

**COMPUTATIONAL MODEL FOR MULTIAXIAL
FATIGUE NOTCH ANALYSIS**

BY

SYED HARIS IFTIKHAR

A Thesis Presented to the
DEANSHIP OF GRADUATE STUDIES

KING FAHD UNIVERSITY OF PETROLEUM & MINERALS

DHAHRAN, SAUDI ARABIA

In Partial Fulfillment of the
Requirements for the Degree of

MASTER OF SCIENCE

In

MECHANICAL ENGINEERING

January 2017

KING FAHD UNIVERSITY OF PETROLEUM & MINERALS

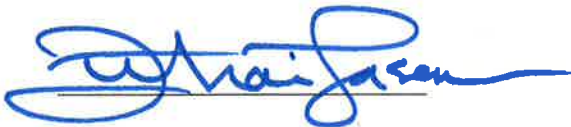
DHAHRAN- 31261, SAUDI ARABIA

DEANSHIP OF GRADUATE STUDIES

This thesis, written by **SYED HARIS IFTIKHAR** under the direction his thesis advisor and approved by his thesis committee, has been presented and accepted by the Dean of Graduate Studies, in partial fulfillment of the requirements for the degree of **MASTER OF SCIENCE IN MECHANICAL ENGINEERING.**



Dr. Jafar Albinmoussa
(Advisor)



Dr. Zuhair M. Gasem
Department Chairman



Dr. Nesar Merah
(Member)



Dr. Salam A. Zummo
Dean of Graduate Studies



Dr. Khaled Saleh Al-Athel
(Member)

11/4/17

Date

© Syed Haris Iftikhar

2017



Dedicated to my grandmother Madia and my grandfather Muaziz Jan,
to my mother Shazia and my father Iftikhar,
and to my aunt Nayab.

ACKNOWLEDGEMENTS

In the Name of Allah, the Most Beneficent, the Most Merciful.

I begin with the name of Allah, the most beneficent, the most merciful. May Allah bestow peace on our beloved Prophet Muhammed (peace and blessings of Allah be upon him), and his family. I would not have been able to complete my thesis work and would not have accomplished success in any walk of life without the help of Allah Almighty who endowed me with patience, health and courage.

During this work my grandparents, my parents, my aunts and my siblings were a constant source of motivation and support. Their love and support, and especially their sincere prayers, helped me reach every milestone of my life.

I would like to thank all my teachers and professors. They have played a positive role in my personality development and motivation to pursue higher education.

I would like to thank King Fahd University of Petroleum and Minerals for providing me with the opportunity and support to pursue my graduate research and coursework.

I would like to thank my thesis advisor Dr. Jafar Albinmoussa for his constant support, motivation and patience. I am thankful to him for all he taught me, and for being a great mentor. I am also thankful to my thesis committee members Dr. Nesar Merah and Dr. Khaled Al-Athel for their involvement and encouragement.

Special thanks to my friend and colleague Mr. Usama Siddiqui for introducing me to different tools and for his helpful discussions. Special thanks to Mr. Azhar Ali Khan and Mr. Hafiz Kabeer Raza for their helpful discussions too. In the end, I would like to thank all my other friends who were there for me through thick and thin throughout my Master's journey.

TABLE OF CONTENTS

ACKNOWLEDGEMENTS	V
LIST OF TABLES	X
LIST OF FIGURES	XI
LIST OF ABBREVIATIONS	XVII
THESIS ABSTRACT (ENGLISH)	XVIII
THESIS ABSTRACT (ARABIC).....	XX
CHAPTER 1 INTRODUCTION AND RESEARCH OBJECTIVES.....	1
1.1 Introduction.....	1
1.2 Objectives of Current Work.....	6
CHAPTER 2 BACKGROUND.....	7
2.1 Theoretical Background.....	7
2.1.1 Stress-Strain Behavior	7
2.1.2 Fatigue Damage Models	20
2.1.3 Cyclic Plasticity	25
2.1.4 Notch Rule	31
2.1.5 Stress-Strain Transformation	34
2.2 Literature Review.....	36
2.2.1 Experimental Studies	37

2.2.2 Computational Studies	39
2.2.3 Literature Review Findings.....	47
CHAPTER 3 COMPUTATIONAL MODELING.....	49
3.1 Notched Component	50
3.1.1 Material	51
3.1.2 Specimen Dimensions.....	52
3.1.3 Benchmark Dataset	53
3.2 FE Model	56
3.2.1 Geometric Model	56
3.2.2 Mesh.....	57
3.2.3 Material Modelling	61
3.2.4 Loading and Boundary Conditions	63
3.3 Elastic-Plastic Stress-Strain Analysis	65
3.4 Modelling of Fatigue Analysis.....	66
3.4.1 Static Material Properties.....	69
3.4.2 Cyclic Fatigue Properties.....	69
3.4.3 Critical Plane Analysis.....	70
3.4.4 Fatigue Damage Models	73
3.5 Proposed Assessment Method	78

3.6 Proposed Fatigue Damage Model.....	84
3.7 Computational Fatigue Design Tool.....	89
CHAPTER 4 RESULTS AND DISCUSSION.....	90
4.1 Validation of FE Model	90
4.2 FEA Results	96
4.2.1 Stress and Strain Distributions.....	96
4.2.2 Stress-Strain Histories.....	103
4.3 Selection of Fatigue Damage Model.....	113
4.3.1 Comparison of Fatigue Damage Models	113
4.3.2 Proposed Assessment Method Results.....	117
4.4 Proposed Damage Model Results	123
4.4.1 Notch Root.....	123
4.4.2 Max von-Mises Location	134
CHAPTER 5 CONCLUSIONS AND RECOMMENDATIONS	145
5.1 Conclusions.....	145
5.2 Recommendations.....	147
NOMENCLATURE.....	149
REFERENCES.....	153
VITAE.....	158

LIST OF TABLES

Table 3-1: Monotonic and cyclic fatigue properties of SAE 1045 steel [10].	52
Table 3-2: Benchmark Dataset [10].	53
Table 3-3: Mesh convergence of the model.	59
Table 3-4: Fatigue testing details of considered alloys.	81
Table 3-5: Chemical compositions (wt%) of considered alloys.	81
Table 3-6: Monotonic properties of considered alloys.	82
Table 3-7: Material constant used in Fatemi-Socie model for all the considered alloys.	82
Table 3-8: Cyclic fatigue properties of all the considered alloys.	84
Table 4-1: Validation of FE model using measured strain gage data.	90
Table 4-2: Error in measured strain gage data.	94
Table 4-3: Critical plane data at notch root of SAE 1045 notched shaft for all the loading types.	128
Table 4-4: Fitting results for the proposed model at the notch root for SAE 1045 notched shaft.	129
Table 4-5: Fitting results for the proposed model at maximum von-Mises node.	139

LIST OF FIGURES

Figure 1-1: Three DOF test fixture for testing SAE 1045 notched shaft [11].	4
Figure 2-1: Engineering and true stress-strain curves [15].	8
Figure 2-2: Tension and compression stress-strain curve [16].	10
Figure 2-3: Torsion of a solid bar [17].	11
Figure 2-4: Stress-strain behavior after unloading followed by a reverse loading [15].	13
Figure 2-5: Cyclic axial stress-strain hysteresis [13].	13
Figure 2-6: Strain-life curve [13].	15
Figure 2-7: Mean stress effects on strain-life curve for SAE 1045 hardened steel [15].	16
Figure 2-8: Bending-Torsion specimen [20].	19
Figure 2-9: Bending and torsion testing system [20].	19
Figure 2-10: A depiction of plastic, positive elastic and negative elastic energy densities [25].	24
Figure 2-11: A schematic illustrating energy-life curve parameters [27].	24
Figure 2-12: Tresca yield surface for $\sigma_z = 0$ [28].	26
Figure 2-13: von-Mises yield surface for $\sigma_z = 0$ [28].	27
Figure 2-14: Strain hardening effects on yield surface [28].	29
Figure 3-1: Modelling and analysis methodology.	50

Figure 3-2: SAE 1045 notched shaft specimen dimensions [7].....	53
Figure 3-3: Schematic for modelling of gripping ends [7].	56
Figure 3-4: Final geometric model of SAE notched shaft.	57
Figure 3-5: Mesh convergence of the model.	59
Figure 3-6: Final mesh of SAE 1045 notched shaft; (a) Whole model, (b) Magnified notch region.....	60
Figure 3-7: Stress-total strain curve for multilinear kinematic hardening [64].	61
Figure 3-8: Modeling of cyclic stress-strain curve of normalized 1045 steel for the cyclic plasticity model.....	63
Figure 3-9: Manner of load applications.....	64
Figure 3-10: Fixed end at the left end face of the constructed model.....	65
Figure 3-11: Flowchart of MATLAB code.....	68
Figure 3-12: Strain-controlled axial-torsional multiaxial loading [69].....	71
Figure 3-13: Defined Cartesian coordinate system at the notch root.....	72
Figure 3-14: Plane rotations; (a) θ rotation about z-axis, (b) ϕ rotations about y-axis [70].....	72
Figure 3-15: State of stress and strain at the notch root [35].	73
Figure 3-16: Plane stress transformation [34].....	75
Figure 3-17: Three dimensional stress state [28].	77
Figure 3-18: Physical basis of Fatemi-Socie model [20].	86

Figure 4-1: Comparison of numerical and measured notch root strains on the SAE 1045 notched shaft specimen; (a) For pure bending loading, (b) For pure torsion loading.....	95
Figure 4-2: Displacement vector sum under pure bending loading at 1/4 th cycle.....	96
Figure 4-3: Stress distribution in x-direction under pure bending loading at 1/4 th cycle.....	97
Figure 4-4: Total mechanical strain distribution in x-direction under pure bending loading at 1/4 th cycle.....	97
Figure 4-5: Displacement vector sum in pure torsion loading at 1/4 th cycle.....	98
Figure 4-6: Shear stress distribution in pure torsion loading at 1/4 th cycle.....	99
Figure 4-7: Shear strain distribution in pure torsion loading at 1/4 th cycle.....	99
Figure 4-8: von-Mises stress distribution under in-phase bending-torsion loading at 1/4 th cycle.....	100
Figure 4-9: von-Mises strain distribution under in-phase bending-torsion loading at 1/4 th cycle.....	101
Figure 4-10: von-Mises stress distribution under 90° out-of-phase bending-torsion loading at 1/8 th cycle.....	102
Figure 4-11: von-Mises strain distribution under 90° out-of-phase bending-torsion loading at 1/8 th cycle.....	102
Figure 4-12: Notch root stress-strain history under pure bending loadings.....	104
Figure 4-13: Notch root stress-strain history under pure torsion loadings.....	105

Figure 4-14: Notch root stress-strain history under in-phase multiaxial loadings.....	106
Figure 4-15: Notch root stress-strain history under 90° out-of-phase multiaxial loadings.....	107
Figure 4-16: Stress-strain history at max von-Mises stress location under pure bending loadings.....	109
Figure 4-17: Stress-strain history at max von-Mises stress location under pure torsion loadings.....	110
Figure 4-18: Stress-strain history at max von-Mises stress location under in-phase multiaxial loadings.	111
Figure 4-19: Stress-strain history at max von-Mises stress location under 90° out-of-phase multiaxial loadings.	112
Figure 4-20: Fatigue life estimations using Fatemi-Socie model; using (a) Albinmousa et al. [3,72] AZ31B Mg alloy data, (b) Zhang et al. [73] AZ61A Mg alloy data, (c) Xiong et al. [2] AZ31B Mg alloy data, and (d) Hoffmeyer [74] S460N structural steel alloy data.....	114
Figure 4-21: Fatigue life estimations using Smith-Watson-Topper model; using (a) Albinmousa et al. [3,72] AZ31B Mg alloy data, (b) Zhang et al. [73] AZ61A Mg alloy data, (c) Xiong et al. [2] AZ31B Mg alloy data, and (d) Hoffmeyer [74] S460N structural steel alloy data.	115
Figure 4-22: Fatigue life estimations using Jahed-Varvani model; using (a) Albinmousa et al. [3,72] AZ31B Mg alloy data, (b) Zhang et al. [73] AZ61A Mg alloy data, and (c) Xiong et al. [2] AZ31B Mg alloy data.....	116

Figure 4-23: Results from the proposed assessment method for Fatemi-Socie model; using (a) Albinmousa et al. [3,72] AZ31B Mg alloy data, (b) Zhang et al. [73] AZ61A Mg alloy data, (c) Xiong et al. [2] AZ31B Mg alloy data, and (d) Hoffmeyer [74] S460N structural steel alloy data.	120
Figure 4-24: Results from the proposed assessment method for Smith-Watson-Topper model; using (a) Albinmousa et al. [3,72] AZ31B Mg alloy data, (b) Zhang et al. [73] AZ61A Mg alloy data, (c) Xiong et al. [2] AZ31B Mg alloy data, and (d) Hoffmeyer [74] S460N structural steel alloy data.	121
Figure 4-25: Results from the proposed assessment method for Jahed-Varvani model; using (a) Albinmousa et al. [3,72] AZ31B Mg alloy data, (b) Zhang et al. [73] AZ61A Mg alloy data, and (c) Xiong et al. [2] AZ31B Mg alloy data.	122
Figure 4-26: Damage-observed life scatter of the Fatemi-Socie model at notch root for SAE shaft.	127
Figure 4-27: Fitting of notch damage scatter with the perfect estimation line for SAE 1045 notched shaft, using; (a) For pure bending loading, (b) For pure torsion loading.	129
Figure 4-28: Damage-observed life scatter at notch root of SAE 1045 notched shaft for all loading types; (a) Fatemi-Socie model, (b) Proposed damage model.	130
Figure 4-29: Fatigue life estimation capability of the model within a factor of 3; (a) Fatemi-Socie model, (b) Proposed damage model.	131
Figure 4-30: Fatigue life estimation capability of the model within a factor of 2.5; (a) Fatemi-Socie model, (b) Proposed damage model.	132

Figure 4-31: Fatigue life estimation capability of the model within a factor of 2; (a) Fatemi-Socie model, (b) Proposed damage model.	133
Figure 4-32: Cumulative probability distribution of SAE shaft at notch root for all loading paths.	134
Figure 4-33: Damage-observed life scatter of the Fatemi-Socie model for SAE 1045 notched shaft.	138
Figure 4-34: Fitting of notch damage scatter with the perfect estimation line; (a) For pure bending loading, (b) For pure torsion loading.	139
Figure 4-35: Damage-observed life scatter for all loading types; (a) Fatemi-Socie model, (b) Proposed damage model.	140
Figure 4-36: Fatigue life estimation capability of the model within a factor of 3; (a) Fatemi-Socie model, (b) Proposed damage model.	141
Figure 4-37: Fatigue life estimation capability of the model within a factor of 2.5; (a) Fatemi-Socie model, (b) Proposed damage model.	142
Figure 4-38: Fatigue life estimation capability of the model within a factor of 2; (a) Fatemi-Socie model, (b) Proposed damage model.	143
Figure 4-39: Cumulative probability distribution of SAE shaft at maximum von-Mises location for all loading paths.	144

LIST OF ABBREVIATIONS

APDL	:	ANSYS Parametric Design Language
EPFEA	:	Elastic Plastic Finite Element Analysis
ESED	:	Equivalent Strain Energy Density
FE	:	Finite Element
FEA	:	Finite Element Analysis
FEM	:	Finite Element Method
FP	:	Fatigue Parameter
MAPE	:	Mean Absolute Percentage Error
MPE	:	Mean Percentage Error

ABSTRACT (ENGLISH)

NAME: Syed Haris Iftikhar
TITLE: Computational Model for Multiaxial Fatigue Notch Analysis
MAJOR FIELD: MECHANICAL ENGINEERING
DATE OF DEGREE: JANUARY 2017

Fatigue life estimations of real-life engineering components is not as successful as that of smooth specimens. Fatigue life estimations of notched components require an accurate estimation of stress-strain histories at the notch root and a successful multiaxial fatigue damage model. Many fatigue damage models have been developed based on smooth specimens that only considers the local stress-strain approach. The local stress-strain approach only account for some of the notch geometric factors (effects) like stress and strain concentrations, while they do not account for other notch geometric factors (effects) like stress and strain gradients. Many researchers have taken the stress and strain gradient effects implicitly, along with local stress-strain analysis, in the multiaxial fatigue damage models by using average (or effective) stresses and strain in the vicinity of notch root. However, this approach does not take into account the sensitivity of the stress and strain gradients effects in fatigue life estimation. Therefore, efforts are made in the current work to take the stress and strain gradient effects explicitly, along with local stress-strain analysis, in the fatigue damage models to account for their sensitivity in fatigue life estimation. An existing multiaxial fatigue damage model, the Fatemi-Socie model, is

modified to account for notch geometric factors (effects) explicitly. A computational fatigue analysis design tool is developed for fatigue life estimations of notched components. This design tool consists of a finite element elastic-plastic stress analysis using ANSYS and multiaxial fatigue damage analysis using MATLAB. The elastic-plastic finite element analysis provides the notch stress-strain histories for the proposed fatigue damage model to estimate fatigue lives. The notched component under consideration is the SAE 1045 notched shaft. Published experimental fatigue life and strain gage data of the SAE notched shaft are used to evaluate fatigue life estimation capability of the proposed damage model and the validation of finite element model, respectively.

The proposed damage model significantly improves fatigue life estimation over that of the Fatemi-Socie model. Taking the notch root as a critical location, the Fatemi-Socie model estimated 83.0% of fatigue life data of all the loading paths within factor of ± 3 , whereas the proposed damage model estimated 83.0% of the data within factor of ± 2.5 . Taking the maximum von-Mises location in the vicinity of notch root as the critical location, the Fatemi-Socie model estimated 70.2% of fatigue life data of all the loading paths falling within factor of ± 3 , whereas the proposed damage model estimated 68.1% and 83.0% of the data within factors of ± 2 and ± 2.5 , respectively. This shows the potential of the proposed damage model for more accurate fatigue life estimations.

ABSTRACT (ARABIC)

ملخص الرسالة

الاسم الكامل: سيد حارث افتخار

عنوان الرسالة: نموذج حاسوبي لتحليل الإرهاب المتعدد المحاور لحز

التخصص: الهندسة الميكانيكية

تاريخ الدرجة العلمية: يناير 2017

تقديرات حياة الإرهاب للمكونات الهندسية الحقيقية ليست ناجحة على نحو العينات المخبرية. تتطلب تقديرات حياة الإرهاب للمكونات تقدير دقيق للإجهاد والانفعال عند الجذر بالدرجة الأولى نموذج ناجح لحساب ضرر الإرهاب العديد المحاور. لقد طرحت العديد من النماذج لحساب الضرر الناتج عن الإرهاب على أساس العينات المخبرية الملساء التي تأخذ في الحسبان فقط طريقة الإجهاد والانفعال المحلي. طريقة الإجهاد والانفعال المحلي تراعي فقط عوامل محدودة لأشكال الشق، مثل تركيز الإجهاد عند الشق، ولكنها لا تأخذ في الاعتبار بعض العوامل الأخرى مثل تدرج الإجهاد والانفعال. لقد اعتبر العديد من الباحثين أثر التدرج في الإجهاد والانفعال فقط ضمناً، جنباً إلى جنب مع تحليل الإجهادات والانفعالات المحلية، في نماذج الضرر الناتج من الإرهاب متعدد المحاور باستخدام متوسط (أو فعال) الإجهادات والانفعالات في محيط جذر الشق. ومع ذلك، فإن هذا النهج لا يأخذ في الاعتبار حساسية تدرج الإجهادات والانفعالات وأثرها في تقدير حياة الإرهاب. لذلك، تبذل جهود في هذا العمل الحالي لاعتبار أثر التدرج في الإجهادات والانفعالات بطريقة مباشرة، جنباً إلى جنب مع تحليل الإجهادات والانفعالات المحلية، في نماذج الضرر الناتج من الإرهاب لحساب حساسية هذه العوامل وتأثيراتها في تقدير الحياة الإرهاب. يتم تعديل نموذج الضرر الناتج من الإرهاب ذو المحاور المتعددة، المعد بواسطة فاتيمي-سوسي، بحيث يتم اعتبار العوامل الشكلية للشق وتأثيراتها بطريقة مباشرة.

تم تطوير نموذج تصميم رقمي بحيث تتم دراسة الإجهاد و الانفعال البلاستيكي للمكون الهندسي بواسطة برنامج أنسس و من ثم يتم تخمين حياة الإرهاق عن طريق برنامج آخر تم إعداده بواسطة برنامج مات لاب. تم التحقق من فعالية نموذج التصميم المطور عن طريق تحليل التجارب المنشورة و التي تم تنفيذها على عينات ذات حز و المصنوعة من فلوذ ١٠٤٥.

يحسن النموذج المقترح تقديرات حياة الإرهاق بشكل كبير مقارنة مع نموذج فاطمي سوسي الأصلي. اذا اخذ جذر الحز بالاعتبار فإن تخمينات الحياه باستخدام معامل فاطمي و سوسي بين معاملين +١- ٣ بنسبة ٨٣٪ بينما تقع تخمينات النموذج المقترح بين معاملين +١- ٢،٥ بنفس النسبة. اذا ما أخذ فون ميسس الأعلى عند حافة الجذر كموقع حساس فإن معامل فاطمي سوسي يخمن الحياه بنسبة ٧٠،٢٪ بين معاملين +١- ٣ بينما يخمن النموذج المقترح الحياه بنسبتين ٦٨،١٪ و ٨٣٪ بين معاملين +١- ٢ و +١- ٢،٥ على التوالي. تشير هذه النتائج الى ان النموذج المقترح قادر على تخمين حياة الإرهاق بشكل أفضل.

CHAPTER 1

INTRODUCTION AND RESEARCH OBJECTIVES

1.1 Introduction

Fatigue failure of structural machine components is a problem of great practical importance. Structural components often operate under multiaxial loadings during service, hence multiaxial fatigue behavior of the material plays an important role in the design of these components. In general, the multiaxial fatigue results from component geometry and external loadings. Unlike uniaxial fatigue, multiaxial fatigue analysis is more challenging as it involves complex strain and stress states. Multiaxial cyclic loading modes can be combined in different ways such that they are in or out-of-phase. Their amplitudes and frequencies can be constant or variable. On the other hand, materials behave differently under these types of loadings. For example, 1045 HR steel develops additional hardening under nonproportional loading as compared to the in-phase loading [1]. Magnesium alloys such as extruded and rolled AZ31B [2–4], extruded AZ61A [5] and extruded ZK60 [6] show asymmetric cyclic behavior due to deformation twinning. This complex material behavior of magnesium alloys may not be considered in existing finite element software.

Therefore, user material subroutines need to be developed to capture the unusual cyclic behaviors such as twinning-detwinning deformations. For example, Behravesh et al. [4] developed a cyclic plasticity model that accounts for the complex asymmetric hardening of magnesium extrusion alloys.

Many machine components have notches or geometrical irregularities such as, but not limited to, fillets, holes, grooves and keyways. These notches cause significant stress concentrations that eventually lead to crack formation. The multiaxial fatigue life estimations of a notched component have not been as successful as those of a smooth test specimen. Accurate estimation of fatigue lives of notched components under multiaxial loadings requires a good estimation of the notch root stress-strain histories and a successful multiaxial fatigue damage model. Of these two, the unavailability of a successful damage model is a major problem. This is because many fatigue damage models are developed for smooth specimens which take into account only the local stress-strain approach and overlooks some geometric factors like stress and strain gradients, which is also a requirement for the notched components. Because of this geometric dependency, the already developed models for smooth specimens fail to accurately estimate fatigue lives of real-life notched components. Therefore, new and improved damage models along with suitable notch stress-strain estimation methods are required for accurate estimation of fatigue lives for industrial notched components under multiaxial loadings.

In 1982, the fatigue design and evaluation committee of the Society of Automotive Engineers (SAE) established an experimental benchmark fatigue testing program in order

to provide data for reliability assessment of multiaxial fatigue approaches. To represent a realistic engineering component, a simple notched shaft that simulated a spindle in a farm tractor was selected as the test specimen. This specimen is named as the SAE 1045 notched shaft specimen. All the notched shafts were subjected to constant-amplitude fully-reversed combined bending-torsion (in-phase and 90° out-of-phase) loadings in load-control mode. Many laboratories took part in developing the benchmark data set. To apply combined bending-torsion loads to the notched shaft, each laboratory created a test fixture of their own [7]. One such example of the test fixture used is shown in Figure 1-1. It is a three degrees of freedom test fixture, which applies bending in two axis and torsion. However, most of the test fixtures were of two degrees of freedom, bending in one axis and torsion. The notched specimen were gripped from both sides in a collet. The torsion moment was constant throughout the section and the bending load varied in the test section. The bending moments were reported at the 5 mm notch root because the notched shaft used to fail there [7].

The notch root stress-strain histories, used to estimate fatigue lives of notched components, can be determined using either experimental, numerical or analytical models. Experimental determination of notch root stress-strain histories may not be feasible because of cost and time considerations. Nonlinear FEA determines the notch stress-strain histories using cyclic plasticity models while analytical models determine it using a notch rule and linear elastic FEA. Simple notch rules such as Neuber [8] or Glinka [9] can be used to estimate the elastic-plastic stress-strain for uniaxial loading. However, estimations

for multiaxial loading states are not as accurate as those from uniaxial loading. The only challenge with using nonlinear FEA is the selection of a suitable plasticity model to accurately capture the material's nonlinear cyclic stress-strain behavior. Multilinear kinematic hardening plasticity model is used in this study, and the FE model is validated by comparing the notch root strain ranges obtained from FE analysis with those of the strain gage data of the SAE notched shaft published by Kurath et al. [10].

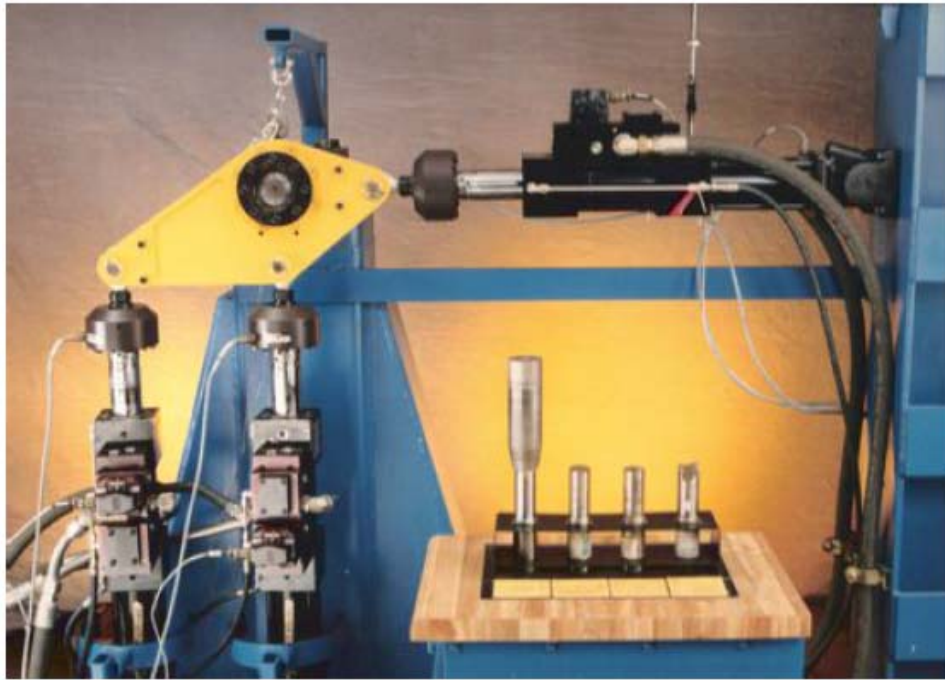


Figure 1-1: Three DOF test fixture for testing SAE 1045 notched shaft [11].

Fatigue design of machine components requires successful fatigue damage models that can estimate life with good accuracy for notched components under multiaxial loadings. During last several decades, many fatigue damage models have been developed for fatigue life estimations, however, no universally accepted damage model exists as most of models

are limited in their application to specific load cases, material and geometry. Socie et al. [11] showed that the current multiaxial fatigue damage models, which estimate fatigue lives well within factors of 2 for smooth specimens, give poor estimations within factors of 10 for SAE 1045 notched shaft. They argued that fatigue life estimations of modern fatigue analysis software was not better than the calculation done 30 years ago by Fash et al. [12]. Thus, in this study, a screening method is proposed which is used to evaluate different fatigue damage models on the basis of smooth tubular specimen data, to select the best model available at the smooth specimen level which will be modified to make accurate fatigue life estimations for notched components.

In this study an existing fatigue damage model, the Fatemi-Socie model, is improved to accurately estimate fatigue lives of notched components. SAE 1045 notched shaft under combined bending-torsion loadings represents a realistic engineering component under complex multiaxial loading in service. Therefore, published experimental multiaxial fatigue data of SAE notched shaft [10], is used to evaluate the fatigue life estimation capability of the proposed damage model for notched components.

Performing experimental durability testing for machine components may not be feasible because of cost and time considerations. Thus, a computational fatigue design tool is developed to analyze notched components subjected to general multiaxial loading conditions. The design tool consists of a numerical elastic-plastic stress-strain analysis performed using ANSYS, to determine the notch stress-strain histories, and a multiaxial fatigue damage analysis performed using MATLAB, for fatigue life estimations.

1.2 Objectives of Current Work

The main objectives of this study are to:

- Review current multiaxial fatigue damage models.
- Select a suitable cyclic plasticity model for FE analysis.
- Develop a new and/or modify an existing fatigue damage model to accurately estimate the fatigue life of notched components subjected to multiaxial loading.
- Develop a computational multiaxial fatigue design tool that integrates FE elastic-plastic stress analysis with the proposed fatigue damage model, for estimating multiaxial fatigue lives of notched components.
- Validate the computational multiaxial fatigue design model, first by verifying the developed FE model simulating SAE 1045 notched shaft under in-phase and 90° out-of-phase multiaxial (combined bending-torsion) loading, and second by evaluating the fatigue life estimation capability of the proposed damage model with published experimental data of the notched shaft.

CHAPTER 2

BACKGROUND

2.1 Theoretical Background

In this section, the theoretical background related to multiaxial fatigue of notched components is discussed. This includes stress-strain behavior, fatigue damage parameters, cyclic plasticity models and analytical notch rules.

2.1.1 Stress-Strain Behavior

Multiaxial fatigue analysis requires an understanding of the stress-strain behavior such as monotonic, cyclic and multiaxial stress-strain behaviors.

Axial Monotonic Behavior

Figure 2-1 shows monotonic tensile engineering and true stress-strain curves. Engineering stress is based on original cross-sectional area and engineering strain is based on original gage length. The engineering stress and strain are given as [13,14]:

$$S = \frac{P}{A_o} \quad (2-1)$$

$$e = \frac{l - l_o}{l_o} \quad (2-2)$$

where P is load applied, A_o is original cross-sectional area, l_o is original length and l is extended length.

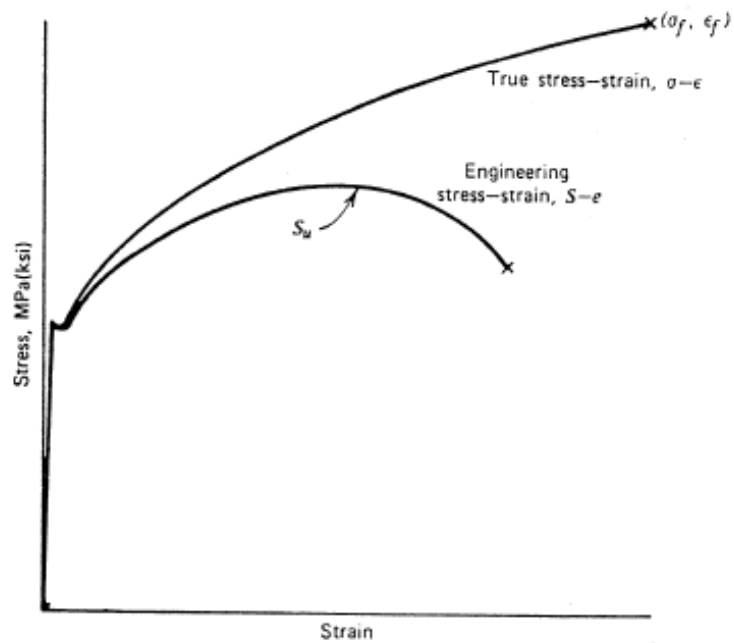


Figure 2-1: Engineering and true stress-strain curves [15].

The true stress is based on instantaneous cross-sectional area and true strain is based on instantaneous gage length. The true stress and strain are given as [13,14]:

$$\sigma = \frac{P}{A} \quad (2-3)$$

$$\varepsilon = \int_{l_0}^l \frac{dl}{l} = \ln \frac{l}{l_0} \quad (2-4)$$

where A is instantaneous cross-sectional area.

For small strains (less than 2%), the engineering and true stresses and strains are nearly equal; hence no distinction between engineering and true components is needed. However, the difference becomes substantial for larger strains [15]. For the case of large strains, a constant volume condition can be considered until necking $Al = A_0l_0$. This consideration is reasonable as the plastic strain doesn't contribute to volume change. Hence, until necking occurs, engineering and true stresses and strains can be related as [13,15]:

$$\sigma = S(1 + e) \quad (2-5)$$

$$\varepsilon = \ln(1 + e) \quad (2-6)$$

The modulus of elasticity E is given by slope of the stress-strain curve within the proportional limit.

The true stress-strain curve can be mathematically modeled using so-called Ramberg-Osgood equation [13]:

$$\varepsilon_t = \varepsilon_e + \varepsilon_p = \frac{\sigma}{E} + \left(\frac{\sigma}{K}\right)^{\frac{1}{n}} \quad (2-7)$$

where n is monotonic tensile strain hardening exponent and K is monotonic tensile strength coefficient.

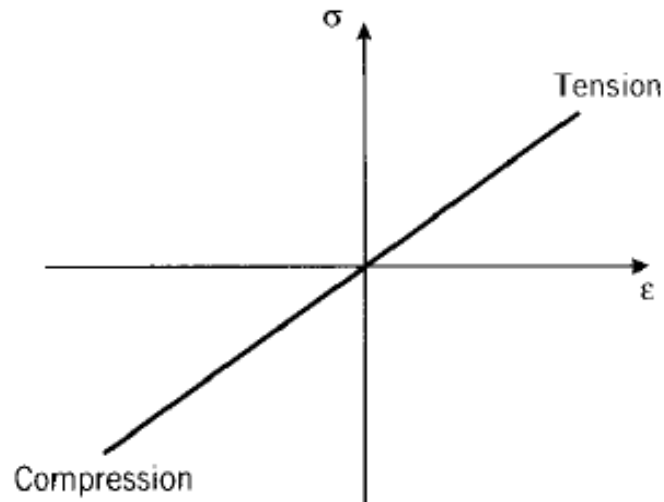


Figure 2-2: Tension and compression stress-strain curve [16].

Note that, if the applied stresses are small i.e. less than the elastic limit, the first term of Eq. (2-7) can be used for the test specimens loaded in compression instead of tension. The stress-strain relations use positive values of σ and ϵ for tension and negative values for compression. Also, the modulus of elasticity E is nearly the same in tension and compression, and the stress-strain curve can simply be thought of being extended as a straight line into the 3rd quadrant [16], as illustrated in Figure 2-2.

Shear Monotonic Behavior

Considering a solid cylinder subjected to a torsional moment M_T at one end as shown in the Figure 2-3. The twisted moment is resisted by shear stresses τ set up within the cross-section. The shear stresses are maximum at the surface and is zero at the center of cylinder [17].

$$M_T = \int_{r=0}^{r=a} \tau r dA = \frac{\tau}{r} \int_0^a r^2 dA \quad (2-8)$$

where r is radial distance and $\int r^2 dA = J$ is polar moment of inertia of the area with respect to axis of cylinder. Thus:

$$M_T = \frac{\tau J}{r} \quad (2-9)$$

It can also be written as:

$$\tau = \frac{M_T r}{J} \quad (2-10)$$

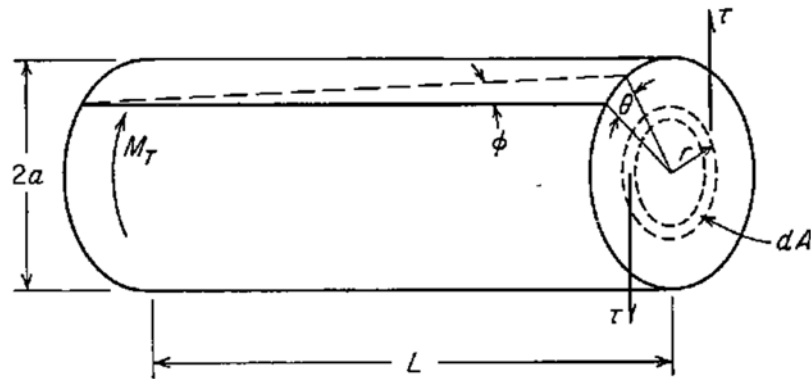


Figure 2-3: Torsion of a solid bar [17].

The maximum stress on surface of the cylinder is given as [17]:

$$\tau_{max} = \frac{16M_T}{\pi D^3} \quad \text{For Solid Cylinder} \quad (2-11)$$

$$\tau_{max} = \frac{16M_T D_2}{\pi(D_2^4 - D_1^4)} \quad \text{For Hollow Cylinder} \quad (2-12)$$

where D is the diameter of the solid cylinder, D_1 is the inside diameter and D_2 is the outside diameter of the hollow cylinder.

The shear strain γ is given by:

$$\gamma = \tan \phi = \frac{r\theta}{L} \quad (2-13)$$

where θ is the angle of twist and L is the length of cylinder.

The shear modulus G in the elastic range is given as:

$$G = \frac{\tau}{\gamma} \quad (2-14)$$

Cyclic Axial Behavior

Unloading a test specimen after plastic deformation, the stress-strain response follows line AB with slope equal to elastic modulus, as shown in Figure 2-4. The stress-strain response will follow path BC if a compressive stress is applied to the test specimen after unloading. It can be observed that the curve AC can be obtained by doubling the curve OA .

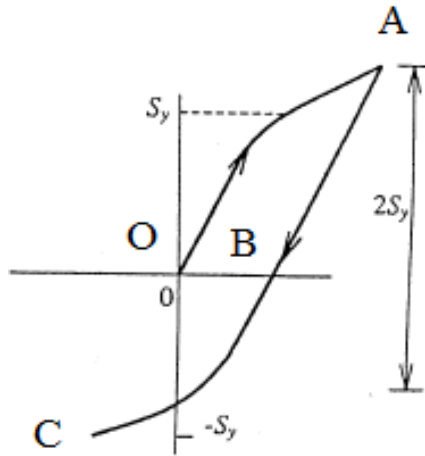


Figure 2-4: Stress-strain behavior after unloading followed by a reverse loading [15].

If the loading, as shown in Figure 2-4, is continued from $-\sigma_{max}$ to σ_{max} , we get a cyclic axial stress-strain hysteresis curve, as shown in Figure 2-5. Area of the hysteresis curve is defined as the energy density dissipating in a cycle.

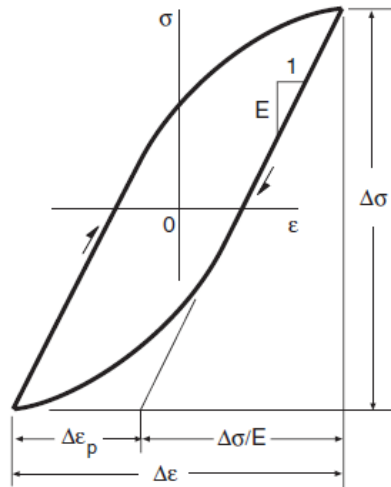


Figure 2-5: Cyclic axial stress-strain hysteresis [13].

Total cyclic axial strain is the addition of elastic and plastic strain components. Its mathematical relation is given as:

$$\Delta\varepsilon = \Delta\varepsilon_e + \Delta\varepsilon_p \quad (2-15)$$

$$\varepsilon_a = \frac{\Delta\varepsilon}{2} = \frac{\sigma_a}{E} + \left(\frac{\sigma_a}{K'}\right)^{\frac{1}{n'}} \quad (2-16)$$

where n' is cyclic axial strain hardening exponent and K' is cyclic axial strength coefficient. General form of cyclic stress-strain hysteresis equation is gives as [13]:

$$\frac{\Delta\varepsilon}{2} = \frac{\Delta\sigma}{2E} + \left(\frac{\Delta\sigma}{2K'}\right)^{\frac{1}{n'}} \quad (2-17)$$

This approximation is only for materials observing symmetric tension and compression behavior.

The elastic strain-life and plastic strain-life data can be approximated using power relations as:

$$\frac{\Delta\varepsilon_e}{2} = \frac{\sigma_f'}{E} (2N_f)^b \quad (2-18)$$

$$\frac{\Delta\varepsilon_p}{2} = \varepsilon_f' (2N_f)^c \quad (2-19)$$

where σ_f' is cyclic axial fatigue strength coefficient, ε_f' is cyclic axial fatigue ductility coefficient, N_f is number of cycles to failure, b is cyclic axial fatigue strength exponent and c is cyclic axial fatigue ductility exponent.

The cyclic axial strain-life curve, as shown in Figure 2-6, can be modeled mathematically using the so-called Coffin-Manson equations:

$$\frac{\Delta\varepsilon}{2} = \frac{\sigma'_f}{E}(2N_f)^b + \varepsilon'_f(2N_f)^c \quad (2-20)$$

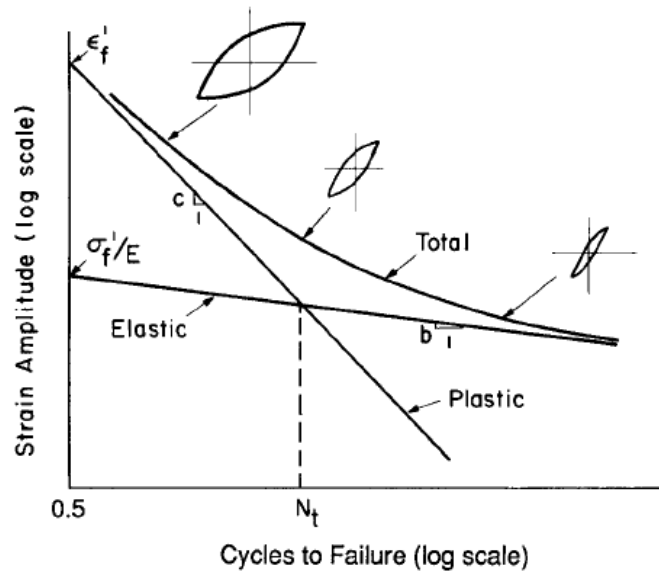


Figure 2-6: Strain-life curve [13].

The fatigue life at which elastic and plastic strains become equal is called the transition life $2N_t$. It can be calculated as:

$$2N_t = \left(\frac{\varepsilon'_f E}{\sigma'_f} \right)^{\frac{1}{b-c}} \quad (2-21)$$

The mean stresses σ_m greatly affect the fatigue life in high cycle regime, as shown in Figure 2-7. Morrow proposed a correction for mean stress effects, called Morrow's mean stress correction [13,15]:

$$\varepsilon_a = \frac{\Delta\varepsilon}{2} = \frac{(\sigma_f' - \sigma_m)}{E} (2N_f)^b + \varepsilon_f' (2N_f)^c \quad (2-22)$$

Morrow proposed another form of the Morrow's mean stress correction for cases when the mean stress affects both elastic and plastic terms [15]:

$$\varepsilon_a = \frac{\Delta\varepsilon}{2} = \frac{(\sigma_f' - \sigma_m)}{E} (2N_f)^b + \varepsilon_f' \left(\frac{\sigma_f' - \sigma_m}{\sigma_f'} \right)^{c/b} (2N_f)^c \quad (2-23)$$

Smith, Watson and Topper have also proposed a correction for including the effects of mean stress [18]:

$$\sigma_{max} \frac{\Delta\varepsilon}{2} = \frac{\sigma_f'^2}{E} (2N_f)^{2b} + \sigma_f' \varepsilon_f' (2N_f)^{b+c} \quad (2-24)$$

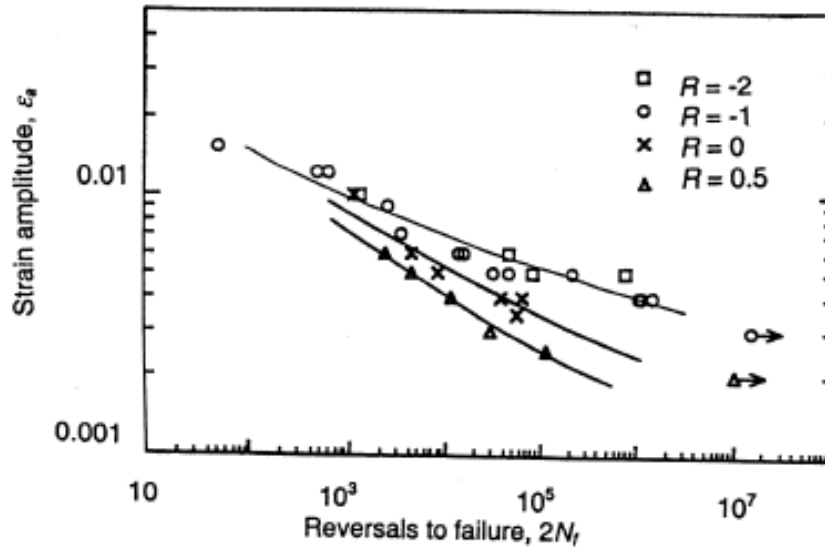


Figure 2-7: Mean stress effects on strain-life curve for SAE 1045 hardened steel [15].

Cyclic Torsion Behavior

Like cyclic axial, the cyclic torsion stress-strain curve can be mathematically modelled using a power equation which can be written as [19]:

$$\frac{\Delta\gamma}{2} = \frac{\Delta\gamma_e}{2} + \frac{\Delta\gamma_p}{2} \quad (2-25)$$

$$\frac{\Delta\gamma}{2} = \frac{\Delta\tau}{2G} + \left(\frac{\Delta\tau}{2K'_s}\right)^{\frac{1}{n'_s}} \quad (2-26)$$

where γ_e is elastic shear strain, γ_p is plastic shear strain, K'_s is cyclic torsional strength coefficient, n'_s is cyclic torsional strain hardening exponent and $\Delta\gamma$ is shear strain range.

Also, shear strain-life curve can be mathematically modeled using a power equation, Coffin-Manson equation, which can be written as [19]:

$$\frac{\Delta\gamma}{2} = \frac{\tau'_f}{G}(2N_f)^{b_s} + \gamma'_f(2N_f)^{c_s} \quad (2-27)$$

where: τ'_f is cyclic torsional fatigue strength coefficient, γ'_f is cyclic torsional fatigue ductility coefficient, b_s is cyclic torsional fatigue strength exponent and c_s is cyclic torsional fatigue ductility exponent.

Multiaxial Cyclic Loading

In multiaxial sinusoidal loading conditions, the phase angle is the angle between axial and torsion strain waveforms. If the maximum of both the axial and torsion strain

waveforms occur at the same time then the phase angle is 0° and the test is called in-phase multiaxial fatigue test, or multiaxial proportional test. This is because at every instant the axial and torsion strains are proportional to one another. However, if the maximum of both the axial and torsion strain waveforms does not occur at the same time, then the test is called out-of-phase multiaxial fatigue test.

As multiaxial loading consists of both axial and torsional loadings, so in order to compare different multiaxial loadings with one another and with pure axial and torsional loadings, an equivalent strain amplitude concept is introduced. The commonly used equivalent strain concept is the von-Mises equivalent strain.

Torsion-bending specimens (Figure 2-8) were one of the first specimens used for studying the multiaxial fatigue behavior of materials [20]. Figure 2-9 shows the force system acting on the torsion-bending specimen. The torsional and bending moments are given as [20]:

$$M_X = (F_1 + F_2)L_B \quad (2-28)$$

$$M_Y = F_3L_B \quad (2-29)$$

$$M_{XY} = (F_1 - F_2)L_T \quad (2-30)$$

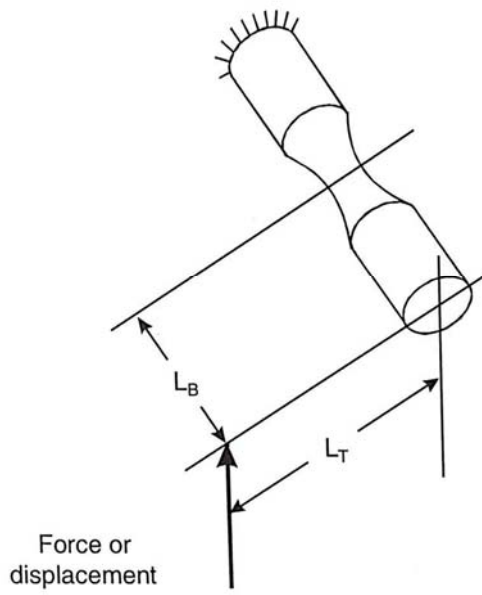


Figure 2-8: Bending-Torsion specimen [20].

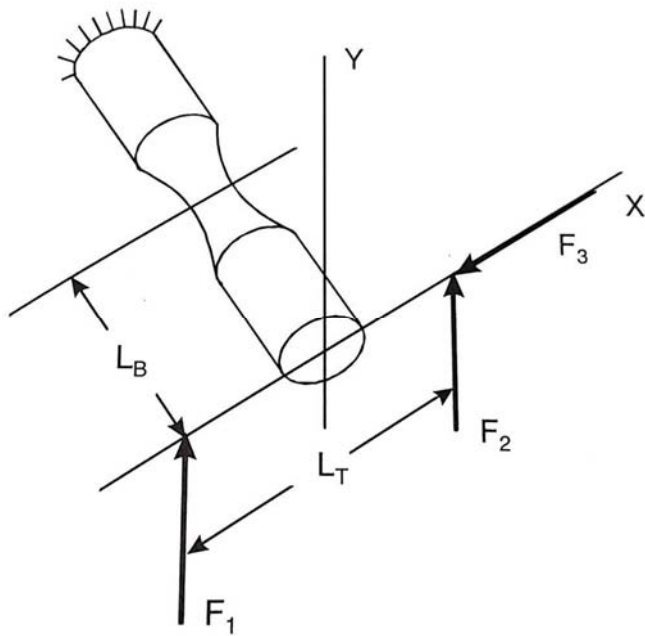


Figure 2-9: Bending and torsion testing system [20].

2.1.2 Fatigue Damage Models

A fatigue damage model consists of a fatigue damage parameter and a fatigue life equation. Fatigue damage parameter is a function that quantifies the fatigue damage in terms of strain and stress variables as well as material-related constants. Whereas, life equation is a function that is used to correlate the damage to fatigue life in terms of cyclic fatigue properties. A fatigue damage model like Fatemi-Socie model uses shear strain based Coffin-Manson equation as the life equation, while the damage parameter consists of shear strain amplitude, a material constant, maximum normal stress and yield strength. In case of multiaxial loading, the damage parameter is expected to collapse experimental data within a single scatter band which is coincident with the fatigue life equation. Therefore, if we substitute experimental fatigue lives we are expecting to get experimental damage values. These value represents the so called “Perfect Estimation”.

Fatigue damage models can be classified into stress-, strain- and energy-based models. Stress-based approaches are used in high cycle fatigue regime, whereas strain- and energy-based approaches can be used in both low and high cycle fatigue regimes. In strain-based models, the damage quantity depends on tensile or shear strains. Whereas in the energy-based models, the damage quantity depends on strain energy.

Critical plane concept has widely been used in all of the three types of fatigue damage models. This is because critical plane based models evaluate damage on specific planes that are expected to be aligned with the physical cracking planes. Hence, critical plane

based models can estimate both fatigue lives and fatigue cracking planes, which gives them advantage over other models that only estimate fatigue lives. This concept originated on the basis of experimental observations [21,22] that fatigue cracks initiate at persistent slip bands (planes).

Three of the commonly used fatigue damage models, namely Fatemi-Socie [23], Smith-Watson-Topper [18] and Jahed-Varvani [24,25] models are reviewed here. They are famous for their accurate life estimation of smooth specimens subjected to multiaxial loading.

Fatemi-Socie Model

Fatemi-Socie model [23] is a strain-based critical plane fatigue damage model that considers the plane of maximum shear strain as critical damaging plane. The governing parameters in this model are maximum shear strain amplitude $\frac{\Delta\gamma_{max}}{2}$ and maximum normal stress $\sigma_{n,max}$ acting on the maximum shear strain plane:

$$\frac{\Delta\gamma_{max}}{2} \left(1 + k \frac{\sigma_{n,max}}{\sigma_{yt}} \right) = \frac{\tau_f'}{G} (2N_f)^{b_s} + \gamma_f' (2N_f)^{c_s} \quad (2-31)$$

where k is a material constant which is determined by fitting the fatigue damage values of cyclic axial with that of cyclic torsion on a damage versus life plot. By trial and error, the value of k is determined for which uniaxial data fits best with the torsion data.

Smith-Watson-Topper Model

Smith-Watson-Topper model [18] is a strain-based critical plane fatigue damage model that considers the plane of maximum axial strain as critical damaging plane. Originally, it was developed to account for the effects of mean stress in uniaxial fatigue analysis, however, Socie [26] extended it to a critical plane based multiaxial fatigue analysis. The governing parameters in this model are maximum axial strain amplitude $\frac{\Delta\varepsilon_1}{2}$ and maximum axial stress $\sigma_{n,max}$ acting on the maximum axial strain plane. The Smith-Watson-Topper model is mathematically expressed as:

$$\sigma_{n,max} \frac{\Delta\varepsilon_1}{2} = \frac{\sigma_f'^2}{E} (2N_f)^{2b} + \sigma_f' \varepsilon_f' (2N_f)^{b+c} \quad (2-32)$$

Jahed-Varvani Model

Jahed-Varvani model [24,25] is an energy-based fatigue damage model that considers total strain energy density as the governing parameter. The total strain energy density comprises of axial and torsion energy densities calculated as the sum of positive elastic and plastic strain energy density components. Addition of the positive elastic energy density allows the inclusion of mean stress effects. In addition, the elastic energy density helps avoid the problem associated with estimating fatigue lives based on small plastic strain energies. Figure 2-10 shows an illustration of the plastic and positive elastic energy densities. The Jahed-Varvani model is mathematically expressed as:

$$N_f = \frac{\Delta E_A}{\Delta E} N_A + \frac{\Delta E_T}{\Delta E} N_T \quad (2-33)$$

where ΔE is total strain energy density, ΔE_A is axial strain energy density, ΔE_T is torsional strain energy density, N_A is fatigue life under purely axial loading and N_T is fatigue life under purely torsion loading.

N_A and N_T are determined using the following Coffin-Manson type energy relations:

$$\Delta E_A = E'_e (N_A)^B + E'_f (N_A)^C \quad (2-34)$$

$$\Delta E_T = W'_e (N_T)^{B_s} + W'_f (N_T)^{C_s} \quad (2-35)$$

where B is axial energy-based fatigue strength exponent, C is axial energy-based fatigue toughness exponent, B_s is torsional energy-based fatigue strength exponent, C_s is torsional energy-based fatigue toughness exponent, E'_e is axial energy-based fatigue strength coefficient, E'_f is axial energy-based fatigue toughness coefficient, W'_e is torsional energy-based fatigue strength coefficient and W'_f is torsional energy-based fatigue toughness coefficient. Figure 2-11 shows an illustration for determining the cyclic fatigue properties of energy-life curve.

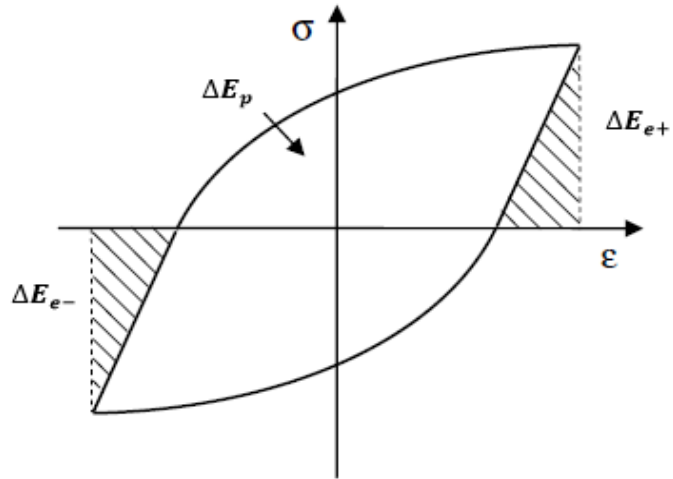


Figure 2-10: A depiction of plastic, positive elastic and negative elastic energy densities [25].

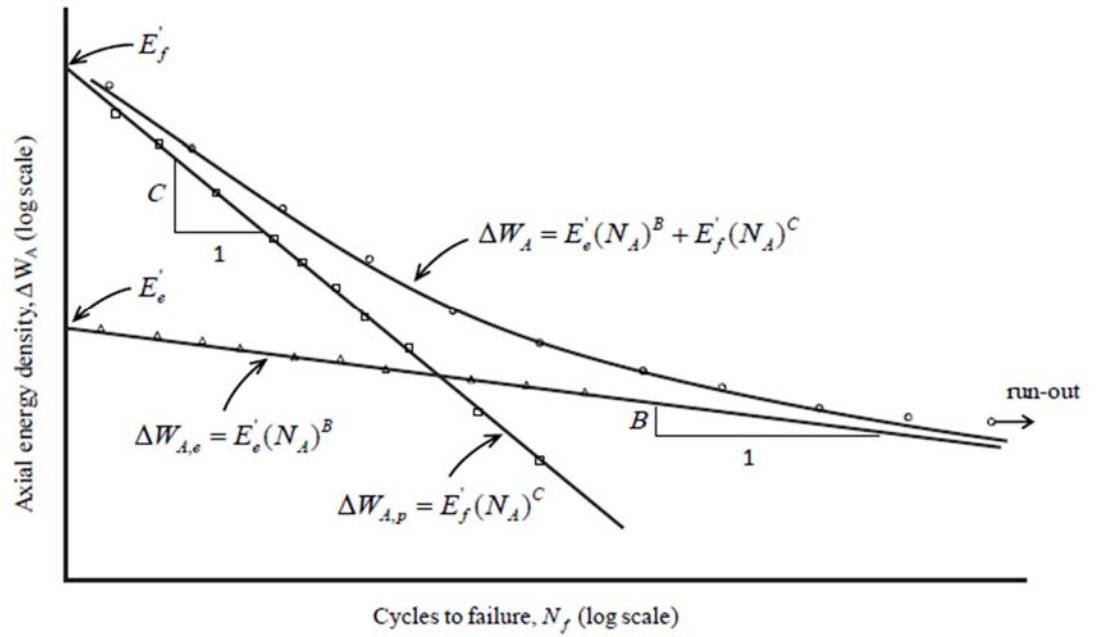


Figure 2-11: A schematic illustrating energy-life curve parameters [27].

2.1.3 Cyclic Plasticity

One of the essential components of the fatigue damage analysis is cyclic plasticity. Notched components contain significant plasticity in the notch region, hence cyclic plasticity is required to determine notch stress-strain histories for multiaxial fatigue analysis. The three basic elements of the theory of plasticity are reviewed here, namely yield criteria, flow rule and hardening rule.

Yield Criterion

The yield criterion is defined as the mathematical expression of stress states which will cause yielding. Generally, the yield criteria can be written as [28]:

$$f(\sigma_x, \sigma_y, \sigma_z, \tau_{xy}, \tau_{yz}, \tau_{xz}) = C \quad (2-36)$$

where C is a material constant. For isotropic materials, it can also be written in form of principal stresses:

$$f(\sigma_1, \sigma_2, \sigma_3) = C \quad (2-37)$$

Many yield criteria have been proposed for all material types. The two most famous yield criteria for ductile metals are Tresca and Mises yield criteria.

According to Tresca yield criterion, yielding occurs when maximum shear stress under complex stress state reaches the maximum shear stress at yielding in a uniaxial tension

stress state [28]. The Tresca yield surface is shown in Figure 2-12. Mathematically, it is expressed as:

$$\sigma_{max} - \sigma_{min} = S_y \quad (2-38)$$

where S_y is tensile yield strength, σ_{max} is maximum principal stress and σ_{min} is minimum principal stress.

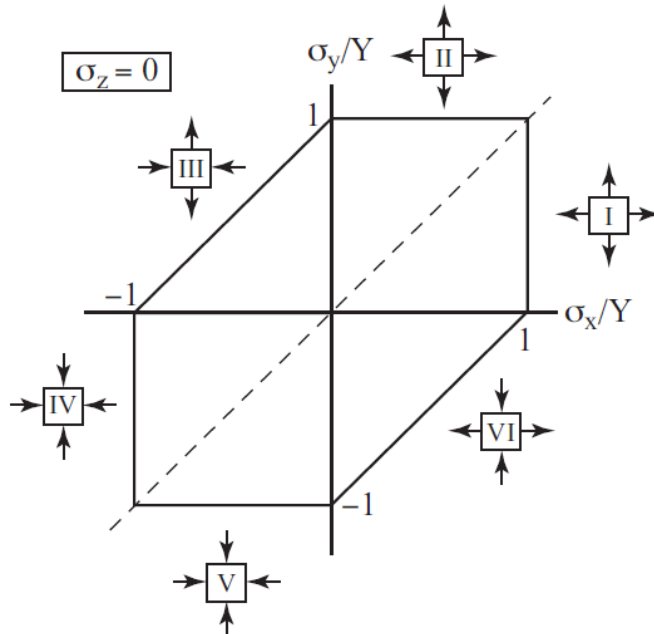


Figure 2-12: Tresca yield surface for $\sigma_z = 0$ [28].

According to von Mises yield criterion, yielding occurs when the root-mean-square shear stress (distortion energy) under complex stress state reaches the root-mean-square shear stress at yielding in a uniaxial tension stress state [28]. The von-Mises yield surface is shown in Figure 2-13. Mathematically, it is expressed as:

$$(\sigma_1 - \sigma_2)^2 + (\sigma_2 - \sigma_3)^2 + (\sigma_3 - \sigma_1)^2 = 2Y^2 \quad (2-39)$$

where σ_1 , σ_2 and σ_3 are the principal stresses.

Also, the multiaxial stress state can be converted, for convenience, to an equivalent von Mises stress σ_e . The equivalent von Mises stress is given as [13]:

$$\sigma_e = \sqrt{\frac{(\sigma_1 - \sigma_2)^2 + (\sigma_2 - \sigma_3)^2 + (\sigma_3 - \sigma_1)^2}{2}} \quad (2-40)$$

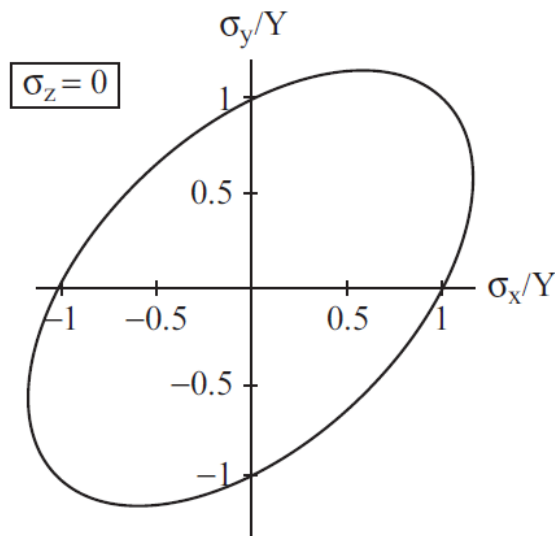


Figure 2-13: von-Mises yield surface for $\sigma_z = 0$ [28].

Flow Rule

For elastic deformations, Hooke's law relates the stresses and strains. Similarly, there are relations for plastic deformations called flow rules that relate plastic strains and stresses. Mathematically, flow rule can be written in general form as [28]:

$$d\varepsilon_{ij} = d\lambda(\partial f/\partial \sigma_{ij}) \quad (2-41)$$

where $d\lambda$ is a constant which depends on stress-strain curve shape and f is yield function.

For the von Mises criterion $f = [(\sigma_1 - \sigma_2)^2 + (\sigma_2 - \sigma_3)^2 + (\sigma_3 - \sigma_1)^2]/4$, so Eq. (2-41) becomes:

$$d\varepsilon_1 = d\lambda[\sigma_1 - (\sigma_2 + \sigma_3)/2] \quad (2-42)$$

$$d\varepsilon_2 = d\lambda[\sigma_2 - (\sigma_3 + \sigma_1)/2] \quad (2-43)$$

$$d\varepsilon_3 = d\lambda[\sigma_3 - (\sigma_1 + \sigma_2)/2] \quad (2-44)$$

The above set of equations are known as Levy-Mises equations. Even if $d\lambda$ is unknown, they can determine strain ratios from a known stress state or the stress ratios from a known strain state. Also, $d\lambda$ can be written as $d\lambda = d\bar{\varepsilon}/d\bar{\sigma}$, which is inverse slope of effective stress-strain curve at the point where strains are being evaluated [28].

Hardening Rule

The hardening rules describe the change in the yield criterion as a function of plastic strains [15]. The two mostly used hardening rules are isotropic and kinematic hardening. In isotropic hardening model, the strain hardening effects during plastic deformation is only to expand the yield surface uniformly without changing its shape, as shown in

Figure 2-14a. The yielding stresses for all the loading paths are increased by the same factor [28]. In kinematic hardening model, the strain hardening effects during plastic

deformation does not change the size and shape of the yield surface, it only shifts the yield surface along the loading path [28], as shown in Figure 2-14b.

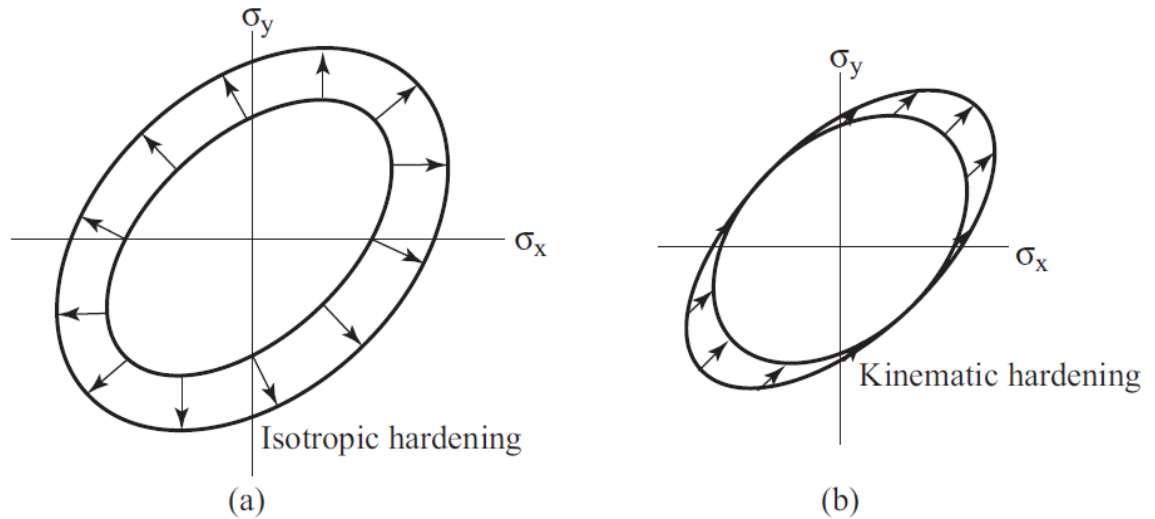


Figure 2-14: Strain hardening effects on yield surface [28].

The isotropic hardening model, unlike kinematic hardening model, does not account for the Bauschinger effect; a common feature in polycrystalline materials [29]. This effect suggests that if a material is subjected to a type of loading followed by another type of loading, then yielding in material is observed at a stress lower than that at which it was unloaded [28]. Modelling of the Bauschinger effect is essential for any cyclic plasticity model, which necessitates the use of kinematic hardening model instead of isotropic hardening model in this study. Some characteristics of both isotropic and kinematic hardening effects are shown by real materials before cyclic stabilization, however, after stabilization they only show kinematic hardening effects [20]. As in fatigue analysis, the cyclic stable material behavior is of more interest than the initial transient material

behavior, hence kinematic hardening models are used to model the cyclic stable material behavior [20].

Kinematic Hardening Models

Kinematic hardening was first introduced by Prager [30]. According to his rule, the yield surface follows the stress point in the stress space without any expansion. The main disadvantage of this model was its application only to bilinear stress-strain curve. However, many engineering materials show nonlinear hardening behavior during plastic loading. Therefore, more general models were developed to take this behavior into account. These models can be divided into three types: multi-surface plasticity models, two-surface plasticity models and linear kinematic models. Only the first two models are discussed here in detail.

Mroz [31] was first to introduce the multi-surface plasticity model. According to him the uniaxial stress-strain curve can be approximated using finite number of linear segments such that each linear segment has its own constant plastic modulus. A stress surface similar to that of yield surface is defined for each corresponding stress state at which the plastic modulus changes in the uniaxial stress-strain approximation. The defined stress surfaces will be concentric for an initially isotropic material. When a stress surface is reached by the stress state, it will be activated. Now if the load is increased, then this activated stress surface and all previously activated stress surfaces, called the inner surfaces, move together until unloading occurs. While working with an active stress surface, its hardening modulus

will be proportional to plastic modulus of that section of the corresponding stress-strain curve. Mroz's model has a disadvantage of the possibility of intersection of stress surfaces for nonproportional loadings, which can cause computational problems. Garud [32] modified Mroz's model in order to prevent this stress surface interaction. According to Garud, the movement of stress surfaces is dependent on the stress direction.

Dafalias and Popov [33] proposed one of the initial two-surface plasticity models. The two-surface plasticity model was devised to describe complex cyclic loading i.e. to describe the material response for partial unloading followed by loading or fully reversed loading. In their model, two yield surfaces of the same shape are defined: loading (inner) and bounding (outer) surfaces. The loading (inner) surface defines elastic limit of the current stress state. If yielding occurs then the current stress point lies on loading surface, and it has a corresponding stress point on bounding surface with the same normal. As the yield surfaces are assumed similar and the current and corresponding stress points have the same normal direction, so contact is imposed only to occur at the current and corresponding stress point. In this model, slope of uniaxial stress-strain curve is described by elastic, plastic and tangential modulus in the elastic part, plastic part, and at any loading point on the curve, respectively.

2.1.4 Notch Rule

Strain-life approach is employed for the fatigue of notched components because there is often plastic deformation at the notch root. This approach, first determines the notch

stress-strain histories, and then life estimation is made on them using fatigue damage models.

The concentration of stresses and strains in the notch region are given by stress and strain concentration factors:

$$K_{\sigma} = \frac{\sigma}{S} \quad (2-45)$$

$$K_{\varepsilon} = \frac{\varepsilon}{e} \quad (2-46)$$

For elastic deformation at the notch region, $K_{\sigma} = K_{\varepsilon} = K_t$, where K_t is elastic stress concentration factor. Whereas for plastic deformation at notch region, K_{σ} reduces and K_{ε} increases with increasing notch stress.

For fatigue analysis, notch rules can be used for estimating the notch stress-strain hysteresis. Two notch rules, namely Neuber's [8] and Glinka's [9] rules, are discussed here.

Neuber's Rule

This rule states that the geometric mean of strain and stress concentration factors under plastic deformation condition is equal to the elastic stress concentration factor. Mathematically it can be expressed as [8]:

$$K_{\varepsilon} K_{\sigma} = K_t^2 \quad (2-47)$$

$$\varepsilon \sigma = K_t^2 e S \quad (2-48)$$

In order to apply Neuber's rule, a simultaneous solution of Eq. (2-48) with tensile stress-strain curve equation (Ramberg-Osgood) is required. The solution is found using iterative techniques and gives the required values of σ and ε .

For the cyclic loading conditions, Topper et al. have suggested to use fatigue notch factor K_f instead of K_t [15], therefore, Eq. (2-48) can be written as:

$$\Delta\varepsilon\Delta\sigma = K_f^2 \Delta e \Delta S \quad (2-49)$$

Equivalent Strain Energy Density or Glinka's Rule

Strain energy density or Glinka's rule [9] assumes that an elastic stress field is surrounding the plastic deformation zone at notch root. This rule states that the notch root strain energy density is nearly the same for both linear elastic (W_e) and elastic-plastic (W_p) material behaviors. The nominal strain energy density is given as:

$$W_s = \int_0^e S de = \int_0^S \frac{S}{E} dS = \frac{S^2}{2E} \quad (2-50)$$

Assumption of linear elastic material behavior gives:

$$W_e = \int_0^{\varepsilon_e} \sigma d\varepsilon = \int_0^{\sigma_e} \frac{\sigma}{E} d\sigma = \frac{\sigma^2}{2E} = \frac{(K_t S)^2}{2E} \quad (2-51)$$

Assumption of elastic-plastic material behavior gives:

$$W_p = \int_0^\varepsilon \sigma d\varepsilon = \frac{\sigma^2}{2E} + \frac{\sigma}{n+1} \left(\frac{\sigma}{K}\right)^{1/n} \quad (2-52)$$

Setting $W_p = W_e$ results in:

$$\frac{\sigma^2}{E} + \frac{2\sigma}{n+1} \left(\frac{\sigma}{K}\right)^{1/n} = \frac{(K_t S)^2}{E} \quad (2-53)$$

For a given nominal stress S, notch stress σ can be found using the above equation.

Also, for cyclic loading, the Eq. (2-53) becomes:

$$\frac{(\Delta\sigma)^2}{E} + \frac{4\Delta\sigma}{n'+1} \left(\frac{\Delta\sigma}{2K'}\right)^{1/n'} = \frac{(K_t \Delta S)^2}{E} \quad (2-54)$$

The notch strain range $\Delta\varepsilon$ is then found from the hysteresis loop:

$$\Delta\varepsilon = \frac{\Delta\sigma}{E} + 2 \left(\frac{\Delta\sigma}{2K'}\right)^{1/n'} \quad (2-55)$$

2.1.5 Stress-Strain Transformation

2D Stress-Strain Transformation

The stress and strain transformation equations for plane stress state is given by the following equations [34]:

$$\sigma_{x'} = \frac{\sigma_x + \sigma_y}{2} + \frac{\sigma_x - \sigma_y}{2} \cos(2\theta) + \tau_{xy} \sin(2\theta) \quad (2-56)$$

$$\tau_{x'y'} = -\frac{\sigma_x - \sigma_y}{2} \sin(2\theta) + \tau_{xy} \cos(2\theta) \quad (2-57)$$

$$\varepsilon_{x'} = \frac{\varepsilon_x + \varepsilon_y}{2} + \frac{\varepsilon_x - \varepsilon_y}{2} \cos(2\theta) + \frac{\gamma_{xy}}{2} \sin(2\theta) \quad (2-58)$$

$$\gamma_{x'y'} = -(\varepsilon_x - \varepsilon_y) \sin(2\theta) + \gamma_{xy} \cos(2\theta) \quad (2-59)$$

The principal stress and maximum shear stress angles are given as [34]:

$$\tan 2\theta_p = \frac{2\tau_{xy}}{\sigma_x - \sigma_y} \quad (2-60)$$

$$\tan 2\theta_s = -\frac{\sigma_x - \sigma_y}{2\tau_{xy}} \quad (2-61)$$

3D Stress-Strain Transformation

Stress and strain are second order tensors, therefore, they must transform in the manner of following equations [29,35,36]:

$$\sigma'_{ij} = M\sigma_{ij}M^T \quad (2-62)$$

$$\varepsilon'_{ij} = M\varepsilon_{ij}M^T \quad (2-63)$$

Where M is the transformation or rotation matrix, M^T is the transpose of the transformation matrix, σ_{ij} and ε_{ij} are the stress and strain time-history tensors, and σ'_{ij} and ε'_{ij} are the corresponding stress and strain time-history tensors transformed to a potential plane.

The potential plane is defined by two angles, θ and ϕ , such that it is reached by first rotating xy-plane clockwise about z-axis by an angle of θ and then by rotating

anticlockwise about y-axis by an angle of θ . The clockwise rotation matrix around z-axis by an angle θ is given as:

$$M_{\theta} = \begin{bmatrix} \cos \theta & \sin \theta & 0 \\ -\sin \theta & \cos \theta & 0 \\ 0 & 0 & 1 \end{bmatrix} \quad (2-64)$$

Similarly, the anticlockwise rotation matrix around y-axis by an angle of ϕ is given as:

$$M_{\phi} = \begin{bmatrix} \cos \phi & 0 & \sin \phi \\ 0 & 1 & 0 \\ -\sin \phi & 0 & \cos \phi \end{bmatrix} \quad (2-65)$$

So, the general transformation matrix to define both the θ and ϕ rotations is given as:

$$M = M_{\phi}M_{\theta} = \begin{bmatrix} \cos \phi & 0 & \sin \phi \\ 0 & 1 & 0 \\ -\sin \phi & 0 & \cos \phi \end{bmatrix} \begin{bmatrix} \cos \theta & \sin \theta & 0 \\ -\sin \theta & \cos \theta & 0 \\ 0 & 0 & 1 \end{bmatrix} \quad (2-66)$$

2.2 Literature Review

The understanding of multiaxial fatigue behavior of real-life notched components is a problem of great significance. Fatigue studies of notched components under multiaxial loading has been a focus of many research groups for more than three decades. However, there is no successful fatigue damage model that can accurately estimate fatigue lives of notched components, because of the complexity involved in terms of geometry and loadings. To this date, many studies are focused around the multiaxial fatigue behavior of

notched components to develop a successful fatigue damage model for notched components.

Literature review revealed that the multiaxial fatigue behavior of notched components has been investigated experimentally as well as computationally.

2.2.1 Experimental Studies

Multiaxial fatigue behavior of notched components have been investigated experimentally to understand the complex fatigue behavior of notched components. Experimental benchmark study of SAE 1045 notched shaft by Society of Automotive Engineers (SAE) is one of the most extensive experimental study of notched components. It provides a detailed benchmark fatigue dataset for understanding the multiaxial fatigue behavior of notched components. Kurath et al. [10] have reported this benchmark fatigue dataset of the SAE 1045 notched shaft. They have provided multiaxial fatigue data for tubular specimen, unnotched and notched shafts made from normalized SAE 1045 steel. Harvey [37] has conducted another extensive experimental study to explain the fatigue and cracking behavior of notched components. Harvey conducted fatigue tests on a solid unnotched shaft similar to a notched shaft in geometry but having no large stress concentration. The unnotched shaft results were compared with the data from notched and thin-walled tubular specimens. The results showed similar cracking behavior in both unnotched shaft and thin-walled tubular specimens, however, fatigue lives in the unnotched shaft were similar to those of the notched shaft. Fatigue studies has relied more and more

on experimental fatigue testing of notched components of various notch geometries made from different materials, throughout the decades and even in the recent years, to further understand the notch behavior. Some of the recent experimental studies include, but not limited to, the work of Branco et al. [38] and Gates et al. [39]. Branco et al. [38] did fatigue testing of solid round bars with a lateral U-shaped notch produced from DIN 34CrNiMo6 high strength steel. Constant amplitude loading fatigue tests with stress ratio near zero were performed under pure bending, pure torsion and in-phase bending-torsion loadings. They also monitored the crack initiation and growth with in-situ setup. Similarly, Gates et al. [39] employed tubular specimens with a circular transverse hole produced from 2024-T3 Al alloy to study the multiaxial fatigue estimation of notched specimens. Fully reversed constant amplitude tests in load control were performed under axial, torsion and multiaxial loadings.

The experimental durability testing of engineering components is not feasible because of the high cost and time considerations. Therefore, the focus of both industrial and academic fatigue researchers are shifting more and more towards computational means. Efforts are made by researchers to develop successful computational models to help the design engineers in designing complex but reliable engineering components. They would help in designing the complex shaped components without going into the hassle of machining them and of designing special fixtures for each of them (to simulate the loading to which they are subjected during service).

2.2.2 Computational Studies

Computational studies of notched components are performed to model their complex cyclic plasticity behavior and multiaxial fatigue behavior. Multiaxial fatigue life estimation of notched components requires an accurate estimation of notch root stress-strain histories and a successful multiaxial fatigue damage model. A comprehensive study of the stress-strain estimation approaches, fatigue life estimation approaches and notch geometric effects of notch components are described below.

Notch Stress-Strain Estimation

The notch root stress-strain histories can be determined experimentally, analytically and numerically. Experimental determination of notch root stress-strain histories may not be feasible because of cost and time considerations. Earlier analytical studies of notched components relied on stress concentration factors. Peterson [40] in his book has compiled the stress concentration factors for a variety of notches under different loading conditions. Then several notch rules were established to extend the notch analysis from purely elastic to elastic-plastic stress-strain analysis. Neuber [8] proposed a notch correction method which states that the geometric mean of strain and stress concentration factors under plastic deformation condition is equal to the elastic stress concentration factor. Molski and Glinka [9] proposed another notch correction method known as equivalent strain energy density (ESED) rule which states that the notch root strain energy density is nearly the same for both linear elastic and elastic-plastic material behaviors. Glinka [41] extended ESED rule

to notched components under cyclic loadings. Then, efforts were made to extend the notch rules from cyclic loading conditions to multiaxial loading conditions. Hoffmann and Seeger [42,43] extended Neuber's rule to multiaxial proportional loadings by using equivalent stress and strain components. Moftakhar [44] has also generalized Neuber and ESED rules for multiaxial proportional loadings. Hoffmann et al. [45] and Singh [46] extended the notch analysis from multiaxial proportional to nonproportional loading conditions. Hoffmann et al. [45] proposed an approach for nonproportional multiaxial loadings by incremental generalization of Neuber rule. Singh [46] extended both Neuber and ESED rules for nonproportional multiaxial loadings using incremental stress-strain approach. Tipton et al. [47] proposed a new approach for estimating notch strains, of the SAE 1045 notched shaft, with a simplified elastic-plastic analysis utilizing nominal elastic strains. Their approach is used to estimate curves of stabilized notch bending strain amplitude versus applied bending moment amplitude and notch shearing strain amplitude versus applied torque amplitude. Chu et al. [36] developed a 3D stress-strain model based on kinematic-isotropic hardening rule, which can be used to estimate the notch root stress-strain histories from the strain gage measured strain histories. For the fatigue life estimation of SAE 1045 notched shafts, they determined the notch stress-strain histories using this constitutive model. Lee et al. [48] have developed a constitutive model which estimates the notch stress-strain states on basis of linear elastic stress analysis. They utilized a two-surface model with Mroz's hardening equation along with associated flow rule, and showed reasonable correlations between estimated and measured notch strains for the SAE 1045 alloy. Many recent studies like, but not limited to, Ince et al. [49], Branco et al. [38] and

Gates et al. [39]; have used analytical methods for estimation of the notch stress-strain histories. Ince et al. [49] have developed a multiaxial notch analysis in which they have combined the multiaxial Neuber notch correction method with Garud cyclic plasticity model to estimate the stress-strain state at the notch root. Branco et al. [38] used the linear elastic FEA and employed the equivalent strain energy density approach to analyze the notch effect of DIN 34CrNiMo6 steel solid round bars with a lateral U-shaped notch. Gates et al. [39] used both Neuber's rule and elastic-plastic FEA for determining the notch stress-strain histories of 2024-T3 Al alloy tubular specimens with a circular transverse hole. Both the methods were found to be in reasonable agreement with each other.

The analytical methods are simple and less time consuming, however the FE methods are more robust [50]. Many research groups have conducted elastic-plastic FE analysis (EPFEA) using a variety of FE packages for the determination of notch stress-strain histories. Fash [51], Fash et al. [12], Socie et al. [11], Gates et al. [39] and Shen et al. [52] have used ABAQUS FE tool for EPFEA of the notched components. Fash [51], Fash et al. [12] and Socie et al. [11] successfully modelled the SAE 1045 notched shaft. Gates et al. [39] successfully modelled tubular specimens with a circular transverse hole made from 2024-T3 Al alloy. Shen et al. [52] modelled two notched components, a U-notched plate under cyclic axial loadings and SAE 1045 notched shaft under multiaxial loadings. Das et al. [50] have used ANSYS FE package for EPFEA (using kinematic hardening rule) of the SAE shaft. Many other researchers like, but not limited to, Tipton et al. [53] and Li et al. [54] have also successfully utilized FE models for determination of notch stress-strain

histories. Tipton et al. [53] and Li et al. [54] have developed a FE model of SAE shaft to determine the notch root stress-strain histories. These stress-strain histories were used as an input to the fatigue life estimation approaches.

Multiaxial Fatigue Damage Models

For fatigue life estimation of notched components, many research groups have used the multiaxial fatigue damage models that were developed for smooth specimens. These models only takes into account the local stress-strain analysis, which only accounts for some of the notch geometric effects like stress and strain concentrations.

Tipton et al. [53] and Hoffmann et al. [43] have evaluated several strain based fatigue damage parameters to estimate fatigue lives of SAE notched shaft. Tipton et al. [53] have used eight parameters, which are based on: von-Mises effective strain amplitude, maximum shear strain amplitude, maximum principal strain amplitude, ASME boiler and pressure vessel code, Brown and Miller, Lohr and Ellison, Garud's plastic work and Mowbray's hydrostatic stress correction approaches. The von-Mises effective strain amplitude, brown and miller and plastic work approaches based damage models estimated fatigue lives well as compared to others. Hoffmann et al. [43] have used three parameters, which are: maximum principal strain parameter, von-Mises equivalent strain parameter and maximum shear strain parameter. The maximum principal strain parameter provided the best results, by giving fatigue life estimations within factors of 3.

Researchers like Das et al. [50], Li et al. [54], Firat [55] and Ince et al. [56] have studied the critical plane based multiaxial fatigue damage models for fatigue life estimation of notched components. They have shown that the critical plane based models give reasonably good fatigue life estimations. Das et al. [50] have shown that the critical plane based fatigue damage models gives better fatigue life estimations for notched shafts when used at the plane which provides the maximum damage rather than the plane which provides the maximum strain range. Li et al. [54] proposed a new critical plane based fatigue damage model that considers the maximum shear strain plane as the critical damaging plane. Their proposed model estimated the multiaxial fatigue life of SAE notched shaft specimens within a factor 3.2. Firat [55] have used two critical plane based models, Fatemi-Socie and Smith-Watson-Topper models, for multiaxial fatigue life estimations of SAE notched shaft. The estimated and experimental lives were in good correlation, and mostly conservative for both multiaxial proportional and non-proportional loadings. Ince et al. [56] proposed a generalized strain energy form and a generalized strain amplitude form of an original critical plane-based fatigue damage model. Both of the damage parameters take into account mean stress effects, path dependency of stress response and non-proportional hardening. These damage parameters demonstrated reasonably well multiaxial fatigue life estimations for both tubular and SAE 1045 notched shaft specimens.

Socie, as a keynote speaker for 10th International Conference on Multiaxial Fatigue & Fracture held in Japan in 2013, concluded his research group results (Socie et al. [11]) that the current fatigue damage models give poor estimations for notched components. They

performed computational fatigue analysis, on the published experimental multiaxial fatigue data of SAE notched shaft and smooth specimens, with the help of several software packages. They showed that the current multiaxial fatigue damage models, which can estimate fatigue lives well within a factor of 2 for smooth specimens, give poor estimations within factor of 10 for SAE 1045 notched shaft specimen. Socie's remarks has helped the fatigue community to focus more on the real-life engineering components than the laboratory smooth specimens. And, as a result, many new studies has emerged centered around multiaxial fatigue analysis of notched components. These studies include, but not limited to, Branco et al. [38], Gates et al. [39], Shen et al. [52], Ince et al. [35] and Gates et al. [57]. Branco et al. [38] used the Coffin-Manson model for fatigue life estimations of DIN 34CrNiMo6 high strength steel solid round bars with a lateral U-shaped notch. The local von Mises equivalent stress was used as the damage parameter. The estimated and experimental lives were in good correlation, especially for fatigue lives greater than 10^4 cycles. Gates et al. [39] used several approaches for fatigue life estimations of 2024-T3 Al alloy tubular specimens with a circular transverse hole. The nominal stress-life approach, based on von Mises equivalent stress and maximum principal stress, estimated mostly non-conservative fatigue lives with life scatter varied by as much as a factor of 10. Local strain and stress-life approaches, based on von Mises equivalent strain or stress, estimated reasonably well in low cycle fatigue regime, but estimation got less and less accurate from mid to high cycle regime with data scatter by more than a factor of 10. However, the estimated and experimental lives were in good correlation for the Fatemi-Socie model, with data mostly falling within a factor of 3. Shen et al. [52] proposed a damage-coupled elastic-

plastic model implemented in ABAQUS which accounts for nonlinear kinematic hardening, to estimate fatigue lives of notched components. They used two damage models, a plastic strain-based and a stress-based. Two cases were studied, a U-notched plate under cyclic axial loadings with estimated lives within a factor of 2, and SAE notched specimen under multiaxial loadings with estimated lives mostly within a factor of 3. Ince et al. [35] proposed a computational fatigue analysis methodology to estimate fatigue lives of notched components, consisting of an elasto-plastic stress analysis and a proposed fatigue damage model. The proposed model correlated estimated lives reasonably well with the multiaxial proportional and non-proportional experimental life data of SAE notched shaft.

Notch Geometric Effects

Some researchers have stressed on further studying the effects of notch geometry on the fatigue life estimations of notched specimens. Fash et al. [12] used five multiaxial fatigue damage models and got the fatigue life correlation for smooth specimens and SAE shafts within factor of 3 and 10, respectively. Therefore, they are of the opinion that the geometrical effects are as important as the selection of fatigue damage model. Tipton et al. [58] have concluded, on the basis of the complex behavior shown by their test data, that the multiaxial fatigue life estimation cannot be characterized just by surface notch stress-strain histories. The nature of the specific notch geometry and the stress distribution over notch cross-section must also be accounted for.

Current fatigue damage models are not able to accurately estimate fatigue lives of notched components because they only take into account the local stress-strain analysis. The local stress-strain analysis only accounts for some of the notch geometric effects like stress and strain concentrations, while they do not account for other notch geometric effects like stress and strain gradients. Many researchers have studied the stress and strain gradient effects, caused by the notch geometry, on the fatigue life estimation of notched specimens. Weixing [59] has proposed a new approach, strain field intensity approach, for estimating fatigue lives of notched components. Instead of taking peak stress value as in the case of local stress-strain approach, they take stress field intensity over local region of damage to account for the gradient effects. Weixing et al. [60] has studied the average stress, fracture mechanics and stress field intensity model based expressions for fatigue notch factor. They showed that the stress field intensity approach is most reasonable and has great potential. Shang et al. [61] proposed a local stress-strain approach, by extending the stress field intensity approach, to take into account the local stress-strain gradient effects into fatigue damage. They showed better fatigue life correlation for local stress-strain intensity approach compared to traditional local stress-strain approach using U-notched specimens made of normalized 45 steel. Adib et al. [62] has used volumetric approach which has a stress field intensity base. They showed that this approach gives better results than Neuber and Molski-Glinka approaches. Gates et al. [57] used Theory of Critical Distances (TCD) to incorporate the stress gradient effects in the Fatemi-Socie model. They used 2024-T3 notched tubular specimens and AISI 1141 stepped and grooved shaft specimens and showed that the Theory of Critical Distances (TCD) approach gives better fatigue life

correlation than the fatigue notch factor approach. Using eFatigue, Socie et al. [11] also used critical distance method for the SAE 1045 notched shaft to take into account the gradient effects.

All the above researchers have taken the stress and strain gradient effects implicitly in the multiaxial fatigue damage models by using average (or effective) stresses and strains in the vicinity of notch root. Thus, this approach provides better results than just the local stress-strain approach because they account for the stress and strain gradient effects. However, this approach does not take into account the sensitivity of the stress and strain gradients in fatigue life estimation. Therefore, the estimation using this approach is also not that accurate.

2.2.3 Literature Review Findings

The fatigue life estimation of notched components by current fatigue damage models, that only considers the local stress-strain approach, is not very accurate. This is because the local stress-strain analysis only accounts for some of the notch geometric effects like stress and strain concentrations, while they do not account for other notch geometric effects like stress and strain gradients. Also, taking the stress and strain gradient effects implicitly in the fatigue damage models, using average stresses and strains in the vicinity of notch root, is not enough. This is because the implicit approach does not take into account the sensitivity of the stress and strain gradients in fatigue life estimation. Consideration of stress and strain gradient effects (notch geometric effects) explicitly in the fatigue damage

models is essential to also account for the sensitivity of the stress and strain gradients in fatigue life estimation. There are no studies on the explicit approach in the literature, and is a focus of the current study.

CHAPTER 3

COMPUTATIONAL MODELING

SAE 1045 notched shaft is used to study the fatigue life estimations of notched components under multiaxial loadings. FE model of notched shaft is developed using ANSYS Mechanical APDL 15.0 [63]. Multilinear kinematic hardening plasticity model is used to perform the elastic-plastic stress-strain analysis to determine notch stress-strain histories, which is used for fatigue life estimations. An existing multiaxial fatigue damage model, the Fatemi-Socie model, which estimates fatigue life accurately for smooth specimens under multiaxial loadings, is modified to accurately estimate fatigue lives of notched components under multiaxial loadings. A computational multiaxial fatigue analysis design model is developed by integrating the proposed damage model with FEA. Figure 3-1 shows the modelling and analysis methodology adopted in this work.

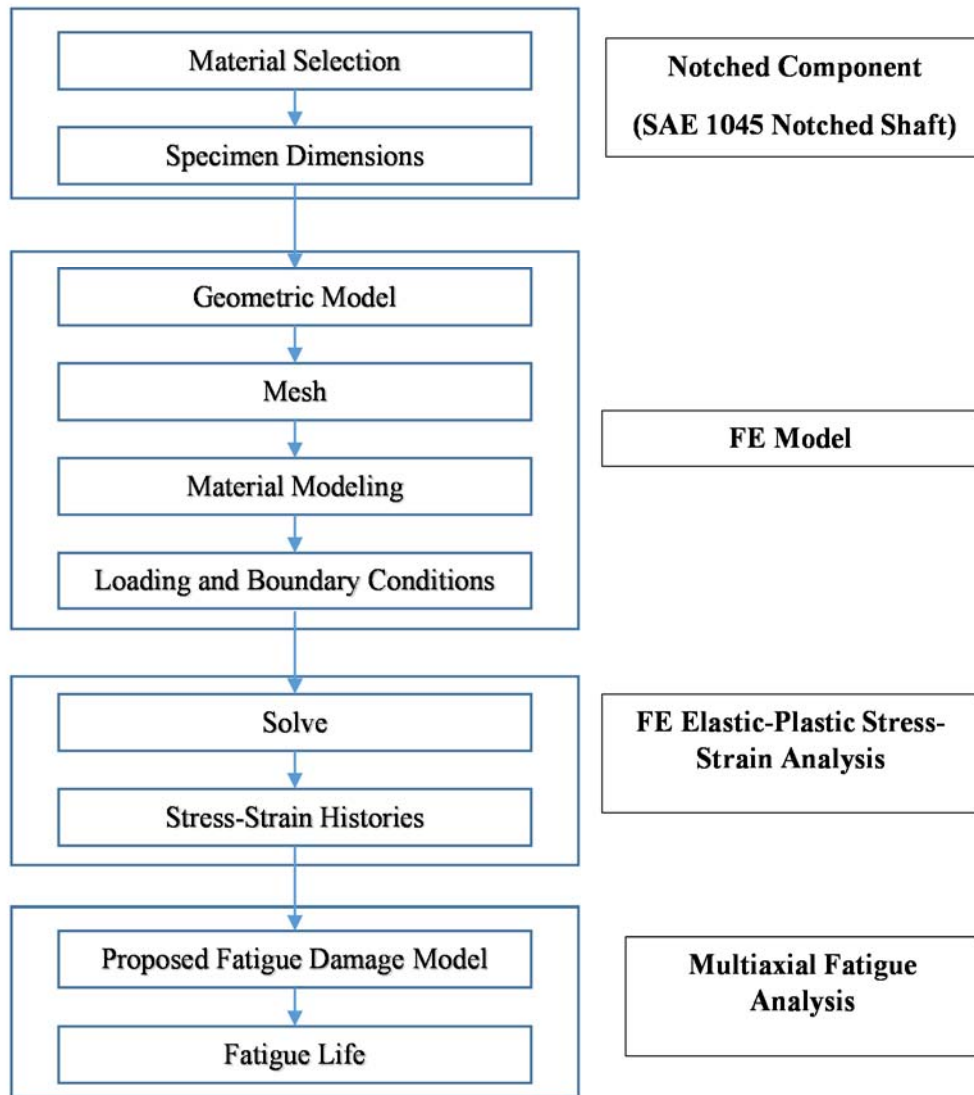


Figure 3-1: Modelling and analysis methodology.

3.1 Notched Component

SAE 1045 notched shafts have been tested previously in benchmark testing program as already discussed in Chapter 1. During the benchmark testing, the notched shafts were

subjected to combined bending-torsion loadings representing a realistic engineering component in service. Therefore, it is selected for this study as a representative notched component.

Following laboratories have contributed in the SAE 1045 notched shaft benchmark testing program [51]:

- University of Illinois (IL)
- Deere and Company (JD)
- Rexnord Corporation (RN)
- O. Smith Corporation (AOS)
- Battel Columbus (BC)
- Guest, Keen and Wettelfolds (GKN)

3.1.1 Material

In the benchmark testing program carried out by SAE, SAE 1045 hot-rolled steel was used to manufacture the notched shafts, and thus is named as SAE 1045 notched shaft [10]. The material was first prepared in the form of 64 mm diameter bars from a single heat, then was normalized in 61 m lots so that mechanical properties variability be reduced [10]. Table 3-1 lists monotonic and cyclic fatigue properties of SAE 1045 steel. The cyclic fatigue properties are to be used for estimating lives to crack initiation [53].

Table 3-1: Monotonic and cyclic fatigue properties of SAE 1045 steel [10].

Monotonic Properties	
Yield Stress (0.2%), S_Y	380 MPa
Ultimate Strength, σ_u	621 MPa
Monotonic Strength Coefficient, K	1185 MPa
Monotonic Strain Hardening Exponent, n	0.23
Modulus of Elasticity, E	204 GPa
Shear Modulus, G	80.3 GPa
Cyclic Axial Fatigue Properties	
Cyclic Axial Strength Coefficient, K'	1258 MPa
Cyclic Axial Strain Hardening Exponent, n'	0.208
Axial Fatigue Strength Coefficient, σ'_f	948 MPa
Axial Fatigue Strength Exponent, b	-0.092
Axial Fatigue Ductility Coefficient, ϵ'_f	0.260
Axial Fatigue Ductility Exponent, c	-0.445
Cyclic Torsional Fatigue Properties	
Cyclic Torsional Strength Coefficient, K'_o	614 MPa
Cyclic Torsional Strain Hardening Exponent, n'_o	0.217
Torsional Fatigue Strength Coefficient, τ'_f	505 MPa
Torsional Fatigue Strength Exponent, b_s	-0.097
Torsional Fatigue Ductility Coefficient, γ'_f	0.413
Torsional Fatigue Ductility Exponent, c_s	-0.445

3.1.2 Specimen Dimensions

The SAE 1045 notched shaft geometry dimensions are shown in Figure 3-2.

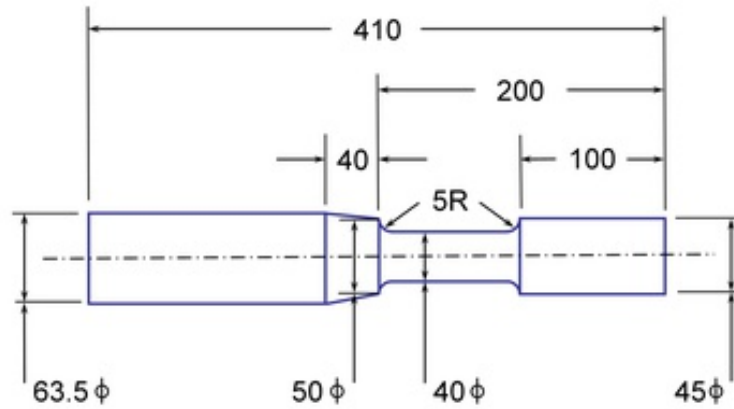


Figure 3-2: SAE 1045 notched shaft specimen dimensions [7].

3.1.3 Benchmark Dataset

Table 3-2 shows the benchmark dataset published by Kurath et al [10]. These loading data are used in the current work.

Table 3-2: Benchmark Dataset [7,10].

Specimen ID *	Loading	Bending Moment, M_b (Nm)	Torsional Moment, M_t (Nm)	$N_{1.0mm}$ (Cycles)	N_f (Cycles)
JD-BR3-1	Bending	2800	0	2,571	8,262
IL-BR3-2		2600	0	3,000	13,760
AOS-BR3-1		2600	0	7,930	13,060
JD-BR3-2		2600	0	8,111	18,310
AOS-BR3-2		2586	0	14,000	17,450
JD-BR2-1		1875	0	41,360	106,700
BC-BR2-1		1875	0	55,000	117,700
RN-BR2-1		1730	0	30,000	83,600
IL-BR2-2		1730	0	49,200	132,300
IL-BR2-1		1730	0	60,000	184,300
AOS-BR2-1		1730	0	130,000	228,300
AOS-BR2-2		1708	0	163,800	249,900
AOS-BR1-1		1475	0	230,000	403,800

AOS-BR1-2		1460	0	430,000	764,000	
JD-BR1-1		1475	0	464,000	709,000	
IL-BR1-1		1400	0	4,494,000	-	
JD-TR3-1	Torsion	0	3000	4,057	9,528	
IL-TR3-1		0	3000	7,000	14,720	
BC-TR2-1		0	2400	65,000	101,100	
IL-TR2-1		0	2400	75,700	164,070	
GKN-TR1-1		0	2000	700,000	2,000,000	
RN-TR1-1		0	2000	750,000	1,293,000	
IL-TR1-1		0	2000	1,584,000	2,238,000	
JD-TR0-1		0	1700	2,324,000	-	
JD-TR0-2		0	1500	1,515,000	-	
IL-XR3-1		In-phase	1850	2550	2,200	5,113
RN-XR3-1			1850	2100	4,780	11,630
IL-XR3-2			1850	2100	6,700	11,500
IL-XRN-1	1355		2550	5,500	11,630	
JD-XR3-1	2000		2100	5,998	12,050	
RN-XR2-1	1220		1700	60,800	124,500	
IL-XR2-1	1220		1710	72,000	163,700	
JD-XR2-1	1220		1710	107,500	158,100	
RN-XR1-1	990		1390	350,000	587,000	
IL-XR1-1	990		1390	933,000	1,194,000	
IL-XRN-1	725		1390	2,000,000	-	
IL-XR2-2	1550		1090	97,500	220,500	
IL-YR2-2	1550		1090	80,000	159,900	
IL-YR3-1	2325		1350	2,810	11,380	
IL-YR3-2	2325		1350	3,000	12,090	
IL-YR3-1	1720		1350	17,070	51,780	
IL-YR3-2	1720		1350	21,450	65,800	
BC-YR2-1	1680		960	30,000	65,049	
JD-YR1-1	1680		900	84,950	153,800	
JD-YR1-1	1300		1400	84,680	226,000	
RN-YR1-1	1250		880	325,000	747,000	
IL-YR1-1	1250		880	600,000	722,500	
IL-YRN-1	1150		1090	2,294,000	-	
IL-YRN-2	1150		1090	2,381,000	-	
IL-ZR3-1	1150		2700	3,000	12,700	

JD-ZR3-1		1250	2700	6,402	10,420
IL-ZR3-1		851	2700	9,000	17,730
IL-ZR3-2		840	2700	10,000	24,540
IL-ZR2-1		780	2180	70,000	142,700
IL-ZR2-2		780	2180	70,680	169,500
IL-ZR2-3		570	2180	76,100	177,800
IL-ZR2-4		570	2180	99,560	186,700
JD-ZR2-1		845	1800	259,900	396,800
IL-ZRN-2		460	1760	2,350,000	-
IL-ZRN-1		460	1760	3,027,000	-
JD-ZR03-1		90° out-of-phase	1150	2700	10,600
JD-XR03-1	1850		2100	12,660	27,470
JD-XR03-2	1800		2100	21,600	24,620
BC-XR03-1	1698		2242	6,725	10,840
JD-YR03-1	2300		1325	17,720	23,980
JD-ZR03-2	770		2180	151,900	157,100
BC-XR03-1	1295		1710	25,580	45,580
JD-XR02-1	1220		1710	157,500	213,800
JD-XR02-2	1220		1710	173,300	266,200
JD-XR01-1	985		1400	>1,000,000	-

* Specimen Identification Code: XX-YYY-Z

XX = Laboratory Conducting Test **

YY = Loading Case ***

Z = Specimen Number

** IL = University of Illinois

JD = Deere & Co.

RN = Rexnord Corp.

AOS = A. O. Smith Corp.

BC = Battelle Columbus Lab

GKN = Guest, Keen, and Nettelfolds, UK

*** BR = Pure bending loading

TR = Pure torsion loading

XR = Shear and tensile stress are equivalent (distortion energy theory)

YR = Shear stress is one half of equivalent tensile stress (distortion energy theory)

ZR = Shear stress is twice the equivalent tensile stress (distortion energy theory)

3.2 FE Model

ANSYS Mechanical APDL 15.0 [63] is used for modelling the SAE 1045 notched shaft. The details of the FE model are described below.

3.2.1 Geometric Model

The geometric model is made according to the notched specimen dimensions except for the left gripping end as shown in Figure 3-3. The left gripping end remains fixed so it is not modelled. The final geometric model of notched shaft is shown in Figure 3-4.

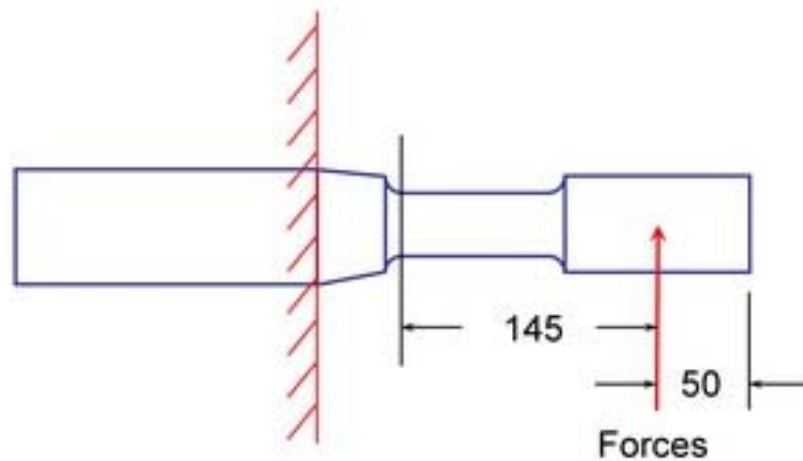


Figure 3-3: Schematic for modelling of gripping ends [7].

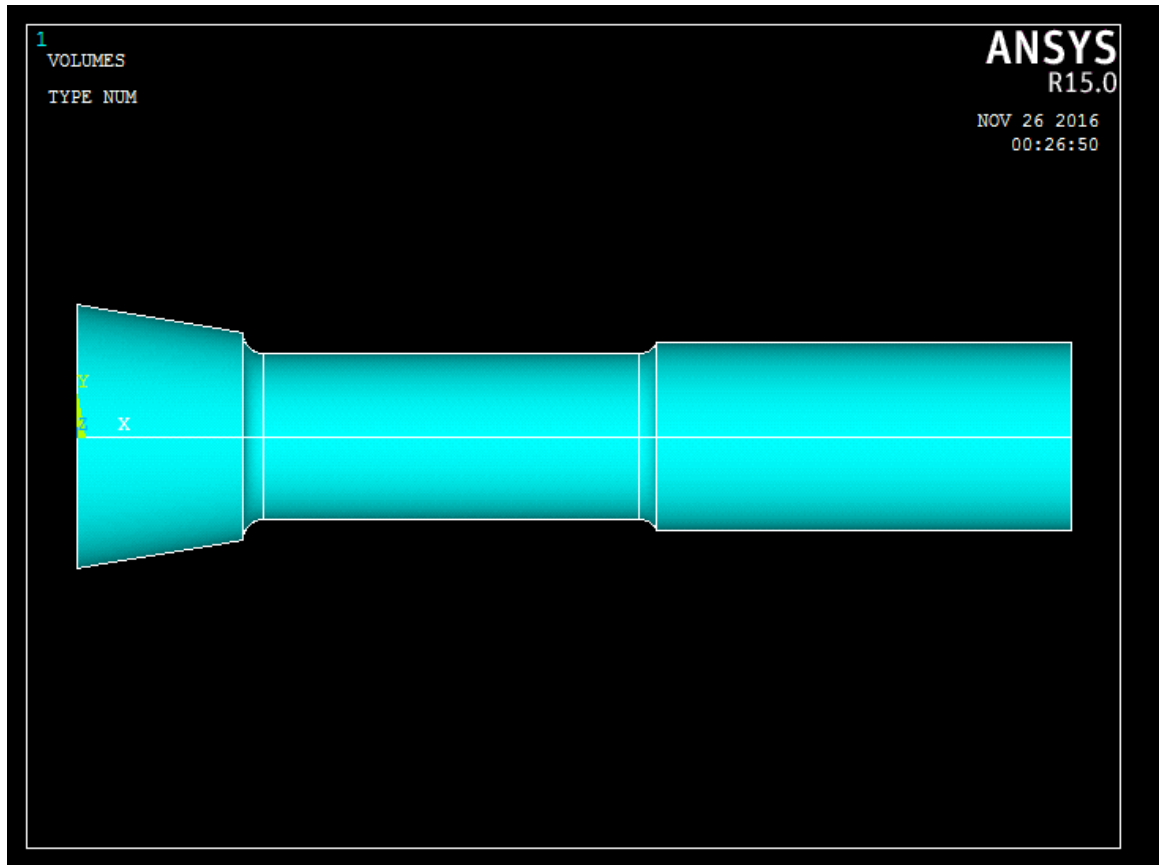


Figure 3-4: Final geometric model of SAE notched shaft.

3.2.2 Mesh

In first attempt, the constructed model was meshed using mapped meshing technique, first using SOLID185 brick element and then using SOLID186 brick element. But ANSYS issued an error during meshing, “Volume has invalid topology for mapped brick meshing”, using both the element types. This is because of the geometry of the notch region which is difficult to be meshed with mapped brick meshing technique. In second attempt, the model was meshed using sweep command with hexahedral elements (SOLID185 and SOLID186

brick elements). But ANSYS again issued warning by using a fine meshing in the notch region, “Shape testing revealed that some of the new or modified elements violate shape warning limits”, using both element types. This is again because of the geometry of the notch region which is difficult to be meshed with hexahedral elements. Hence, the model was meshed using the automatic free meshing techniques and mesh refinement in the notch region.

The constructed model was meshed using SOLID187 elements with automatic free meshing techniques at different scales. The loading scenario of JD-XR3-1 specimen is considered, from the set of load data shown in Table 3-2, for mesh convergence. The selected loading is an in-phase multiaxial load with both high bending and torsional moments. Instead of using the loading as a sinusoidal cyclic load, the loading is applied as a static load with magnitude equal to that of the amplitude of the cyclic load. As summarized in Table 3-3 and Figure 3-5, the mesh of the constructed model was refined 5 times and solved to get convergence. The solution of each meshed model was compared on basis of maximum von-Mises stress at the notch root. As can be seen in Table 3-3, Mesh-4 and 5 have around 2.5 and 6 times the number of elements of the Mesh-3 respectively, while there is a very little difference between their maximum von-Mises values, hence the convergence is achieved. The Mesh-3 is taken as the final mesh, as shown in the Figure 3-6, which is the meshing with 28,156 elements.

Table 3-3: Mesh convergence of the model.

Mesh No.	No. of Elements	No. of Nodes	Max. von Mises Stress
Mesh-1	7335	13181	357.6
Mesh-2	8322	14896	356.3
Mesh-3	28156	44407	363.6
Mesh-4	74176	110318	365.1
Mesh-5	173370	249521	365.7

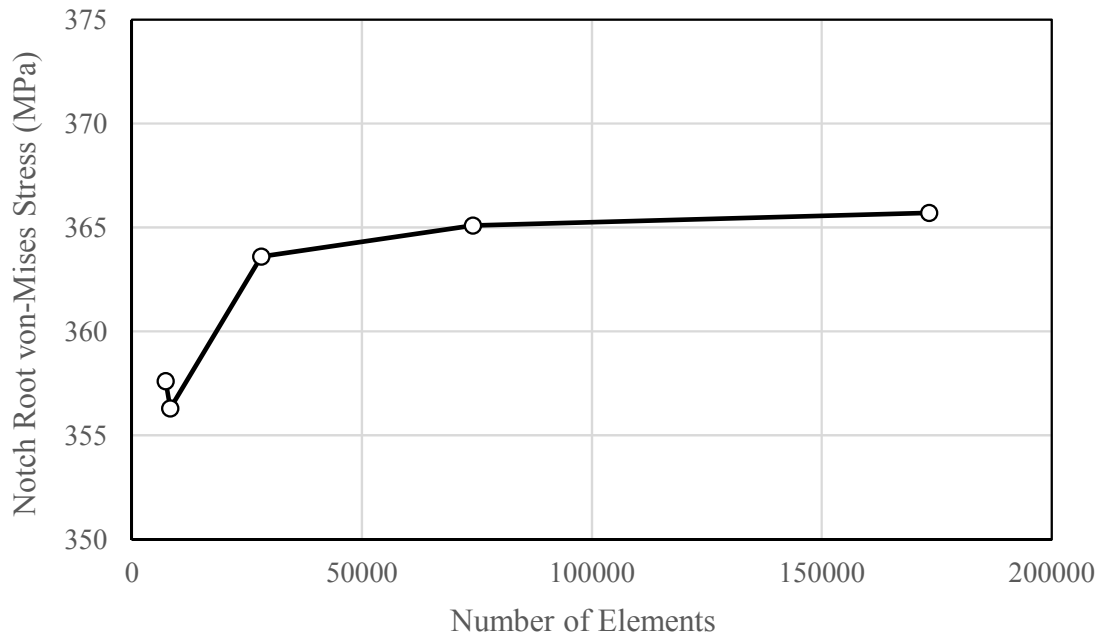
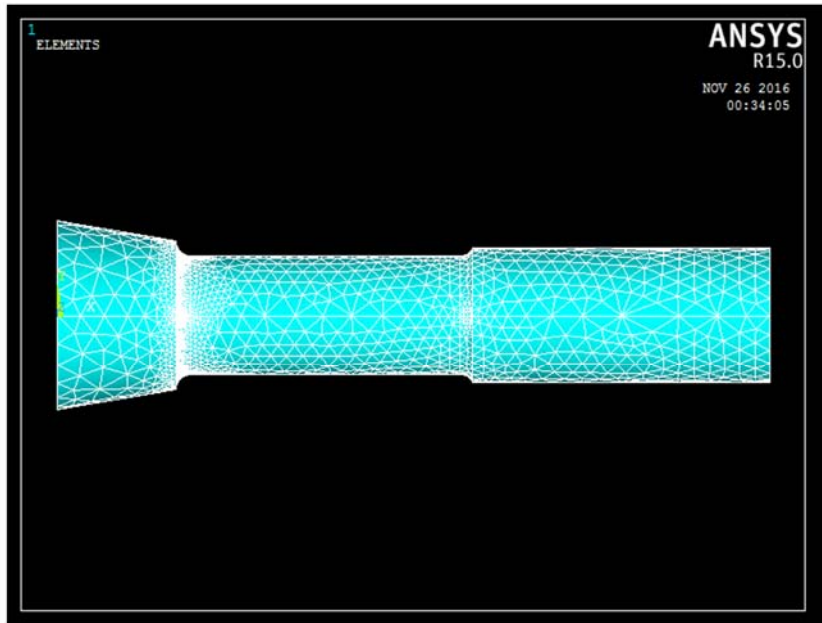
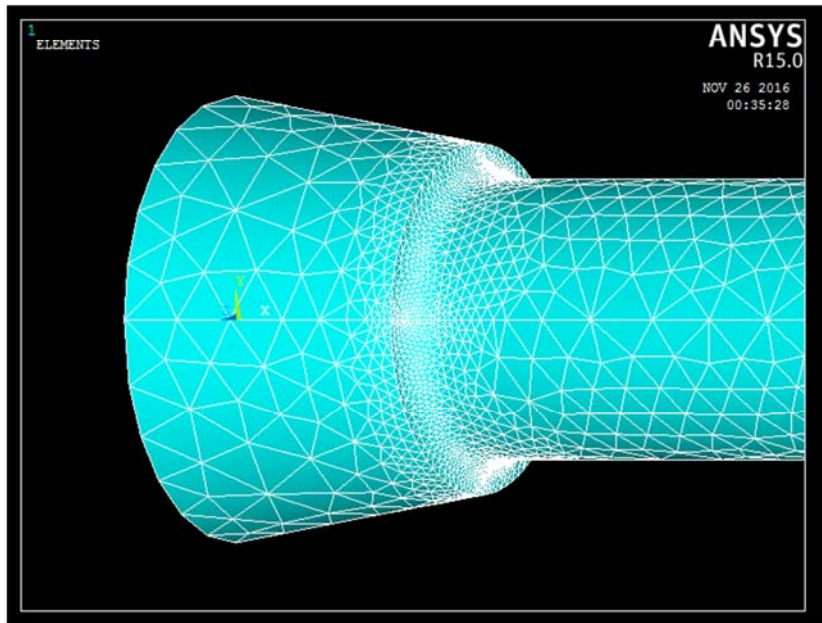


Figure 3-5: Mesh convergence of the model.



(a)



(b)

Figure 3-6: Final mesh of SAE 1045 notched shaft; (a) Whole model, (b) Magnified notch region.

3.2.3 Material Modelling

Multilinear kinematic hardening (KINH) is used for material modelling of the SAE 1045 notched shaft in ANSYS. For multilinear kinematic hardening, the backstress tensor evolves such that the stress-total strain curve is multilinear with the linear segments defined by user-input stress-strain data [64], as shown in the Figure 3-7. In Figure 3-7, σ_0 corresponds to the yield stress of the material.

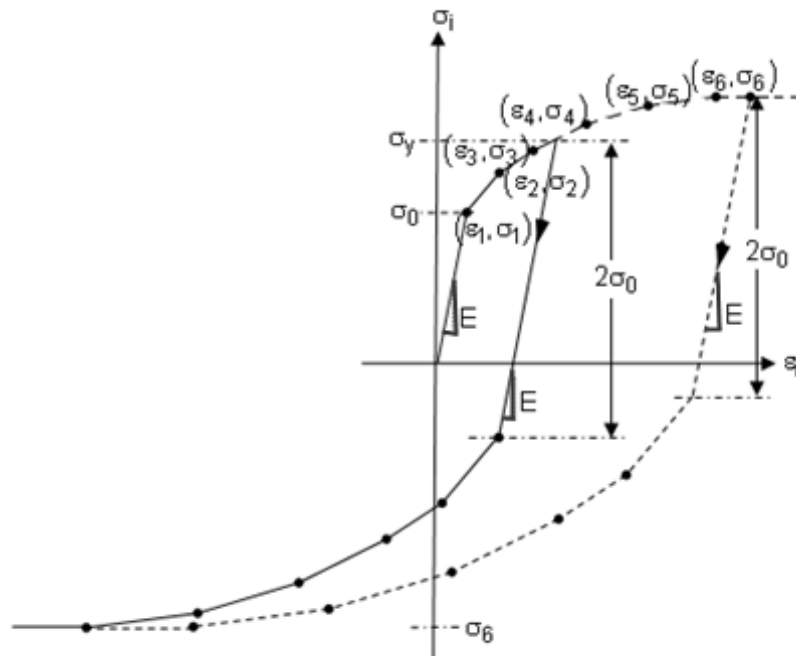


Figure 3-7: Stress-total strain curve for multilinear kinematic hardening [64].

The formulation of the model is based on sublayer model of Besseling [65] and Owen, Prakash & Zienkiewicz [66]; in which the material is considered to be composed of a number of sublayers, all under the same total strain [64]. The number of sublayers is the

same as the number of user-input stress-strain data points, and the overall behavior is weighted for each sublayer, and the weight is mathematically expressed as [64]:

$$w_k = \frac{E - E_{Tk}}{E - \frac{1-2\nu}{3}E_{Tk}} - \sum_{i=1}^{k-1} w_i \quad (3-1)$$

Here E_{Tk} is tangent modulus for segment of the stress-strain curve.

The uniaxial yield stress for each sublayer is given as [64]:

$$\sigma_{Tk} = \frac{1}{2(1+\nu)} (3E\varepsilon_k - (1-2\nu)\sigma_k) \quad (3-2)$$

where $(\varepsilon_k, \sigma_k)$ is the input stress-strain point for sublayer k .

A von-Mises yield criterion is used and each sublayer yields at an equivalent stress equal to the sublayer uniaxial yield stress.

Also, the total plastic strain is given as [64]:

$$d\varepsilon^{pl} = \sum_{i=1}^{N_{SV}} w_i d\varepsilon_i^{pl} \quad (3-3)$$

where $d\varepsilon_i^{pl}$ is sublayer plastic strain increment and N_{SV} is number of sublayers.

K' and n' values from Table 3-1 are used in Ramberg-Osgood equation, Eq. (3-4), to create true stress-total strain data to be stored in multilinear kinematic hardening model:

$$\varepsilon_t = \frac{\sigma}{E} + \left(\frac{\sigma}{K}\right)^{\frac{1}{n}} \quad (3-4)$$

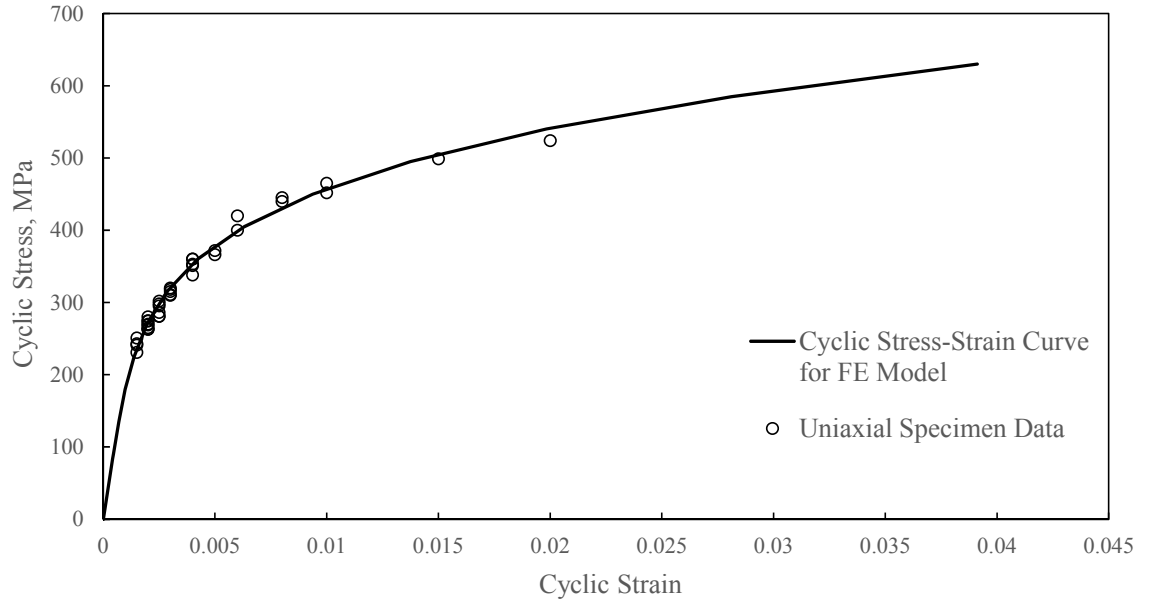


Figure 3-8: Modeling of cyclic stress-strain curve of normalized 1045 steel for the cyclic plasticity model.

As can be seen in the Figure 3-8, the cyclic stress-strain curve used for the FE model fits well with the experimental uniaxial specimen data of normalized 1045 steel [10].

3.2.4 Loading and Boundary Conditions

The bending and torsional loads were distributed in 24 load steps in order to get a smooth hysteresis. The bending moment was modelled using a bending force given as:

$$\text{Bending Force} = \frac{\text{Bending Moment } (M_b)}{\text{Length from Load Point to Notch Root}} \quad (3-5)$$

The torsional moment was modelled using four forces to produce a torsional effect:

$$\text{Torsional Force} = \frac{\text{Torsional Moment } (M_t)}{4 \times \text{Radius of Shaft at Load Point}} \quad (3-6)$$

Figure 3-3 shows the location of the geometric model where bending and torsional forces were applied. The manner in which the bending and torsional loads are applied is shown in the Figure 3-9 (cross-sectional view, 145 mm from notch root). The bending load is applied as a shear force shown by a black arrow, while the torsional load is applied as two couples shown by orange arrows.

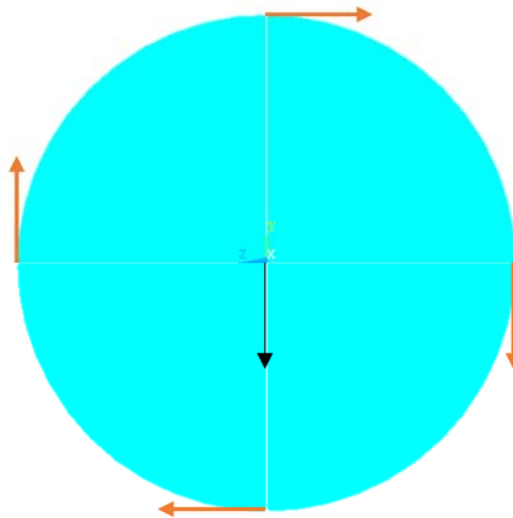


Figure 3-9: Manner of load applications.

Figure 3-3 shows the location where the geometric model was fixed in all directions. Figure 3-10 shows the manner in which the left end face of the constructed model is fixed in all directions.

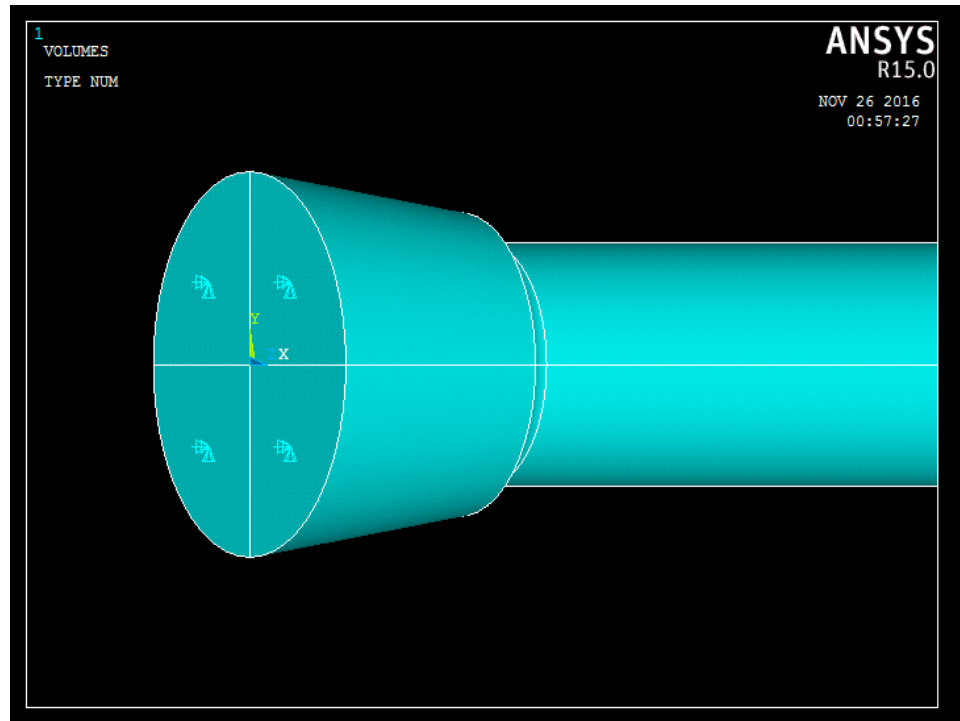


Figure 3-10: Fixed end at the left end face of the constructed model.

3.3 Elastic-Plastic Stress-Strain Analysis

The developed ANSYS model is used to obtain elastic-plastic stress analysis of the notched shaft. The SAE 1045 notched shaft was designed to fail at the notch root under a variety of multiaxial loadings [10]. Therefore, the notch root is taken as the critical point. In addition, the point of maximum von-Mises stress was also used for fatigue analysis.

The local stress-strain histories at the notch root and maximum von-Mises location were obtained and exported in CSV files to be read by MATLAB code for fatigue damage calculations and fatigue life estimations.

3.4 Modelling of Fatigue Analysis

A fully automated MATLAB code has been written from scratch for this work, which is capable of doing multiaxial fatigue analysis on both smooth and notched specimens. It asks the user to import static, cyclic and multiaxial stress-strain data in the form of excel files, and then do all types of static and fatigue analysis automatically and provide the final results in the form of plots and stores all the results in an output excel file.

Flowchart of MATLAB code is shown in Figure 3-11. The MATLAB code is capable of:

- Determining the static material properties using monotonic stress-strain data
- Determining cyclic axial and torsion fatigue properties for axial and torsion strain-life curves, respectively
- Determining cyclic axial and torsion fatigue properties for axial and torsion energy-life curves, respectively
- Performing critical plane analysis for determining the most critical damaging plane for use in critical plane based fatigue damage models
- Determining cyclic axial and torsional strain components (elastic and plastic) for use in strain based fatigue damage models
- Determining cyclic axial and torsional energy components (elastic and plastic) for use in energy based fatigue damage models

- Calculating damage values for different fatigue damage models and estimating the corresponding fatigue lives
- Selecting the best fatigue damage model using the proposed criterion
- Estimating fatigue life for both smooth and notched specimens
- Estimating fatigue life for notched components with a better accuracy using the proposed modification in the Fatemi-Socie model
- Accommodating new fatigue damage models easily

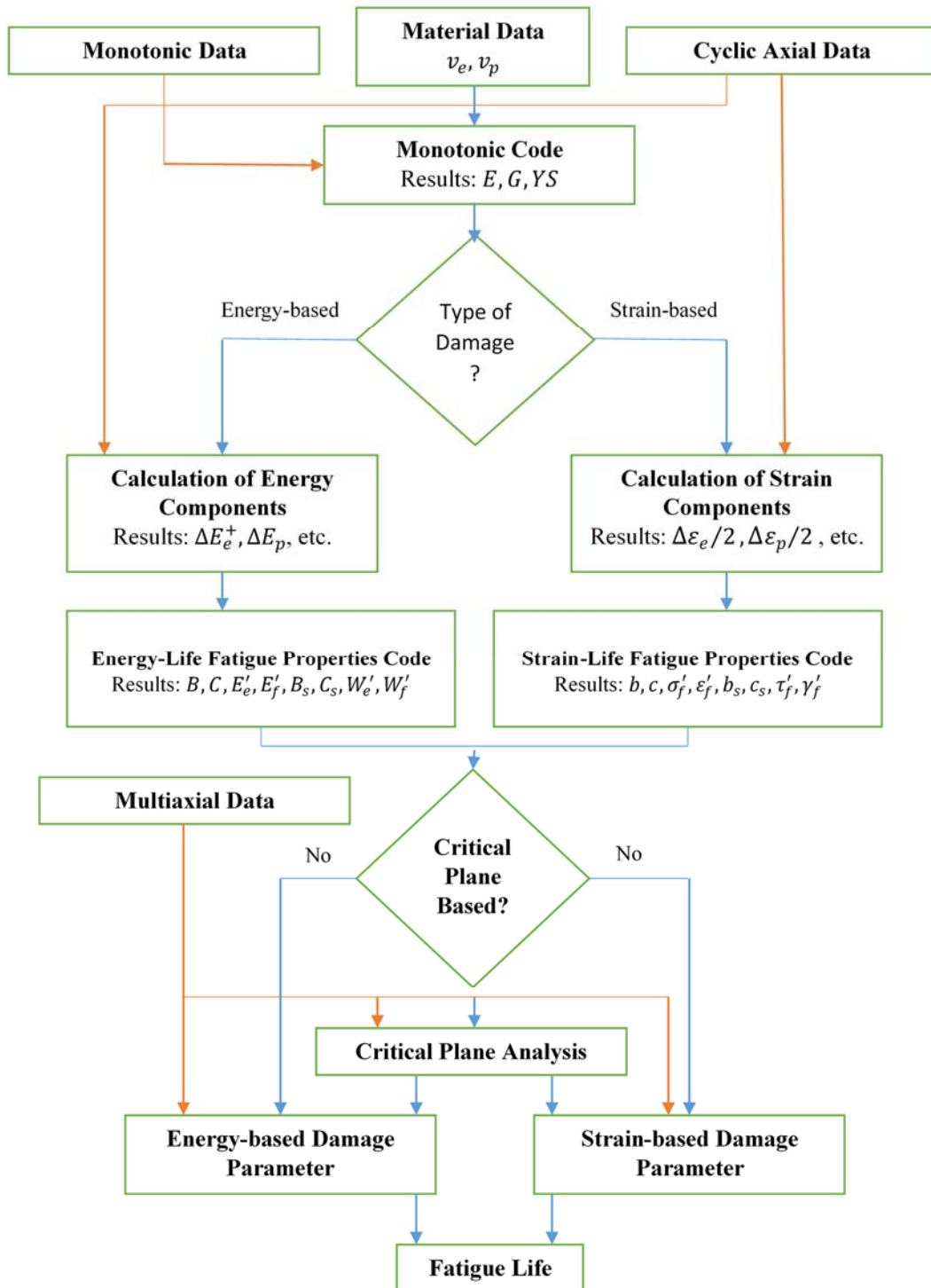


Figure 3-11: Flowchart of MATLAB code.

3.4.1 Static Material Properties

The monotonic tensile properties are determined according to the methods suggested by E8/E8M ASTM standard [67]. The tensile yield strength is determined using the offset method at an offset of 0.2%. The ultimate tensile stress is found as the maximum stress in the monotonic tensile stress-strain data.

The monotonic compressive properties are determined according to the methods suggested by E9 ASTM standard [68]. The compressive yield strength is determined using the offset method at an offset of 0.2%. The ultimate compressive stress is found as the maximum stress in the monotonic compressive stress-strain data.

The elastic modulus is determined as the slope of the stress-strain curve within the proportional limit. The shear modulus is determined using the following relation [17]:

$$G = \frac{E}{2(1 + \nu)} \quad (3-7)$$

3.4.2 Cyclic Fatigue Properties

Cyclic Fatigue Properties For Strain-Life Curve

The cyclic axial fatigue properties for strain-life curve are determined using the axial strain based Coffin-Manson equation Eq. (2-20). They are determined according to the method shown in Figure 2-6. In the same manner, the cyclic shear fatigue properties for

strain-life curve are determined using the shear strain based Coffin-Manson equation Eq. (2-27).

Cyclic Fatigue Properties For Energy-Life Curve

The cyclic axial fatigue properties for energy-life curve are determined using the axial energy based Coffin-Manson equation Eq. (2-34). Similarly, the cyclic shear fatigue properties for energy-life curve are determined using the shear energy based Coffin-Manson equation Eq. (2-35). Figure 2-11 shows an illustration for determining the cyclic fatigue properties of energy-life curve.

3.4.3 Critical Plane Analysis

Critical Plane Analysis for Smooth Specimens

Critical plane analysis is used to determine the critical damaging planes. The critical plane analysis of smooth specimens is done using stress and strain transformation equations Eqs. (2-56), (2-57), (2-58) and (2-59). For axial-torsional multiaxial loading, as shown in Figure 3-12, σ_y is the axial stress history, τ_{xy} is the shear stress history, ε_y is the axial strain history and γ_{xy} is the shear strain history. There is no stress along the x-axis, so $\sigma_x = 0$ and ε_x is determined as:

$$\varepsilon_x = -v_e \frac{\sigma_y}{E} - v_p \left(\varepsilon_y - \frac{\sigma_y}{E} \right) \quad (3-8)$$

The value of θ is varied from $0 - 180^\circ$ with an increment of 1° , and maximum axial and shear strain planes or material planes are determined, to be used in critical plane based multiaxial fatigue damage models.

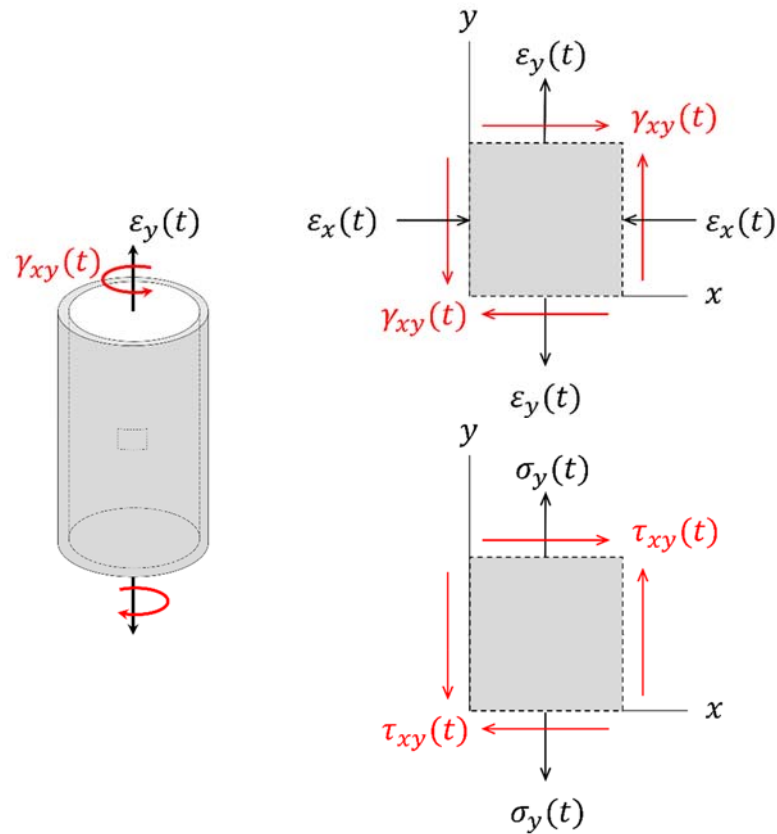


Figure 3-12: Strain-controlled axial-torsional multiaxial loading [69].

Critical Plane Analysis for Notched Components

The critical plane analysis of notched components is done using stress and strain transformation equations Eqs. (2-62), (2-63) and (2-66). The stress and strain time-history tensors are transformed to the potential plane using two angles, θ and ϕ . Figure 3-13 shows

the defined Cartesian coordinate system. The potential plane is reached by first rotating xy-plane clockwise about z-axis by an angle of θ and then by rotating anticlockwise about y-axis by an angle of ϕ . The θ and ϕ plane rotations are shown in Figure 3-14. The critical plane is determined by varying both θ and ϕ from $0 - 180^\circ$ with an increment of 1° .

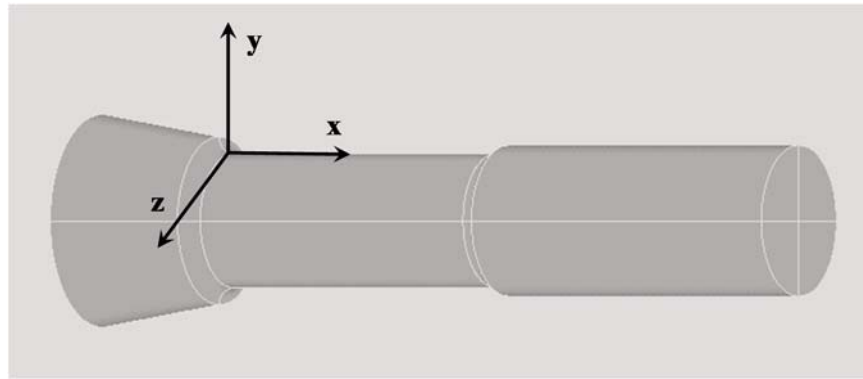


Figure 3-13: Defined Cartesian coordinate system at the notch root.

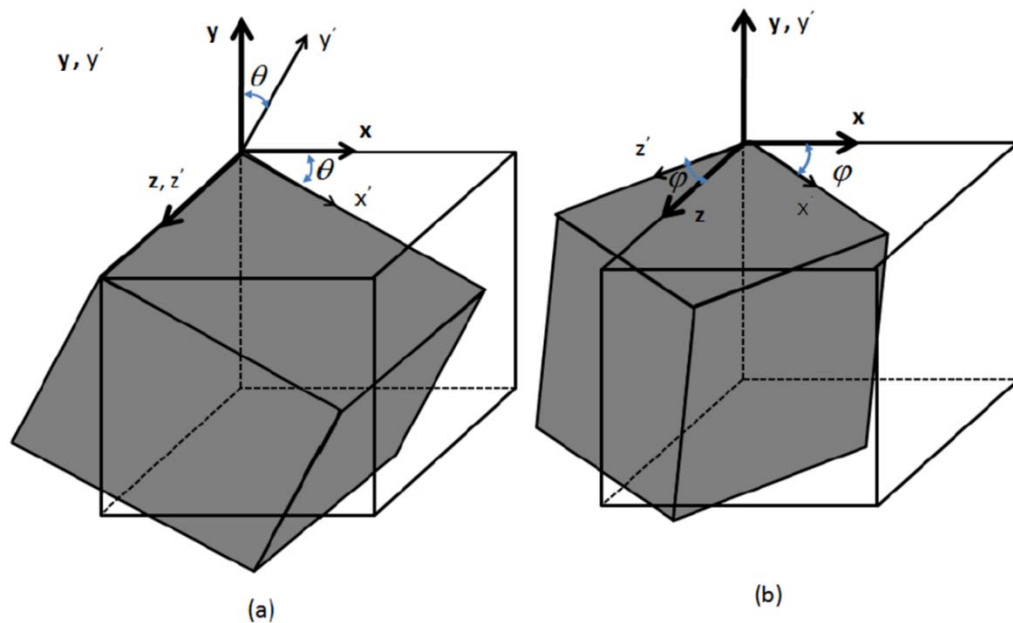


Figure 3-14: Plane rotations; (a) θ rotation about z-axis, (b) ϕ rotations about y-axis [70].

From Figure 3-13, it can be seen that y-axis is normal to the notch surface, so the stress in the y-direction is zero. Thus, the notch root has a biaxial stress state and a triaxial strain state, as shown in the Figure 3-15.

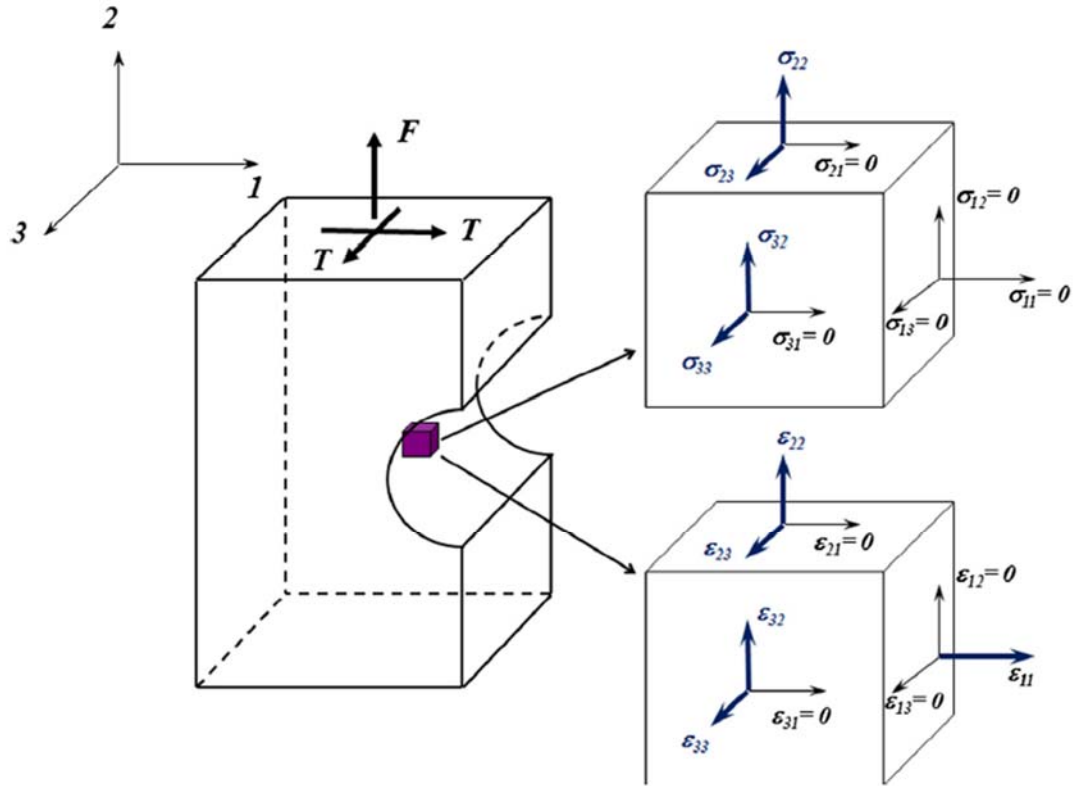


Figure 3-15: State of stress and strain at the notch root [35].

3.4.4 Fatigue Damage Models

Fatemi-Socie Model for Smooth Specimens

The code determines the plane of maximum shear strain using critical plane analysis. Then it transform the stress-strain histories at this maximum shear strain plane to calculate

the damage values, which are used for fatigue life estimation. The code also determines the material constant k by fitting the fatigue damage values of cyclic axial and cyclic torsion on a damage versus life plot. Then, the only unknown variable in the nonlinear equation Eq. (2-31) is N_f , which the code determines by solving it using Newton-Raphson method.

Smith-Watson-Topper Model for Smooth Specimens

The code determines the plane of maximum normal strain using critical plane analysis. Then it transform the stress-strain histories at this maximum normal strain plane to calculate the damage values, which are used for fatigue life estimation. Then, the only unknown variable in the nonlinear equation Eq. (2-32) is N_f , which the code determines by solving it using Newton-Raphson method.

Jahed-Varvani Model for Smooth Specimens

The code determines the axial and shear elastic and plastic energy densities to calculate the total energy density in order to be used for fatigue life estimation. The only unknown variables in the nonlinear equation Eqs. (2-34) and (2-35) are N_A and N_T respectively, which the code determines by solving them using Newton-Raphson method. The determined value of N_A and N_T is used in Eq. (2-33) to determine the value of N_f .

The code can also use Jahed-Varvani model as a critical plane based model to estimate fatigue lives. The critical plane can be defined as either the maximum total energy plane, or as maximum axial energy plane or as maximum shear energy plane.

Fatemi-Socie Model for Notched Components

Das et al. [50] have studied the SAE 1045 notched shaft and have found that the critical plane based fatigue damage models gives better fatigue life estimations when used at the plane which provides the maximum damage rather than the plane provides the maximum strain range. Thus, the Fatemi-Socie damage parameter for the SAE notched is calculated at the maximum damage plane in order to get better fatigue life estimations.

For a plane stress state as shown in Figure 3-16, two Fatemi-Socie fatigue damage parameters can be calculated in the following forms:

$$FP_1 = \frac{\Delta\gamma_{xy,max}}{2} \left(1 + k \frac{\sigma_{x,max}}{\sigma_{yt}} \right) \quad (3-9)$$

$$FP_2 = \frac{\Delta\gamma_{xy,max}}{2} \left(1 + k \frac{\sigma_{y,max}}{\sigma_{yt}} \right) \quad (3-10)$$

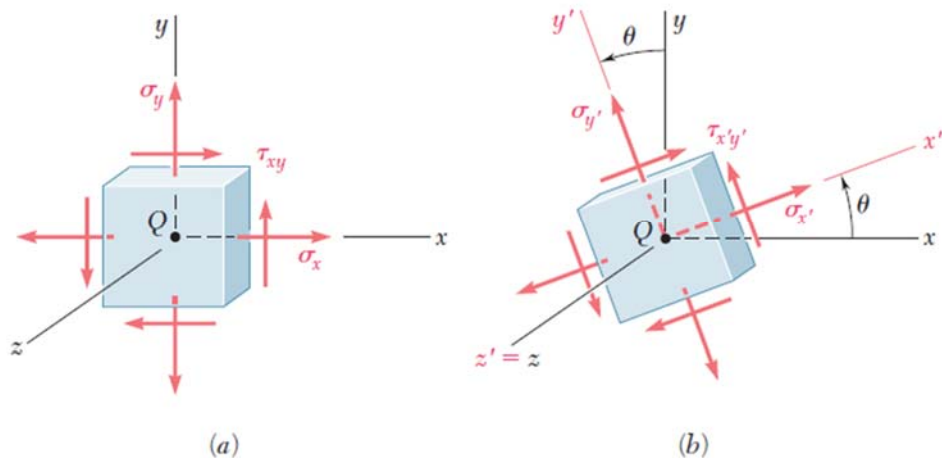


Figure 3-16: Plane stress transformation [34].

There is no need for calculating both the damage parameters, because both of the damage parameters are 90° out-of-phase with one another, and the critical plane is found by varying θ from 0 to 180°. For example, when σ_x is varied by 90° it becomes σ_y , and vice versa. So, by varying the angle from 0 to 180° all possible planes are taken into account and so any of the two damage parameter is enough for the critical plane analysis. The critical plane analysis is done by considering the damage parameters FP_1 in Eq (3-9). This logic can also be extended to three dimensional critical plane analysis. For a three dimensional stress state as shown in Figure 3-17, six Fatemi-Socie fatigue damage parameters can be calculated in the following forms:

$$FP_1 = \frac{\Delta\gamma_{xy,max}}{2} \left(1 + k \frac{\sigma_{x,max}}{\sigma_{yt}} \right) \quad (3-11)$$

$$FP_2 = \frac{\Delta\gamma_{xz,max}}{2} \left(1 + k \frac{\sigma_{x,max}}{\sigma_{yt}} \right) \quad (3-12)$$

$$FP_3 = \frac{\Delta\gamma_{xy,max}}{2} \left(1 + k \frac{\sigma_{y,max}}{\sigma_{yt}} \right) \quad (3-13)$$

$$FP_4 = \frac{\Delta\gamma_{yz,max}}{2} \left(1 + k \frac{\sigma_{y,max}}{\sigma_{yt}} \right) \quad (3-14)$$

$$FP_5 = \frac{\Delta\gamma_{yz,max}}{2} \left(1 + k \frac{\sigma_{z,max}}{\sigma_{yt}} \right) \quad (3-15)$$

$$FP_6 = \frac{\Delta\gamma_{xy,max}}{2} \left(1 + k \frac{\sigma_{x,max}}{\sigma_{yt}} \right) \quad (3-16)$$

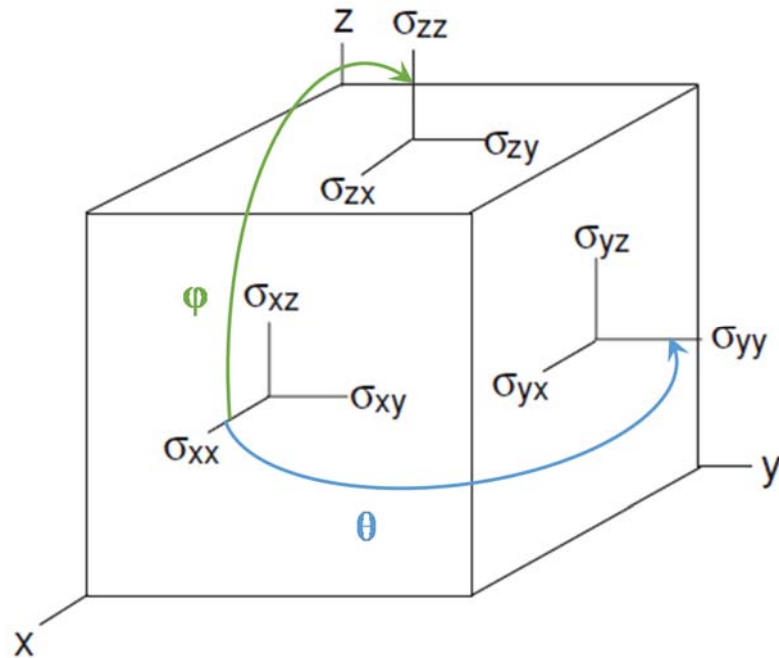


Figure 3-17: Three dimensional stress state [28].

There is no need for calculating all the six damage parameters, only two damage parameters will do the job. This is because by rotating the the yz -plane around z -axis by an angle θ of 90° , σ_x becomes σ_y , σ_{xz} becomes σ_{yz} , σ_{xy} is already equal to $-\sigma_{yx}$; and vice versa. Similarly, by rotating the the xz -plane around x -axis by an angle ϕ of 90° , σ_x becomes σ_z , σ_{xy} becomes σ_{zy} , σ_{xz} is already equal to $-\sigma_{zx}$; and vice versa. As the critical plane is found by varying θ and ϕ from 0 to 180° by increments of 1° , thus all the possible planes are taken into account and so only two damage parameters is enough for the critical plane analysis. The critical plane analysis is done by considering the damage parameters FP_1 and FP_2 in Eqs. (3-11) and (3-12). The specific plane at which the highest damage among the two damage parameters is obtained is considered as the critical plane. Then, the

only unknown variable in the nonlinear equation Eq. (2-31) is N_f , which the code determines by solving it using Newton-Raphson method.

Fatemi & Socie [23] and Fatemi & Kurath [71] have used 0.6 as the value of k for hot-rolled 1045 steel in normalized condition. Chu et al. [36] has also used 0.6 as the value of k for studying the SAE 1045 notched shaft. Thus, the value of k is taken as 0.6 for the SAE shaft in this study.

3.5 Proposed Assessment Method

Many critical plane based fatigue damage models have been developed during last several decades. These developed models propose different damage mechanisms and formulations. They have been shown to estimate fatigue lives within ± 2 and ± 3 factors of life. Although, many critical plane models have been proposed, however there are no methods developed to assess them. Therefore, there is a need to develop some screening method for critical plane models, which can help with selection of damage mechanisms and formulations that have a high chance of improvement in the fatigue life estimation. These selected models should be further studied to close the ± 2 life estimation factor gap.

This study proposes a method to assess the critical plane based fatigue damage models. It can be used as an initial check for the working of the damage model. Critical plane based damage parameter has two aspects: the damage formulation and the evaluation method. The damage is formulated using combination of mechanical damage variables such as

stresses or strains. The evaluation method defines the specific plane(s) where the damage should be calculated. In this method, we assess the correlational-capability of the damage formulation with fatigue life. This method proposes that the damage model should be evaluated at all plane angles, namely, from 0 to 180° with an increment of 1°. In another words, the damage values and the corresponding fatigue lives are calculated at all the plane angles. Out of all these estimated lives, the one closest to the experimental life is selected to gauge the estimation capability of the model. If the selected fatigue life is nearly close to the experimental life, then the model has a chance to successfully estimate life better than ± 2 factor with further studies and improvements. Else, if the damage model fails to estimate life nearly close to the experimental life on all the planes, then it has a very slim chance of estimating life better than ± 2 factor with further studies and improvements. Although this method does not guarantee that the passed damage models will be successful in accurately estimating fatigue lives, however, it does guarantee that the failed models have less chances for successful life estimations.

The proposed assessment method is used to evaluate different fatigue damage models on the basis of smooth tubular specimen data, to select the best model available at the smooth specimen level which will be modified to make accurate fatigue life estimations for notched specimens. Detailed experimental fatigue data is required for evaluating the capability of the proposed method and for determining the best critical plane based model. The experimental multiaxial fatigue data of Albinmoussa et al. [3,72] on extruded AZ31B magnesium alloy, Zhang et al. [73] on extruded AZ61A magnesium alloy, Xiong et al. [2]

on extruded AZ31B magnesium alloy and Hoffmeyer [74] on S460N structural steel alloy were used for evaluating the proposed method. The fatigue testing details, chemical compositions and monotonic properties of the considered alloys are listed in Table 3-4 to Table 3-6, respectively. Different extrusion section geometry (from which the test specimens were made), different extrusion parameters and a little difference in chemical composition might be the source of the difference in mechanical properties of Albinmousa et al. AZ31B and Xiong et al. AZ31B alloys.

Two commonly used strain-based and one energy-based models are compared to select the best model, which will be modified to accurately estimate fatigue lives for notched components. The two strain-based models are Smith-Watson-Topper (normal strain based) and the Fatemi-Socie (shear strain based) models. For the energy-based model, Jahed-Varvani model was used. Although, Fatemi-Socie and Smith-Watson-Topper models are strain-based critical plane models, however instead of evaluating them at the critical plane they are evaluated from 0 to 180° plane angles with increment of 1° to check whether they have a chance to successfully estimate multiaxial fatigue lives beyond ± 2 factor with further studies and improvements. Also, Jahed-Varvani model is originally an energy-based model not based on critical plane approach, however it is also subjected to the proposed method to evaluate its potential as a critical plane based model.

Table 3-4: Fatigue testing details of considered alloys.

Author	Material	Control Mode	Strain Ratio	Loading Paths
Albinmousa et al. [3,72]	Extruded AZ31B Mg Alloy	Strain	Fully Reversed	Cyclic Axial, Cyclic Torsion, Multiaxial Proportional and Nonproportional (45°, 90°)
Zhang et al. [73]	Extruded AZ61A Mg Alloy	Strain	Fully Reversed	Cyclic Axial, Cyclic Torsion, Multiaxial Proportional and Nonproportional (90°)
Xiong et al. [2]	Extruded AZ31B Mg Alloy	Strain	Fully Reversed	Cyclic Axial, Cyclic Torsion, Multiaxial Proportional and Nonproportional (90°)
Hoffmeyer [74]	S460N Structural Steel Alloy	Strain or Load	Fully Reversed	Multiaxial Proportional and Nonproportional (13 different paths)

Table 3-5: Chemical compositions (wt%) of considered alloys.

Author	Material	Composition (wt%)
Albinmousa et al. [3,72]	Extruded AZ31B Mg Alloy	3.1 Al, 1.05 Zn, 0.54 Mn, 0.0035 Fe, 0.0008 Cu, 0.0007 Ni, Balance Mg
Zhang et al. [73]	Extruded AZ61A Mg Alloy	6.5 Al, 0.95 Zn, 0.325 Mn, 0.1 Si, 0.05 Cu, 0.005 Fe, 0.005 Ni, 0.3 Other Impurities, Balance Mg
Xiong et al. [2]	Extruded AZ31B Mg Alloy	2.5-3.5 Al, 0.7-1.3 Zn, 0.3 Si, 0.2 Mn, 0.05 Cu, 0.005 Fe, 0.005 Ni, Balance Mg
Hoffmeyer [74]	S460N Structural Steel Alloy	1.54 Mn, 0.44 Si, 0.27 Ni, 0.18 C, 0.17 V, 0.022 Cr, 0.019 N, 0.016 P, 0.013 Al, 0.009 Cu, 0.001 S, Balance Fe

Table 3-6: Monotonic properties of considered alloys.

Author	Material	E (GPa)	ν	G (GPa)	σ_{yt} (MPa)	σ_{yc} (MPa)	σ_{ut} (MPa)	σ_{uc} (MPa)
Albinmousa et al. [3,72]	Extruded AZ31B Mg Alloy	43.72	0.35	15.54	213.33	108	227.45	364.1
Zhang et al. [73]	Extruded AZ61A Mg Alloy	43.3	0.35	16.4	192	120	279	-
Xiong et al. [2]	Extruded AZ31B Mg Alloy	44.8	0.35	16.9	244	151	298	417
Hoffmeyer [74]	S460N Structural Steel Alloy	208.5	0.3	-	500	-	643	-

The material constant k used in the Fatemi-Socie model for all the considered alloys are listed in Table 3-7. The material constant for AZ31B alloy is taken from Albinmousa et al. [72] and Castro et al. [75], for AZ61A alloy is taken from Yu et al. [5], and for S460N alloy it is taken from Jiang et al. [76].

Table 3-7: Material constant used in Fatemi-Socie model for all the considered alloys.

Author	Material	k
Albinmousa et al.[3,72]	Extruded AZ31B Mg Alloy	0.3
Zhang et al.[73], Yu et al.[5]	Extruded AZ61A Mg Alloy	0.1
Xiong et al.[2], Castro et al.[75]	Extruded AZ31B Mg Alloy	0.17
Hoffmeyer[74], Jiang et al.[76]	S460N Structural Steel Alloy	0.98

The cyclic fatigue properties for all the considered alloys are listed in Table 3-8. These properties are calculated for the Xiong et al. [2] AZ31B and Zhang et al. [73] AZ61A alloys from cyclic strain- and energy-life curves, for both axial and shear modes. The properties of Albinmoussa et al. [3,72] AZ31B and Hoffmeyer [74] S460N alloys are taken from their published work. Hoffmeyer has not published energy-fatigue life properties for S460N alloy, and also because of the unavailability of the cyclic axial and torsion data for the S460N alloy, the energy-fatigue life properties are not calculated. Therefore, the Jahed-Varvani model is not used for estimating the fatigue lives of S460N alloy. Because of the higher concentration of data points within the low- to mid-cycle regimes in all of the Zhang et al. AZ61A and Xiong et al. AZ31B alloy datasets, only fatigue data less than 10^5 cycles are considered to get accurate Coffin-Manson type fittings and to get accurate fatigue life estimations.

The differences between the cyclic fatigue properties of Albinmoussa et al. [3,72] and Xiong et al. [2] extruded AZ31B alloy data is because Albinmoussa et al. determined the properties for a very short range, less than 22×10^3 cycles for cyclic axial and less than 25×10^3 for cyclic torsion. Whereas Xiong et al. properties are calculated for less than 10^5 cycles for both cyclic axial and cyclic torsion data.

Table 3-8: Cyclic fatigue properties of all the considered alloys.

Author	Albinmoussa et al. [3,72]	Zhang et al. [73]	Xiong et al. [2]	Hoffmeyer [74]
Material	Extruded AZ31B Mg Alloy	Extruded AZ61A Mg Alloy	Extruded AZ31B Mg Alloy	S460N Structural Steel Alloy
σ'_f (MPa)	723.5	586.1	394.7	969.6
b	-0.159	-0.153	-0.089	-0.086
ϵ'_f	0.252	1.823	0.484	0.281
c	-0.718	-0.832	-0.706	-0.493
τ'_f (MPa)	142.82	134.92	162.03	463.2
b_s	-0.110	-0.079	-0.096	-0.071
γ'_f	0.131	0.173	0.072	0.224
c_s	-0.427	-0.435	-0.340	-0.422
E'_e (MJ/m ³)	20.29	7.01	2.94	-
E'_f (MJ/m ³)	510.74	924.14	217.70	-
B	-0.440	-0.373	-0.226	-
C	-1.052	-1.001	-0.822	-
W'_e (MJ/m ³)	0.67	0.49	0.68	-
W'_f (MJ/m ³)	27.72	24.64	21.48	-
B_s	-0.242	-0.155	-0.191	-
C_s	-0.560	-0.485	-0.478	-

3.6 Proposed Fatigue Damage Model

The physical basis of the Fatemi-Socie model, shown in Figure 3-18, assumes a constant shear strain and a constant maximum normal stress along the duration of initiation

crack length. This physical basis is true for a smooth specimen, however, for notched components the shear strain and maximum normal stress are not constant because of the notch geometric effects like high stress and strain gradients in the notch region. To modify the Fatemi-Socie damage parameter for notched components, it is suggested that the damage parameter should also include two notch geometric correction factors. One notch geometric correction factor accounts for the notch geometrical effects on the maximum normal stress along the crack normal direction and the other accounts for notch geometrical effects on the shear strain amplitude along the crack. The proposed damaged parameter takes the following form:

$$FP = \frac{\Delta\gamma}{2} \left(1 + k \frac{\sigma_{n,max}}{S_y} + g_1 \right) + g_2 \quad (3-17)$$

where g_1 and g_2 are notch geometric correction factors. The factor g_1 accounts for the geometrical factors along the crack normal, whereas the factor g_2 accounts for the geometrical factors along the crack. These notch geometric correction factors depend on the geometry and loading type. The original Fatemi-Socie parameter already takes into account the material effects, loading effects and some of notch geometric effects like stress and strain concentration using local stress-strain analysis. However, it does not account for other geometric effects like stress and strain gradients that are also caused by the notch geometry.

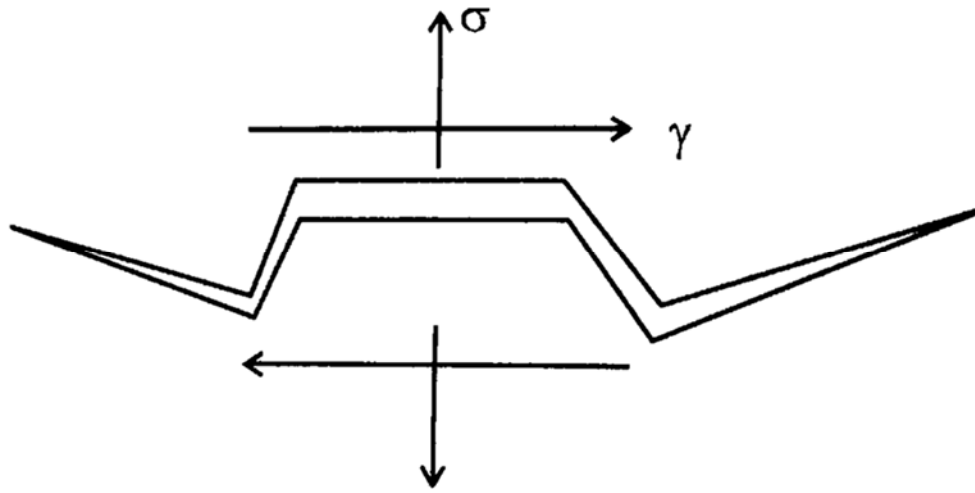


Figure 3-18: Physical basis of Fatemi-Socie model [20].

The material behavior is dependent on the loading magnitude as it may cause a change in the material state from linear elastic to non-linear plastic behavior. However, for small deformation cases like fatigue testing, the geometric behavior is independent of the magnitude of loading, as it does not cause any or very little change in the geometric state. Though, the geometrical behavior is dependent on the loading type (i.e. pure bending, pure torsion or mixed loading).

The critical plane for all pure bending loadings occur at the same angle. In other words, if the stress state is represented using Mohr's circle, then any changes in the magnitude of load will only change the size of the circle. The principle and the maximum shear stress/stain planes are constant. This suggests that the geometrical effects in fatigue damage for pure bending loadings is a constant. Thus, the geometric correction factors are constant for pure bending loadings. Similarly, the critical plane for all pure torsion loadings occur

at the same angle. Thus, it suggests that the geometric correction factors are also constant for pure torsion loadings.

For pure bending loadings, the proposed damage parameter takes the following form:

$$FP = \frac{\Delta\gamma}{2} \left(1 + k \frac{\sigma_{n,max}}{S_y} + g_{1,b} \right) + g_{2,b} \quad (3-18)$$

where $g_{1,b}$ and $g_{2,b}$ are bending notch geometric correction factors and are constant. These correction factors are determined by fitting the fatigue damage parameter in Eq. (3-18) with the experimental fatigue life data under pure bending loading.

Similarly, for pure torsion loadings, the proposed damage parameter takes the following form:

$$FP = \frac{\Delta\gamma}{2} \left(1 + k \frac{\sigma_{n,max}}{S_y} + g_{1,t} \right) + g_{2,t} \quad (3-19)$$

where $g_{1,t}$ and $g_{2,t}$ are torsion notch geometric correction factors and are constant. These correction factors are determined by fitting the fatigue damage parameter in Eq. (3-19) with the experimental fatigue life data under pure torsion loading.

The critical plane for all the multiaxial loadings (combined bending-torsion) does not occur at the same angle. For multiaxial loadings, the critical plane is a function of the amplitude of axial and shear stresses as shown by Eqs. (2-60) and (2-61). Therefore, for

the in-phase and 90° out-of-phase loadings, the notch geometric correction factors are also not constant and are functions of the amplitude of bending and torsion loadings. The notch geometric correction factors for general multiaxial loading, including in-phase and 90° out-of-phase loadings, are calculated using a weight function:

$$g_i = \left(\frac{\sigma_{nom}^2}{\sigma_{nom}^2 + \tau_{nom}^2} \right) g_{i,b} + \left(\frac{\tau_{nom}^2}{\sigma_{nom}^2 + \tau_{nom}^2} \right) g_{i,t} \quad (3-20)$$

where σ_{nom} and τ_{nom} are the nominal axial and shear stresses, respectively, and $i = 1, 2$.

Initially, square of the von-Mises stress equation, which is $\sigma^2 + 3\tau^2$, was used as a weight function to avoid any imaginary number values for the notch geometric correction factors. However, because of the term $3\tau^2$, the weight function does not collapse to the torsion notch geometric correction factors for pure torsion loading. Therefore, to avoid this problem, the weight function was used in the form of $\sigma^2 + \tau^2$.

The proposed fatigue damage model can be written in terms of the damage parameter and life equation as:

$$\frac{\Delta\gamma_{max}}{2} \left(1 + k \frac{\sigma_{n,max}}{\sigma_{yt}} + g_1 \right) + g_2 = \frac{\tau_f'}{G} (2N_f)^{b_s} + \gamma_f' (2N_f)^{c_s} \quad (3-21)$$

3.7 Computational Fatigue Design Tool

An in-house computational fatigue design tool is developed for the multiaxial fatigue analysis of the notched components. Given any notched component geometric model, material properties, loading type, loading amplitude and appropriate boundary conditions; it can be used to automatically perform the FE analysis and multiaxial fatigue analysis. The FE analysis is performed to determine the stress-strain histories at the critical locations in the notched component. The multiaxial fatigue analysis utilizes these stress-strain histories to determine the fatigue damage which is further used for fatigue life estimation. The FE analysis is done using APDL code and the multiaxial fatigue analysis is done using MATLAB code.

MATLAB and APDL codes are automated and linked together for the computational fatigue design tool. The MATLAB code automatically calls APDL code to perform every simulation. The APDL code then runs the simulation for the given geometry, material properties, loading type (pure bending, pure shear, proportional and non-proportional combined bending-torsion) and loading magnitude. It performs the cyclic elastic-plastic stress analysis using multilinear kinematic hardening, to determine cyclic stress-strain history at the critical nodes. It then saves these stress-strain histories in a CSV file at the end of every simulation. The MATLAB code reads the CSV file and uses these stress-strain histories as an input, applies a fatigue damage model on it, and returns the multiaxial fatigue life.

CHAPTER 4

RESULTS AND DISCUSSION

4.1 Validation of FE Model

During experimental testing of the SAE notched shaft specimens, strain gages were placed at the 5mm notch root because it was the critical location. These strain gage data, which have been compiled by Kurath et al. [10], are used to validate the present FE model. The strain gage data is compared with the numerical strain data on a node located at the notch root. Table 4-1 shows the comparison of both strain data.

Table 4-1: Validation of FE model using measured strain gage data.

Specimen	Loading	Numerical Strains (microstrain)		Half Life Strains [10] (microstrain)		Percent Error	
		$\Delta\varepsilon_{xx}/2$	$\Delta\varepsilon_{xz}/2$	$\Delta\varepsilon_{xx}/2$	$\Delta\varepsilon_{xz}/2$	$\Delta\varepsilon_{xx}/2$	$\Delta\varepsilon_{xz}/2$
JD-BR3-1	Bending	4371	20	4373	0	0.05	-
AOS-BR3-1		3845	17	3900	-	1.41	-
JD-BR3-2		3845	17	2750	0	39.82	-
AOS-BR3-2		3810	17	3800	-	0.27	-
JD-BR2-1		2326	8	2240	0	3.84	-
BC-BR2-1		2326	8	2420	0	3.88	-
RN-BR2-1		2080	7	2730	0	23.82	-
AOS-BR2-1		2080	7	2150	0	3.27	-
AOS-BR2-2		2045	7	2175	0	5.98	-

AOS-BR1-1		1698	5	1830	0	7.22	-	
AOS-BR1-2		1676	5	1775	0	5.60	-	
JD-BR1-1		1698	5	1720	0	1.29	-	
JD-TR3-1	Torsion	2	7931	0	13000	-	38.99	
BC-TR2-1		1	4604	0	2650	-	73.72	
RN-TR1-1		0	3226	0	2710	-	19.04	
JD-TR0-1		0	2483	-	2925	-	15.10	
JD-TR0-2		0	2068	0	2390	-	13.46	
JD-XR3-1	In-phase	3389	4558	2759	4933	22.84	7.60	
RN-XR2-1		1606	2752	1020	2670	57.42	3.07	
JD-XR2-1		1610	2777	1270	2480	26.75	11.98	
RN-XR1-1		1186	2007	1250	1570	5.13	27.84	
IL-YR3-1		2299	2200	2200	2000	4.52	9.99	
IL-YR3-2		2299	2200	1900	1740	21.03	26.42	
BC-YR2-1		2107	1444	2400	1725	12.21	16.28	
JD-YR1-1		2092	1343	1969	1525	6.26	11.95	
RN-YR1-1		1445	1208	1640	900	11.91	34.22	
IL-YRN-1		1342	1518	1160	1460	15.72	3.96	
IL-YRN-2		1342	1518	1530	1500	12.26	1.18	
IL-YRN-3		1019	1154	750	1440	35.90	19.89	
JD-ZR3-1		2307	6629	2253	8915	2.40	25.64	
IL-ZR3-1		1499	6312	1550	6620	3.30	4.65	
IL-ZR3-2		1478	6306	1460	6200	1.23	1.70	
IL-ZR2-4		802	3885	920	4400	12.79	11.70	
JD-ZR2-1		1084	2844	1010	3390	7.30	16.12	
IL-ZRN-1		568	2663	700	2750	18.86	3.15	
JD-ZR03-1		90° Out-of-phase	1380	6148	1045	6458	32.08	4.81
JD-XR03-1			2519	3835	2342	3618	7.55	6.00
JD-XR03-2	2419		3806	1800	3200	34.39	18.93	
BC-XR03-1	2248		4242	1800	4365	24.89	2.81	
JD-YR03-1	3231		1947	2778	1645	16.32	18.39	
JD-ZR03-2	805		3829	700	3409	14.99	12.33	
BC-XR03-1	1507		2584	1750	2950	13.90	12.42	
JD-XR02-1	1391		2576	1306	2440	6.53	5.57	
JD-XR02-2	1391		2576	1309	2443	6.28	5.44	
JD-XR01-1	1074		1921	990	1745	8.51	10.06	

Figure 4-1a shows the comparison of numerical and measured notch root strains for pure bending loading. The error bars show that there is a variation in the measured strain gage data. The marker shows the mean, whereas the bars show the minimum and maximum, of the measured strain data at a given bending loading. Some of the data points does not have error bars because their tests were not duplicated during the benchmark program. From Table 4-1 and Figure 4-1a, it can be seen that the FE model works really well for most of the pure bending loads. Also, it can be seen in Figure 4-1a that the FE model results for pure bending loading are comparable to the previous work by Ince [70] and Fash [51]. Experimentally, the shear strain under pure bending loadings should be zero, however, the FE model gives a very small value close to zero, which are also very small values compared to the corresponding axial strain values. As the experimental shear strains are zero, thus the percent error in shear strain estimation is a value divided by zero, thus the percent error in shear strain estimation for pure bending loading is not shown in Table 4-1.

Figure 4-1b shows the comparison of numerical and measured notch root strains for pure torsion loading. From Table 4-1 and Figure 4-1b, it can be seen that the FE model strains does not match well with the strain gage data. This is because of the error in the measured strain gage data, as shown in Table 4-2, as the first three data points follow the opposite trend i.e. the shear strain is increasing by decreasing the torsional moment. Also for all the four data points in the Table 4-2, there is a very little difference in shear strains while there is a huge difference in the torsional moment. The error in strain gage

measurement can also be evaluated from Figure 4-1b where there is a huge change in torsional moment while a very low change in measured shear strain hence it looks like a vertical trend which is not usually the case. Also, it can be seen in Figure 4-1b that the FE model results for pure torsional loading are comparable to the previous work by Ince [70] and Fash [51]. Experimentally, the axial strain under pure torsion loadings should be zero, however, the FE model gives a very small value close to zero, which are also very small values compared to the corresponding shear strain values. As the experimental axial strains are zero, thus the percent error in axial strain estimation is a value divided by zero, thus the percent error in axial strain estimation for pure torsion loading is not shown in Table 4-1.

As the FE model works well for the pure bending and torsion loads, therefore, it will work well for both the in-phase as well as 90° out-of-phase bending-torsion loadings. Table 4-1 shows that the FE model calculates notch strains close to the strain-gage data for most of the in-phase as well as 90° out-of-phase loadings. The discrepancy in some of the data points could be explained by the possible scatter in the strain gage data as was the case with both the pure bending and torsion loadings. As the tests were conducted by several individuals of the contributing laboratories and companies, therefore, human error could be one of the main reasons for this scatter in the strain gage data. The placement of the strain gage by the laboratory personnel could also be a factor as there is a high strain gradient in the notch region and a little misplacement could cause large error in the measured strain data. Apart from the high strain gradient, the surface curvature could also

cause errors in the measured strain data if the strain gage were placed a bit up the notch root [47].

As the differences between most of the strain data is very small, and as it matches the results in the literature, so it validates the FE model.

Table 4-2: Error in measured strain gage data.

Specimen	Mb	Mt	Strain Gage Values at Half Life (microstrain)	
			$\Delta\epsilon_{xx}/2$	$\Delta\epsilon_{xz}/2$
BC-TR2-1	0	2400	0	2650
RN-TR1-1	0	2000	0	2710
JD-TR0-1	0	1700	-	2925
JD-TR0-2	0	1500	0	2390

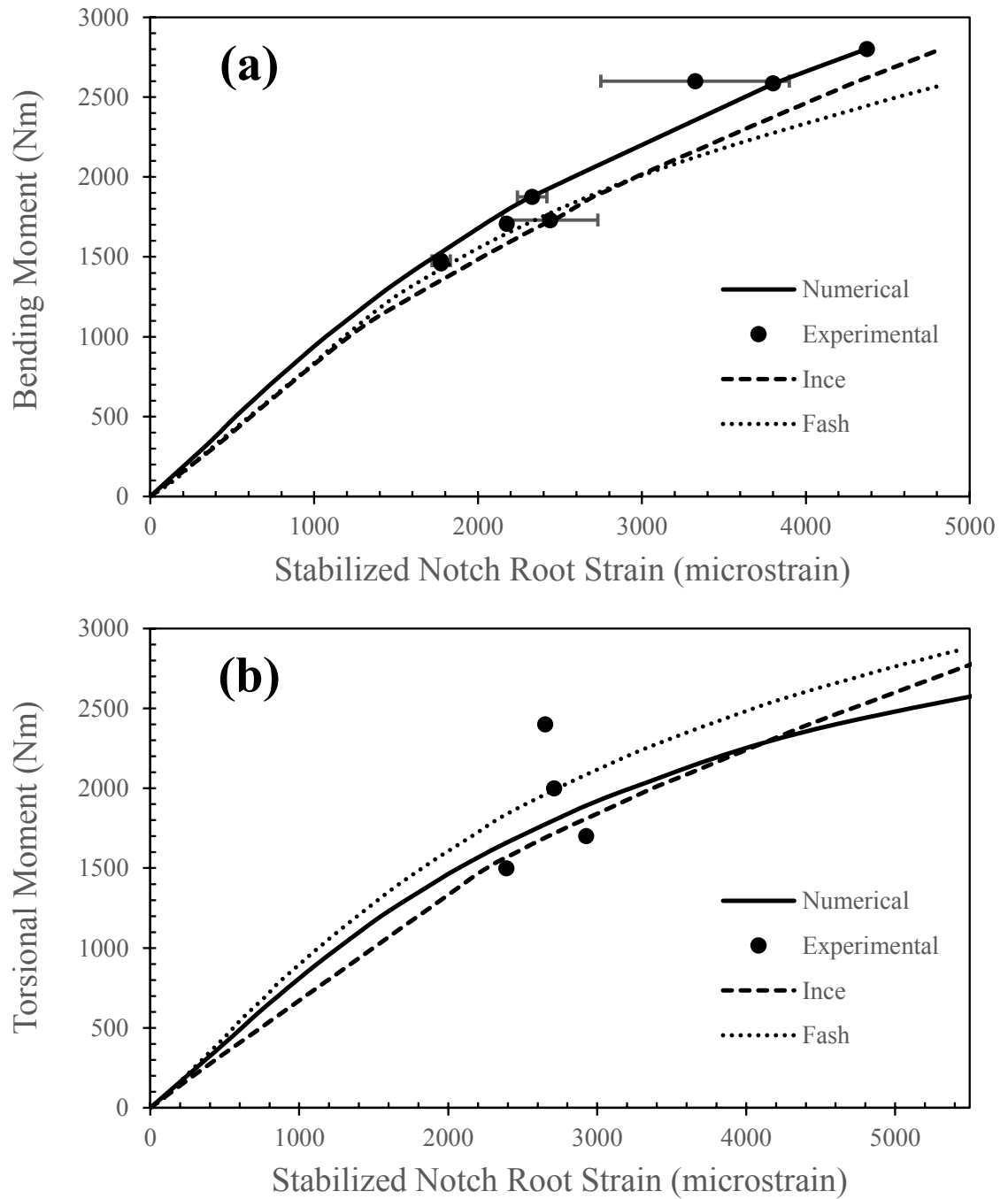


Figure 4-1: Comparison of numerical and measured notch root strains on the SAE 1045 notched shaft specimen; (a) For pure bending loading, (b) For pure torsion loading.

4.2 FEA Results

4.2.1 Stress and Strain Distributions

Bending Loading

The loading scenario of JD-BR3-1 is used for generating the nodal plots because it is subjected to the highest bending moment among other specimens under pure bending loading. Figure 4-2 shows the distribution of displacement vector sum under pure bending loading, which indicates that the bending loading has been applied correctly. Figure 4-3 shows the stress distribution in x-direction, and Figure 4-4 shows the strain distribution in x-direction under pure bending loading.

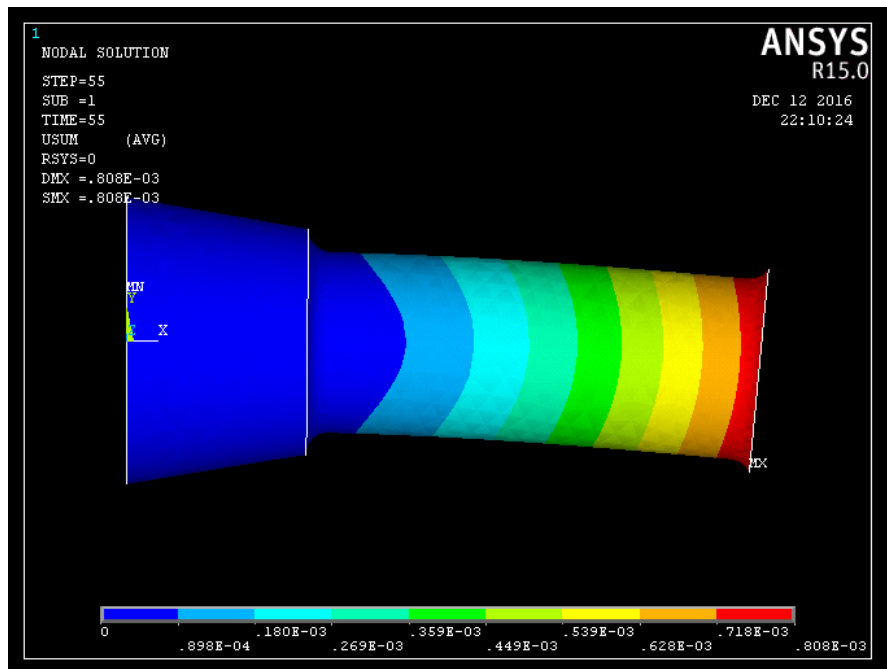


Figure 4-2: Displacement vector sum under pure bending loading at 1/4th cycle.

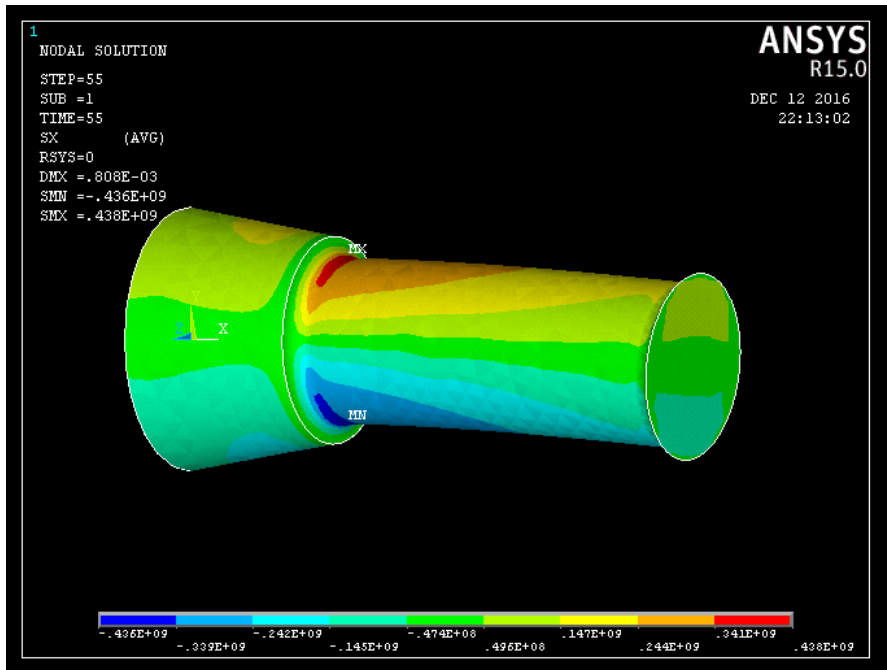


Figure 4-3: Stress distribution in x-direction under pure bending loading at 1/4th cycle.

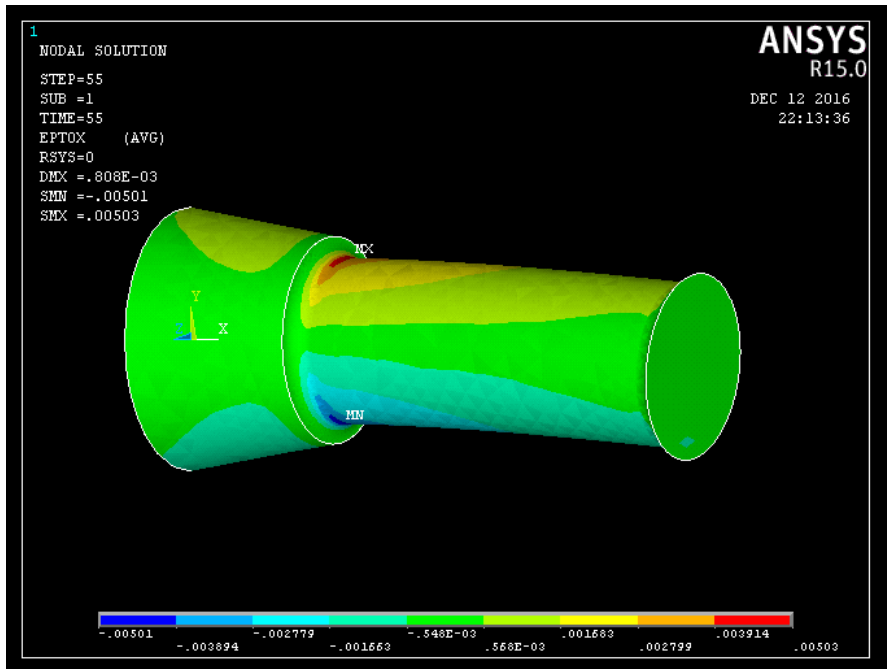


Figure 4-4: Total mechanical strain distribution in x-direction under pure bending loading at 1/4th cycle.

Torsion Loading

The loading scenario of JD-TR3-1 and IL-TR3-1 is used for generating the nodal plots because it is subjected to the highest torsional moment among other specimens under pure torsion loading. Figure 4-5 shows the distribution of displacement vector sum under pure torsion loading, which indicates that the torsion loading has been applied correctly. Figure 4-6 shows the shear stress distribution, and Figure 4-7 shows the shear strain distribution under pure torsion loading.

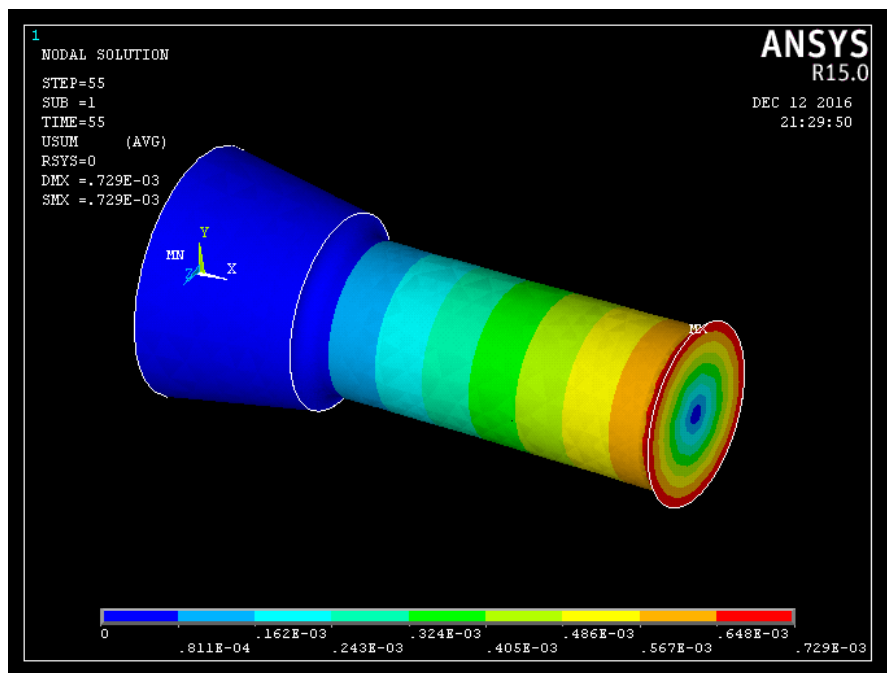


Figure 4-5: Displacement vector sum in pure torsion loading at 1/4th cycle.

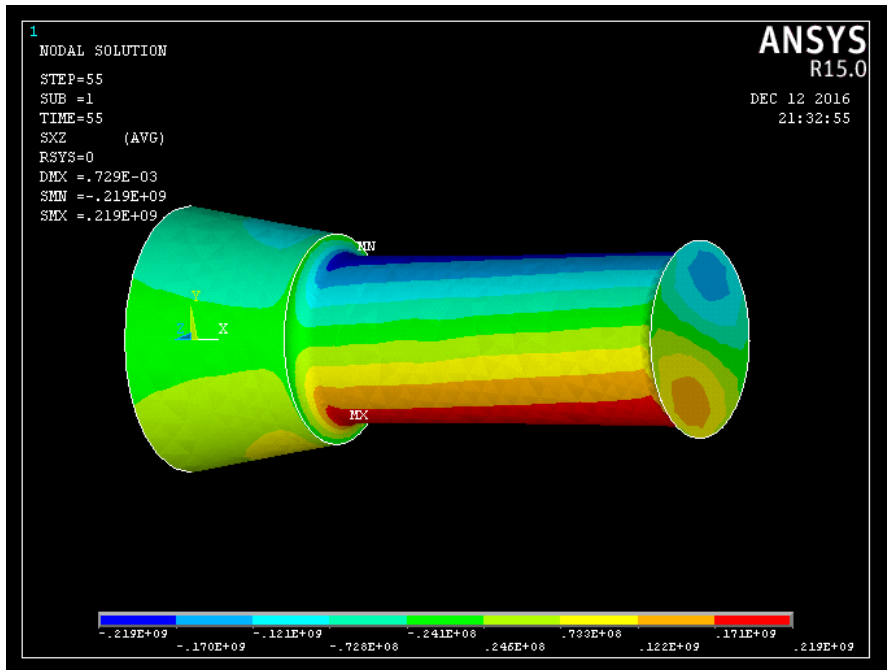


Figure 4-6: Shear stress distribution in pure torsion loading at 1/4th cycle.

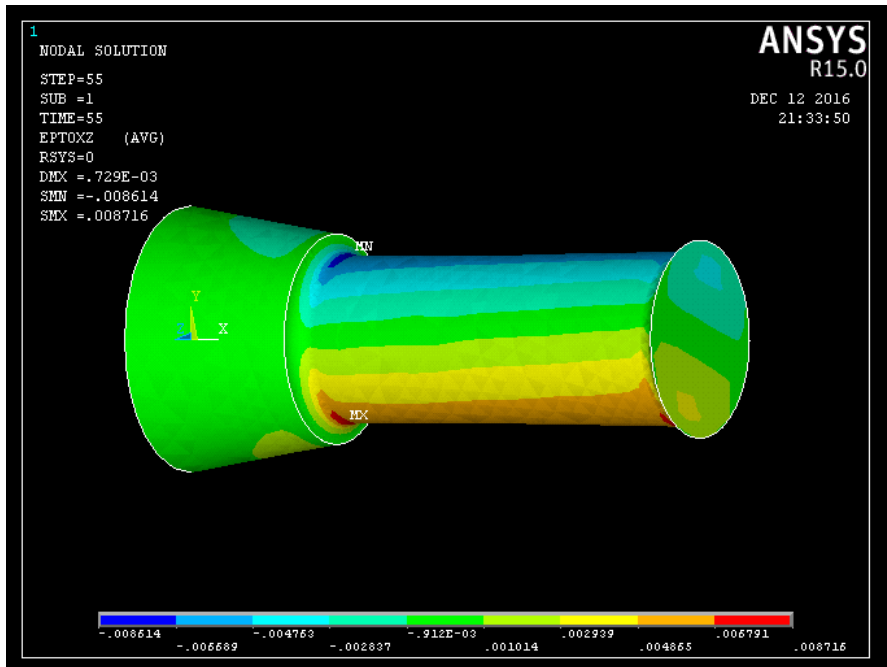


Figure 4-7: Shear strain distribution in pure torsion loading at 1/4th cycle.

In-Phase Bending-Torsion Loading

The loading scenario of JD-XR3-1 specimen is considered because it has both high bending and torsional moments. Figure 4-8 shows the von-Mises stress distribution, and Figure 4-9 shows the von-Mises total mechanical strain distribution under in-phase bending-torsion loadings.

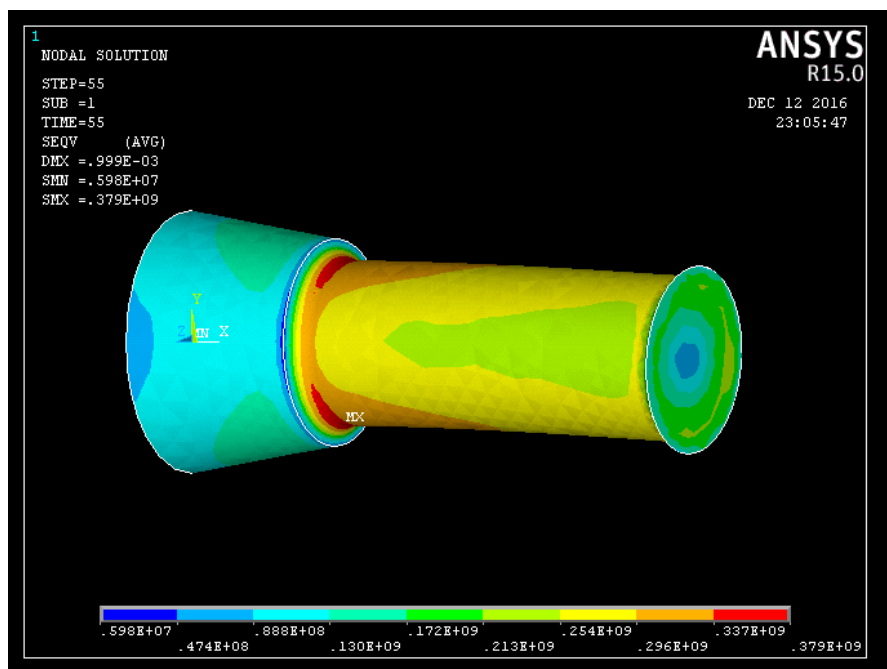


Figure 4-8: von-Mises stress distribution under in-phase bending-torsion loading at 1/4th cycle.

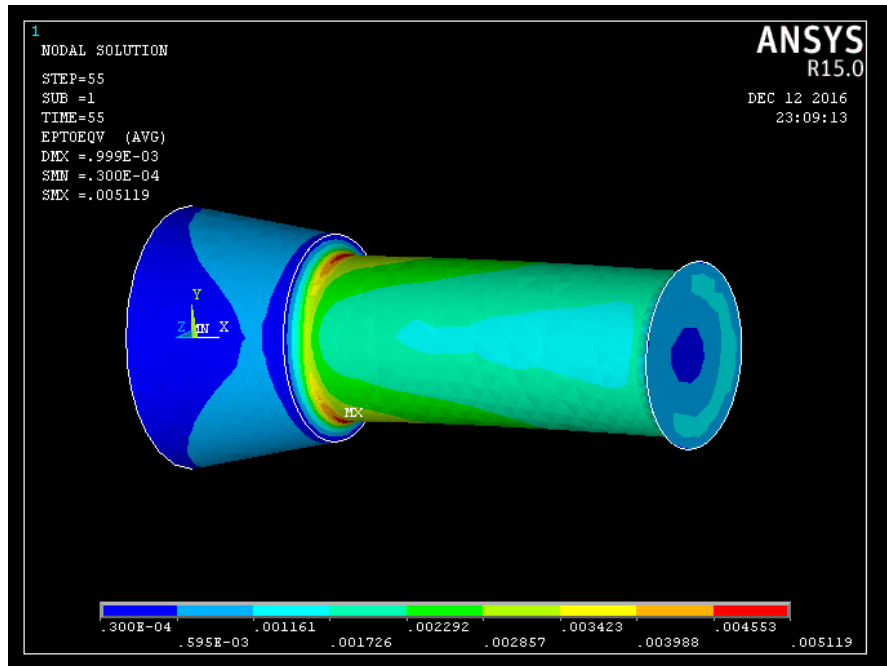


Figure 4-9: von-Mises strain distribution under in-phase bending-torsion loading at 1/4th cycle.

90° Out-of-Phase Bending-Torsion Loading

The loading scenario of JD-XR03-1 specimen is considered because it has both high bending and torsional moments. Figure 4-10 shows the von-Mises stress distribution, and Figure 4-11 shows the von-Mises total mechanical strain distribution under 90° out-of-phase bending-torsion loadings at 1/8th cycle.

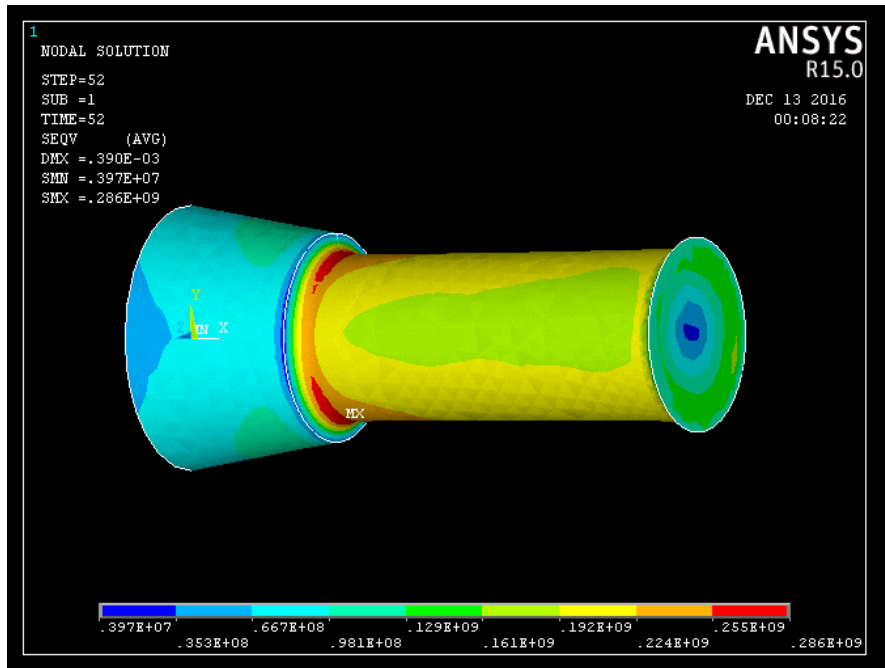


Figure 4-10: von-Mises stress distribution under 90° out-of-phase bending-torsion loading at 1/8th cycle.

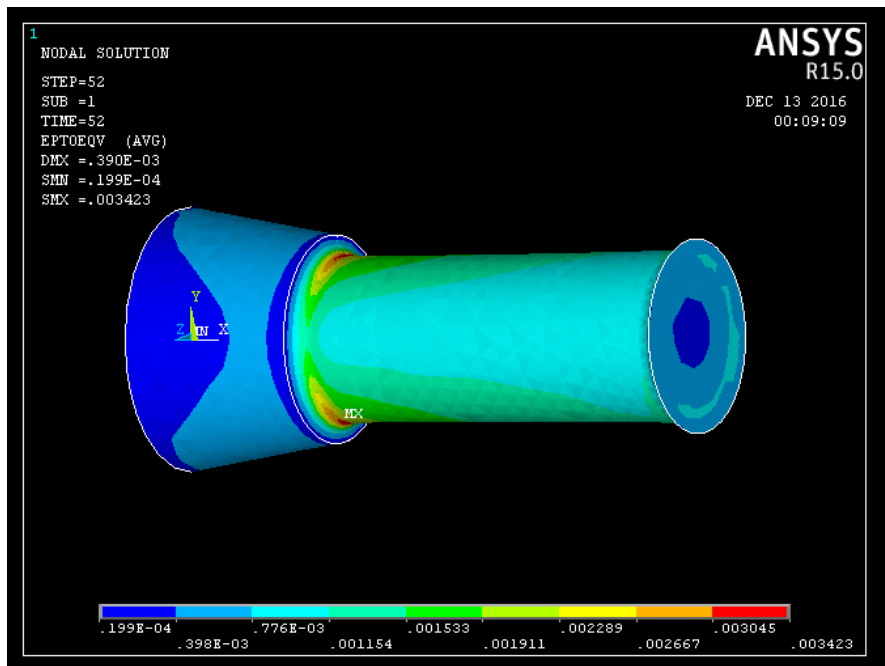


Figure 4-11: von-Mises strain distribution under 90° out-of-phase bending-torsion loading at 1/8th cycle.

4.2.2 Stress-Strain Histories

Stress-strain histories at two critical nodes, notch root node and maximum von-Mises node, were exported from ANSYS into MATLAB for multiaxial fatigue analysis.

Notch Root

Figure 4-12 to Figure 4-15 show the pure bending, pure torsion, multiaxial in-phase and 90° out-of-phase stress-strain histories at the notch root. These stress-strain histories are used for damage analysis and fatigue life estimation at the notch root. The limits of both the x- and y-axes have been kept same in all of the subplots for a general comparison of the magnitude of stresses and strains in specific directions. Figure 4-12 shows that only the axial stresses along x- and z-axes are acting at the notch root under pure bending loading, while Figure 4-13 shows that only the shear stress along xz-plane is acting at the notch root under pure torsion loadings. Figure 4-14 and Figure 4-15 show that only the axial stresses along x- and z-axes and shear stress along xz-plane are acting at the notch root under in-phase and 90°-out-of-phase loadings, respectively. This suggests that the notch root has a plane stress condition.

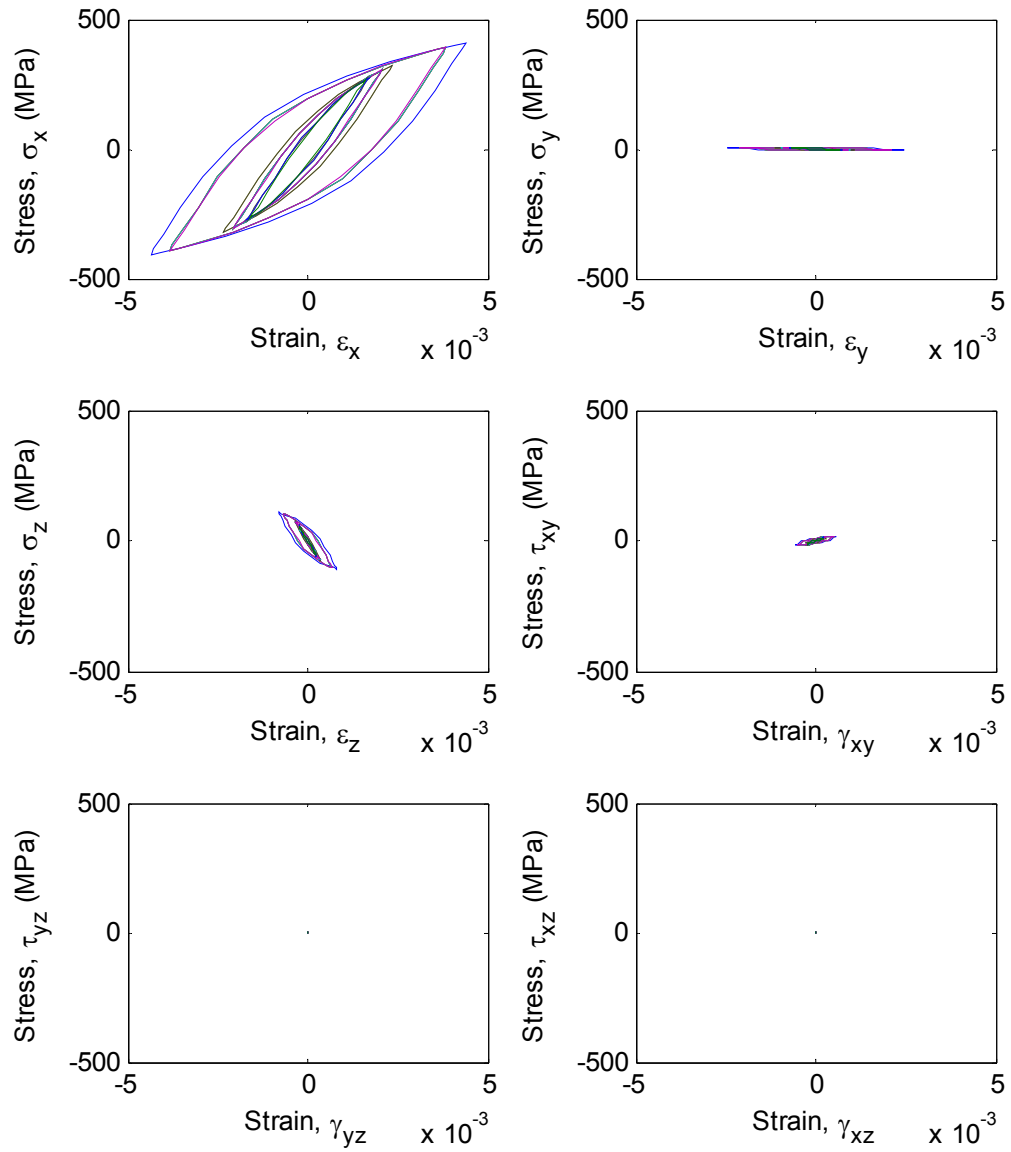


Figure 4-12: Notch root stress-strain history under pure bending loadings.

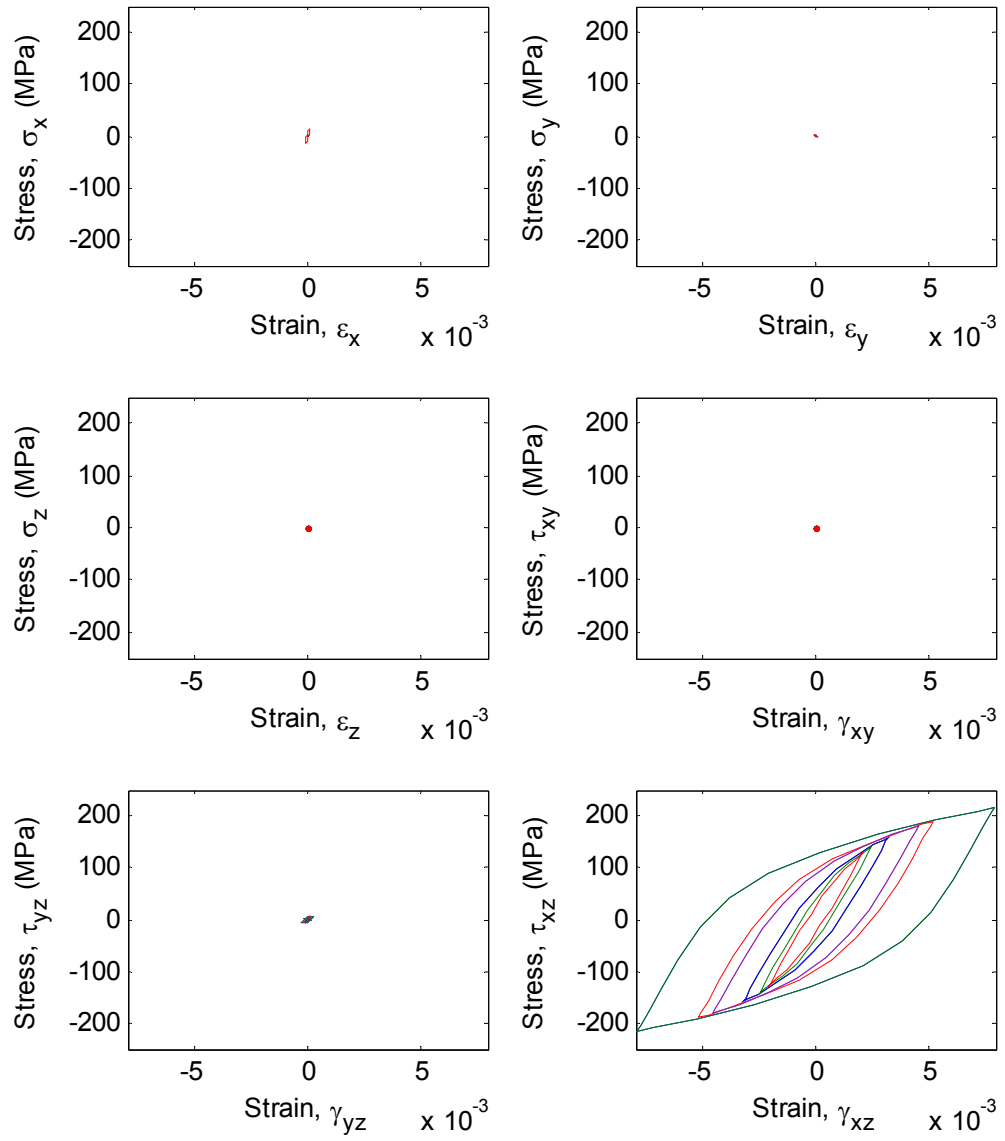


Figure 4-13: Notch root stress-strain history under pure torsion loadings.

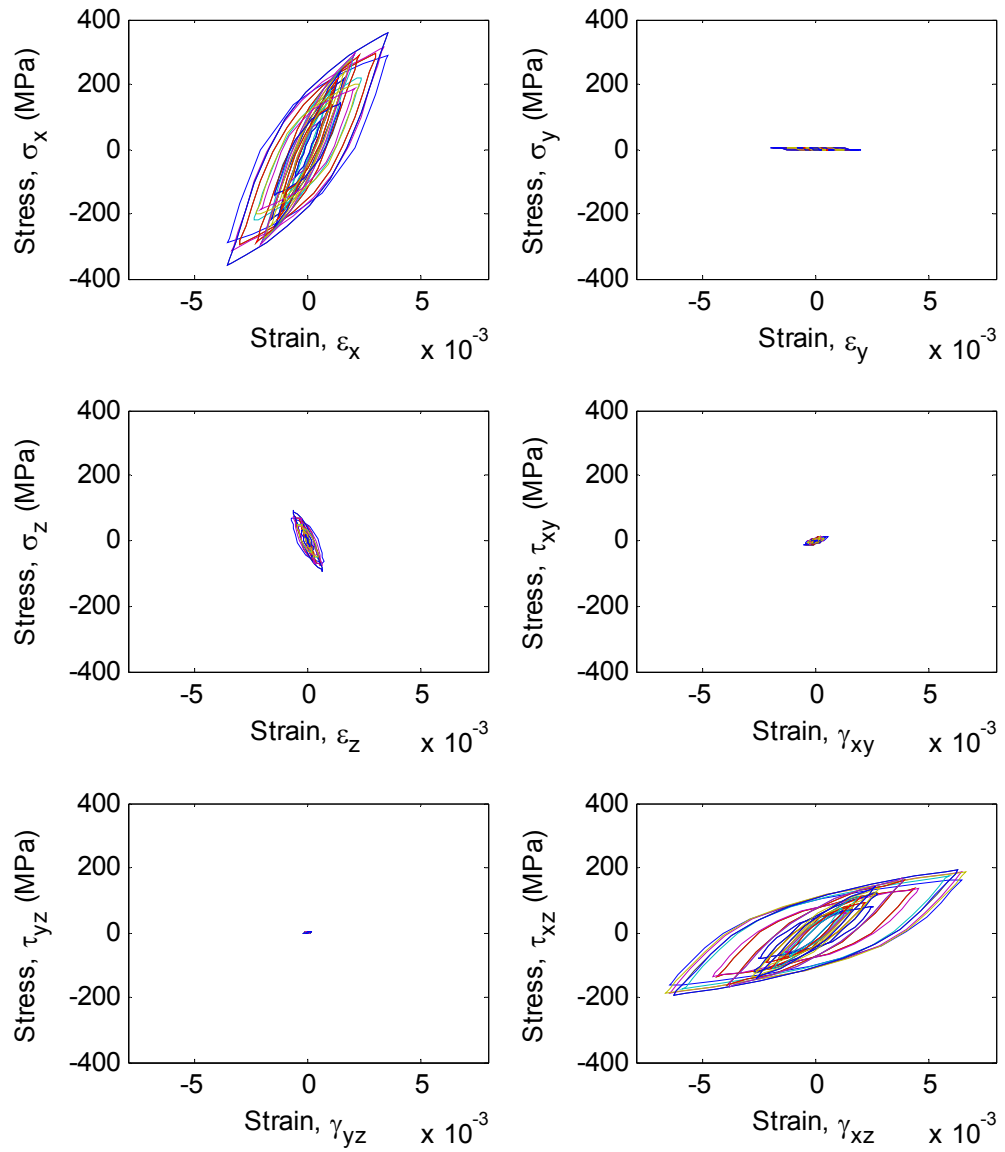


Figure 4-14: Notch root stress-strain history under in-phase multiaxial loadings.

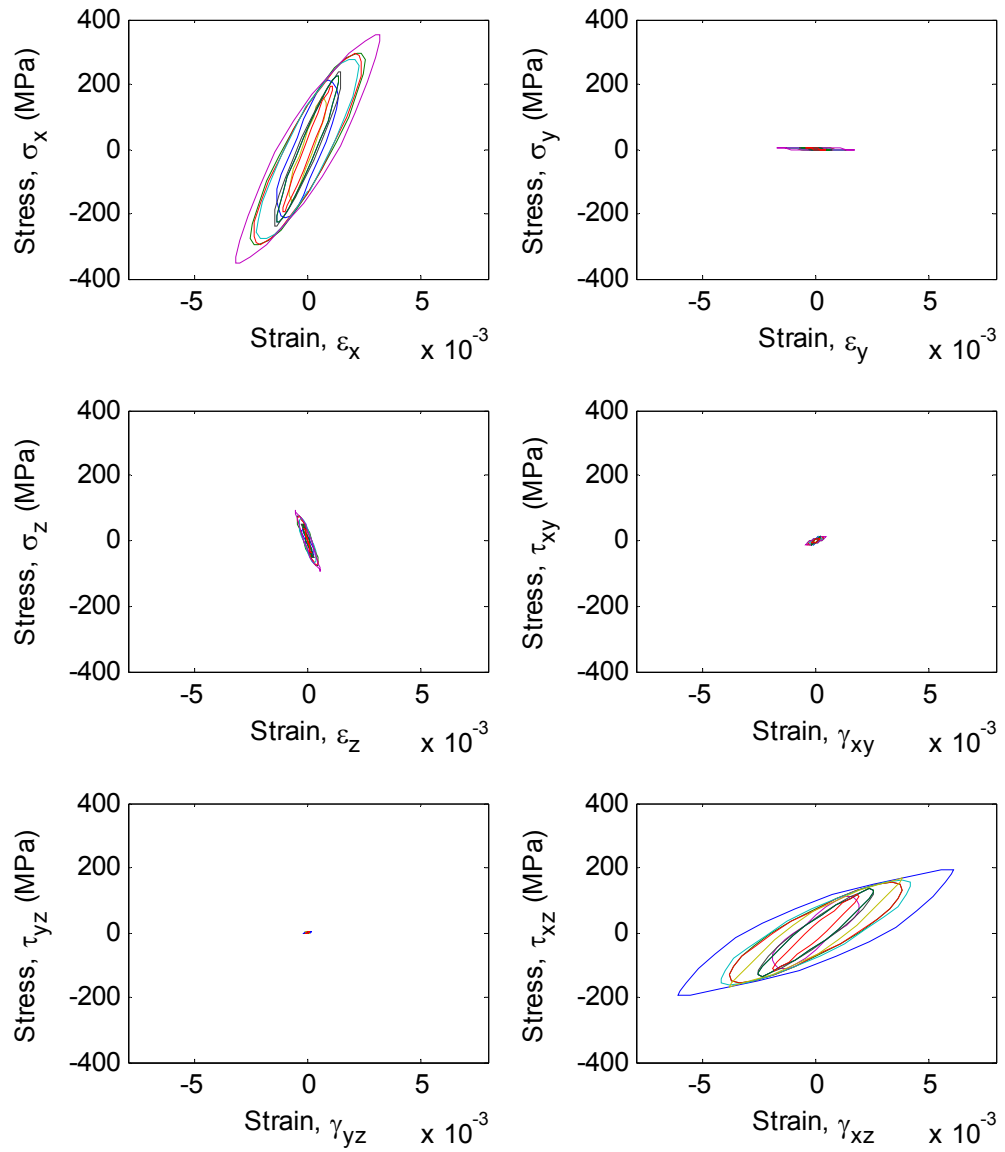


Figure 4-15: Notch root stress-strain history under 90° out-of-phase multiaxial loadings.

Maximum Von-Mises Location

Figure 4-16 to Figure 4-19 show the pure bending, pure torsion, multiaxial in-phase and 90° out-of-phase stress-strain histories at the maximum von-Mises node in the vicinity of notch. These stress-strain histories are used for damage analysis and fatigue life estimation at the maximum von-Mises location. The limits of both the x- and y-axes have been kept same in all of the subplots for a general comparison of the magnitude of stresses and strains in specific directions.

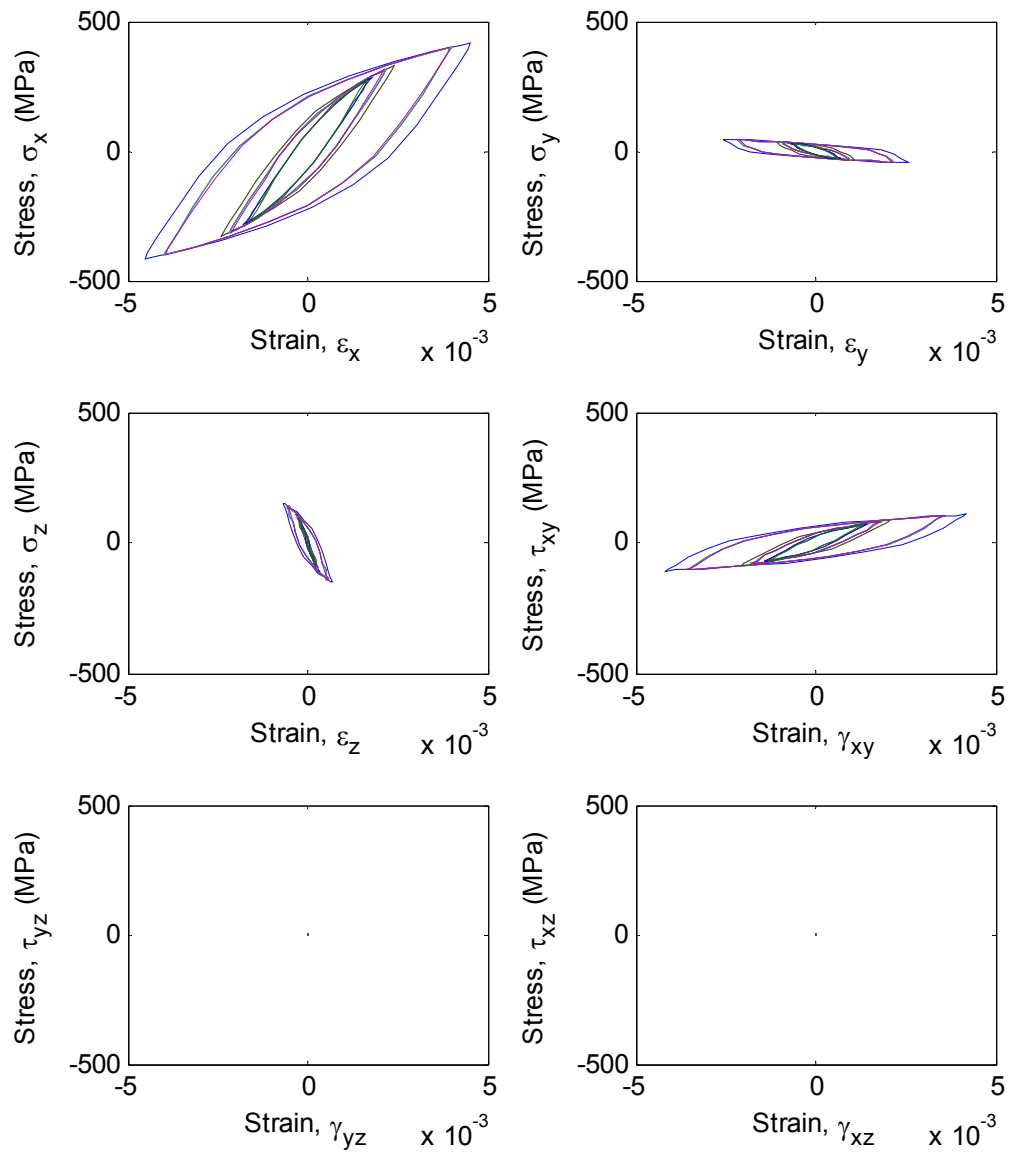


Figure 4-16: Stress-strain history at max von-Mises stress location under pure bending loadings.

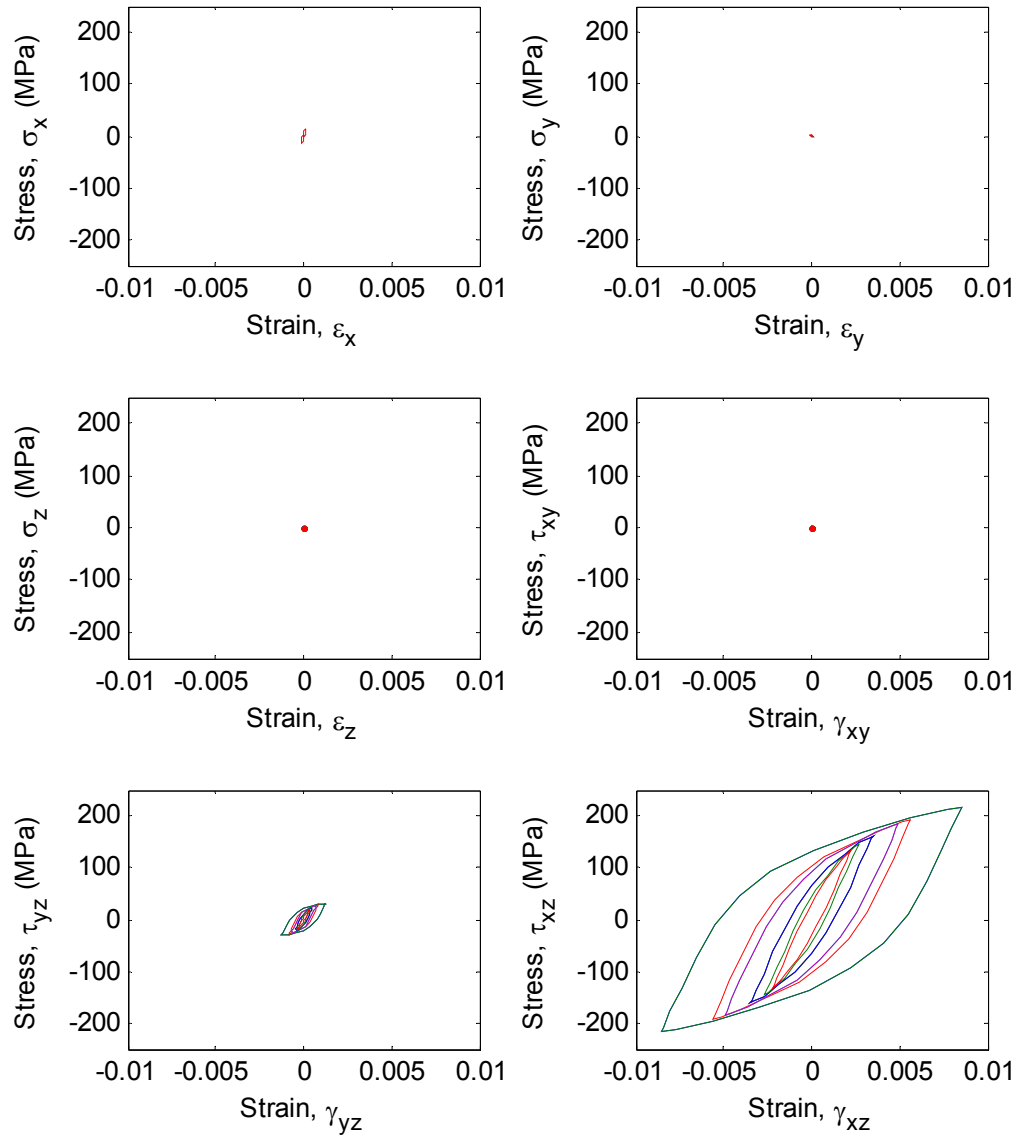


Figure 4-17: Stress-strain history at max von-Mises stress location under pure torsion loadings.

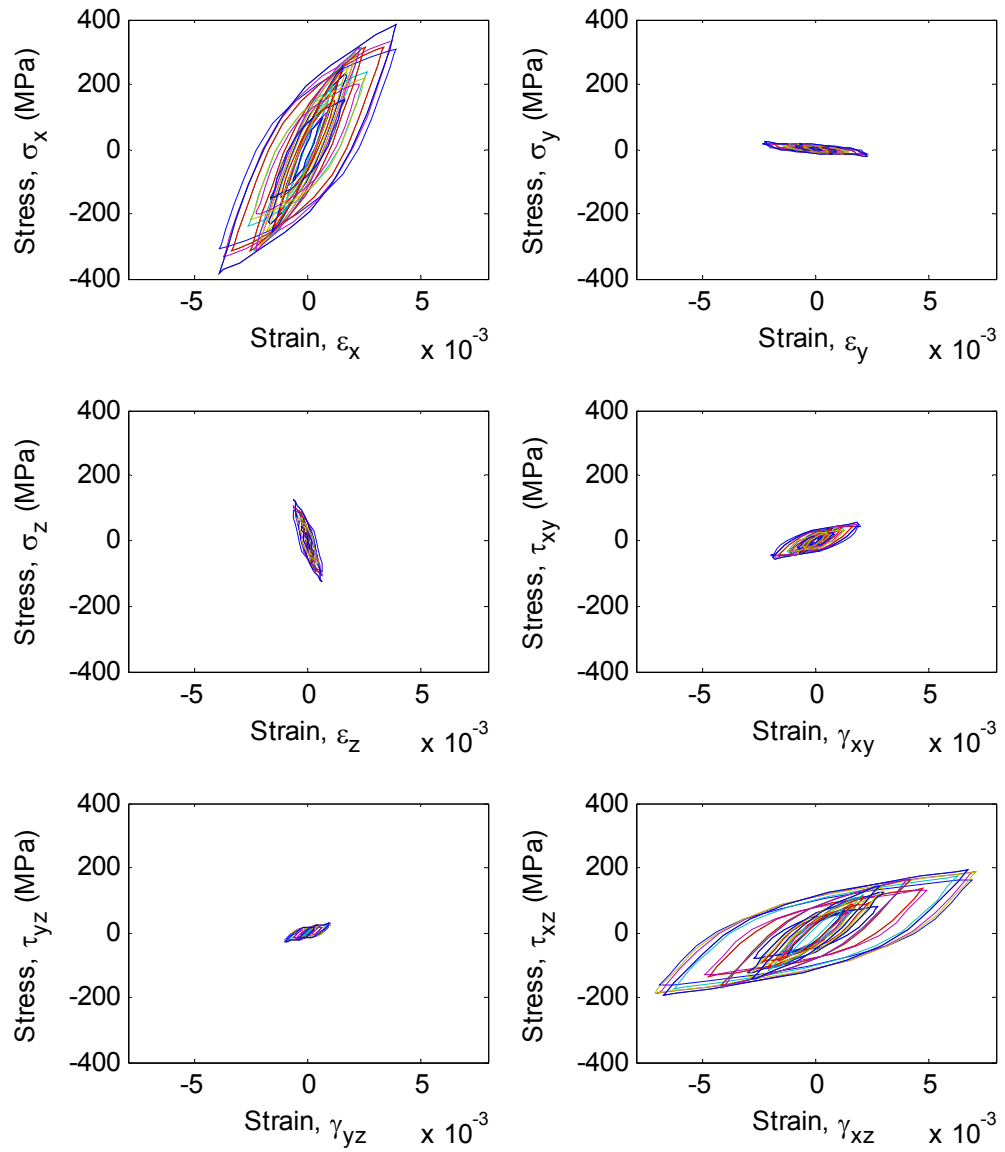


Figure 4-18: Stress-strain history at max von-Mises stress location under in-phase multiaxial loadings.

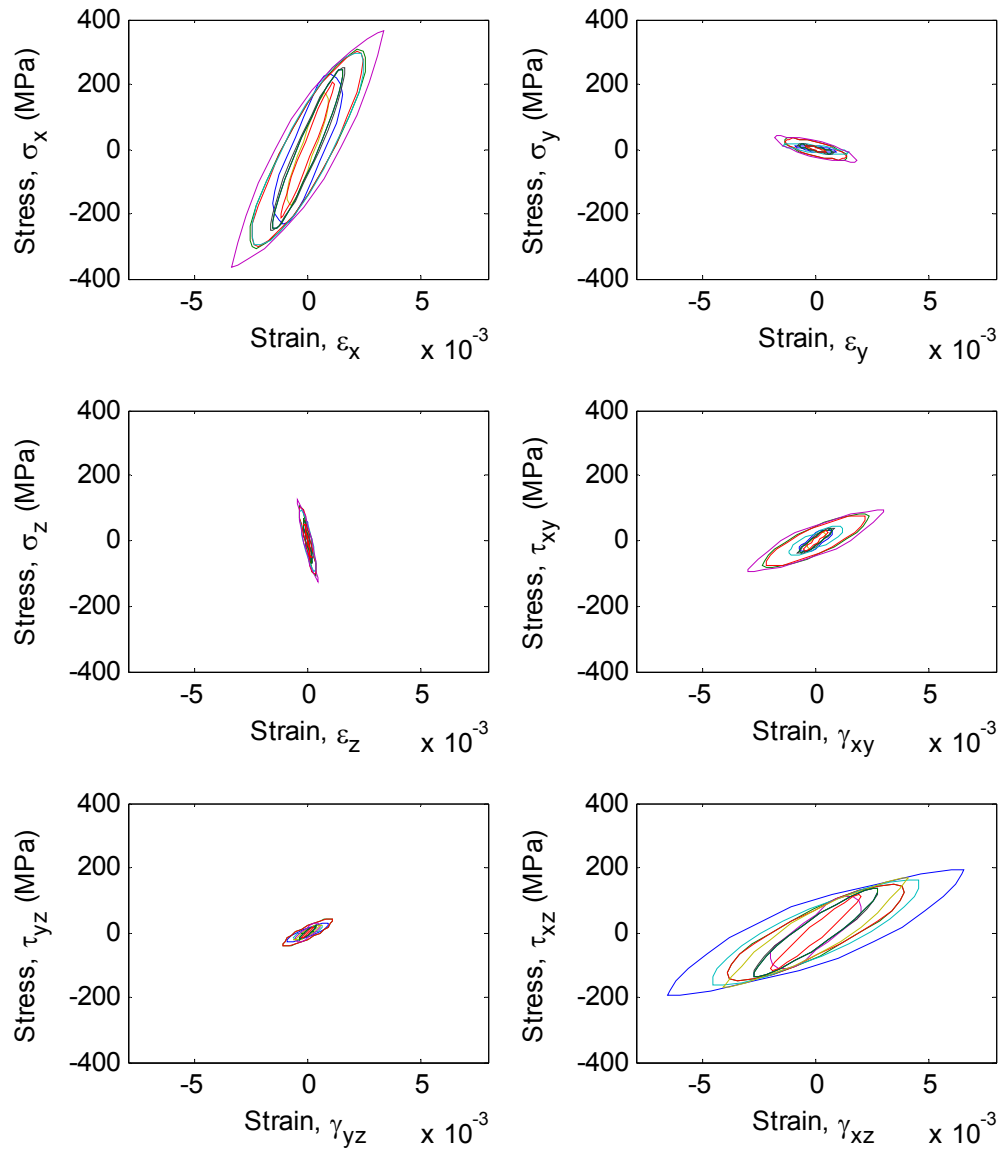


Figure 4-19: Stress-strain history at max von-Mises stress location under 90° out-of-phase multiaxial loadings.

4.3 Selection of Fatigue Damage Model

4.3.1 Comparison of Fatigue Damage Models

Figure 4-20 to Figure 4-22 show the fatigue life estimation of all the considered alloys using Fatemi-Socie, Smith-Watson-Topper and Jahed-Varvani models, respectively. By comparison, it can be seen that Fatemi-Socie model best correlates the fatigue life data for Albinmousa et al. [3,72] AZ31B alloy for all the loading paths. Both the Fatemi-Socie and Smith-Watson-Topper models did well in correlating fatigue life data for Zhang et al. [73] AZ61A alloy for all the loading paths. For Xiong et al. [2] AZ31B alloy, both the Jahed-Varvani and Fatemi-Socie models correlated the fatigue life data reasonably well. The Jahed-Varvani model gives more accurate estimations for low lives but estimates more on the non-conservative side for higher fatigue lives. This is because at higher fatigue lives the contribution of elastic energy in energy parameter is more compared to plastic energy, which is not as good an estimation parameter as that of plastic energy. For Hoffmeyer [74] S460N alloy, the Fatemi-Socie model better correlates the fatigue life data for all the loading paths.

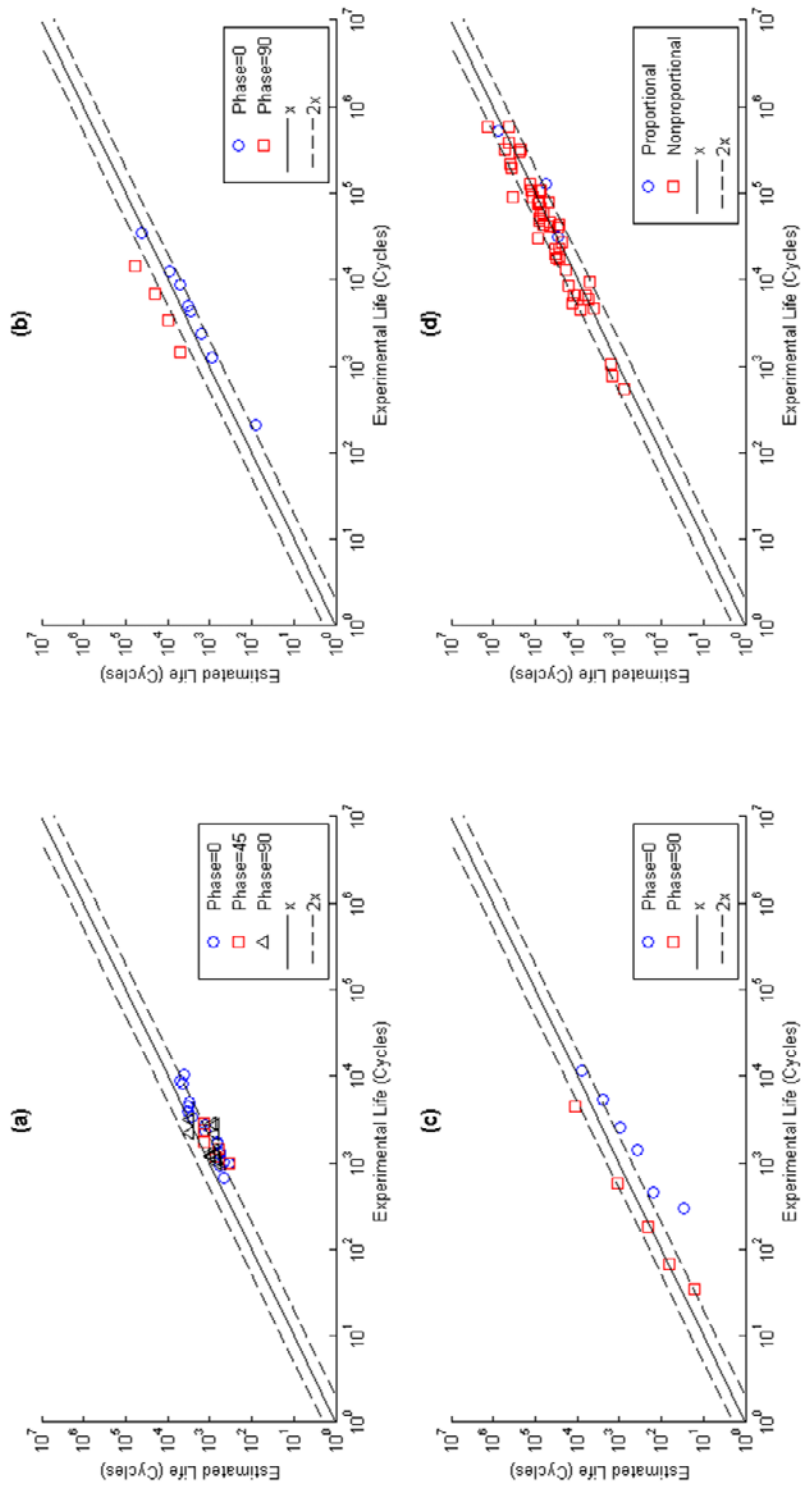


Figure 4-20: Fatigue life estimations using Fatemi-Socie model; using (a) Albinmoussa et al. [3,72] AZ31B Mg alloy data, (b) Zhang et al. [73] AZ61A Mg alloy data, (c) Xiong et al. [2] AZ31B Mg alloy data, and (d) Hoffmeyer [74] S460N structural steel alloy data.

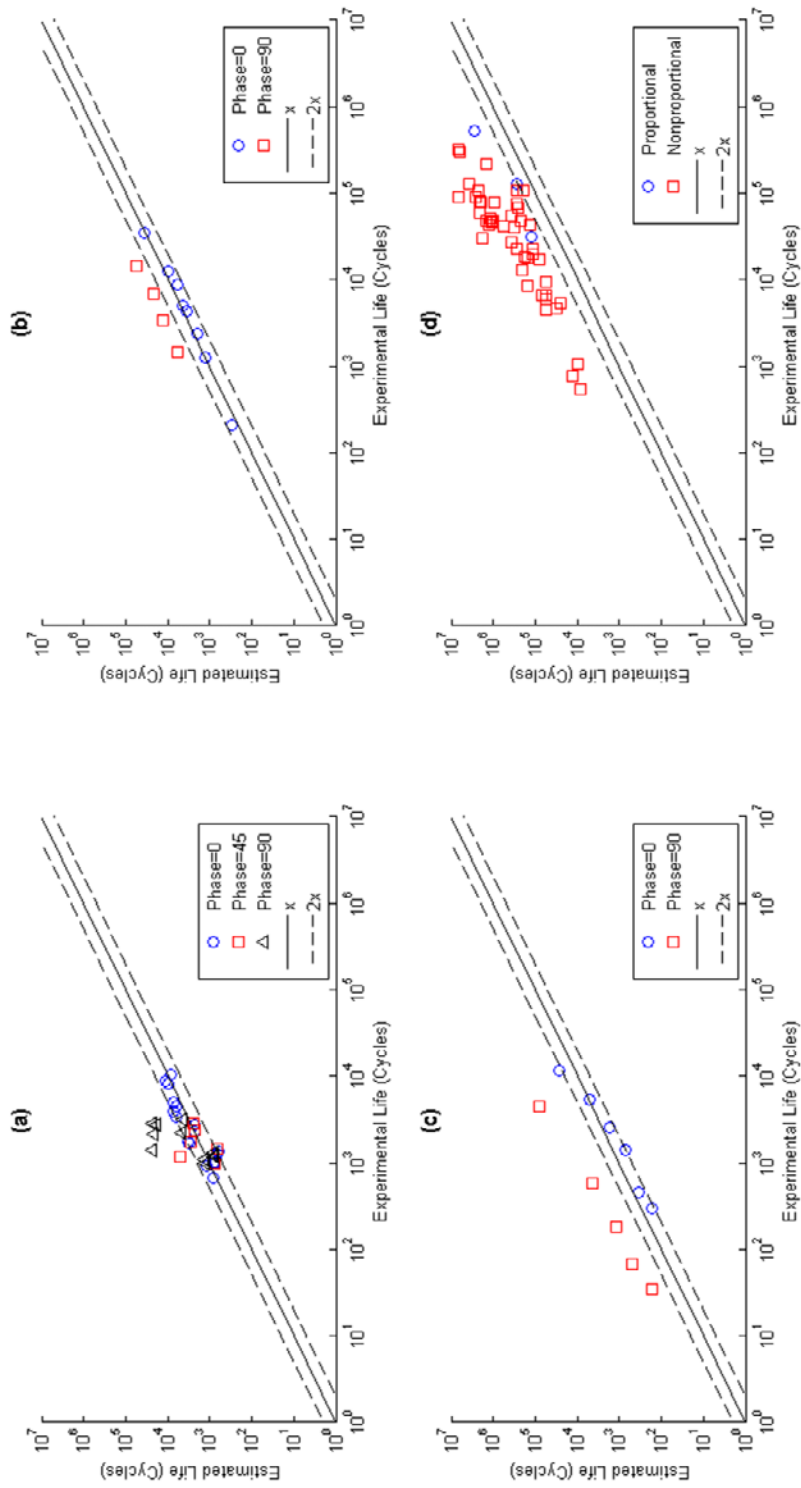


Figure 4-21: Fatigue life estimations using Smith-Watson-Topper model; using (a) Albinmousa et al. [3,72] AZ31B Mg alloy data, (b) Zhang et al. [73] AZ61A Mg alloy data, (c) Xiong et al. [2] AZ31B Mg alloy data, and (d) Hoffmeyer [74] S460N structural steel alloy data.

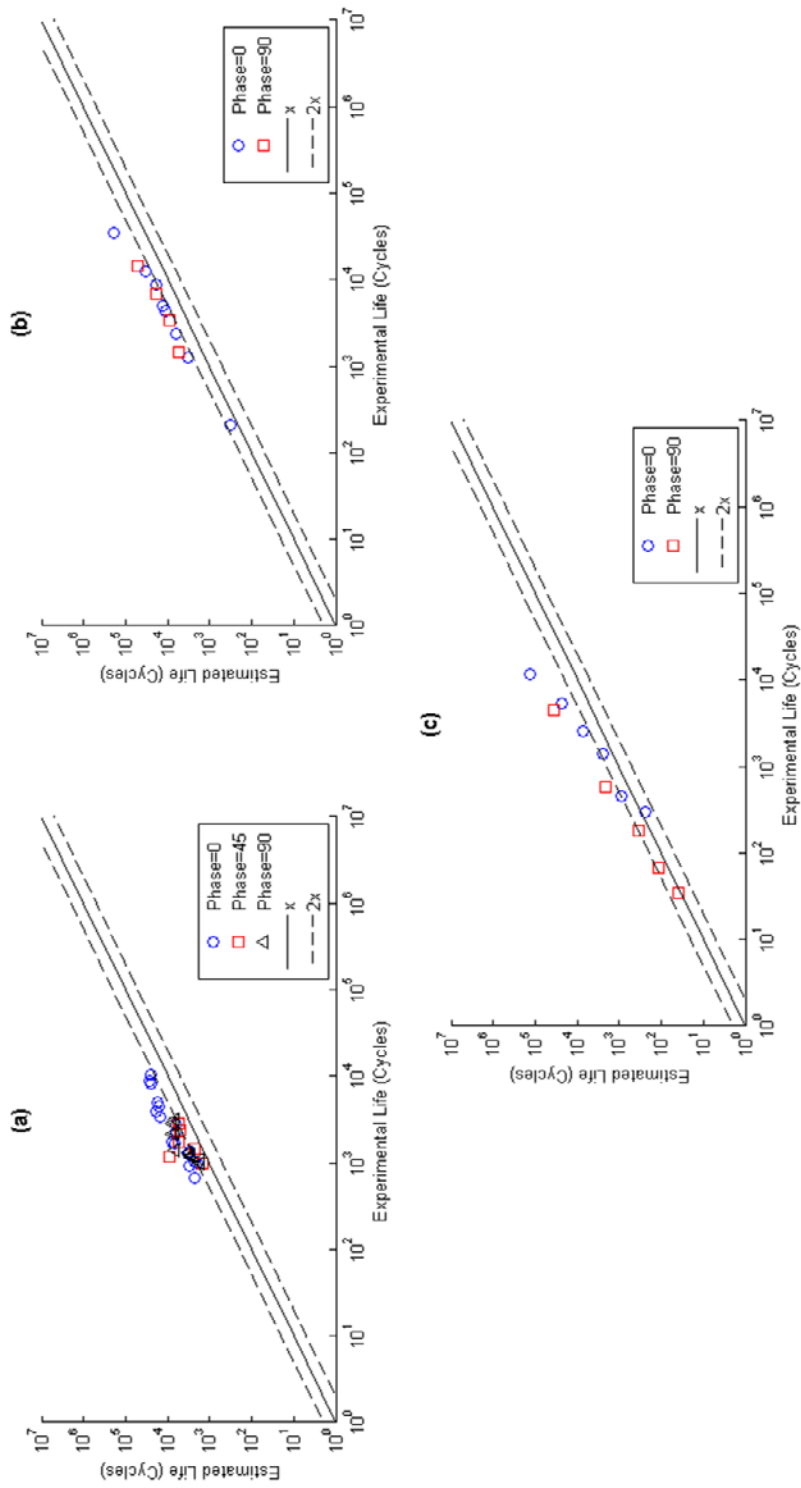


Figure 4-22: Fatigue life estimations using Jahed-Varvani model; using (a) Albinmousa et al. [3,72] AZ31B Mg alloy data, (b) Zhang et al. [73] AZ61A Mg alloy data, and (c) Xiong et al. [2] AZ31B Mg alloy data.

4.3.2 Proposed Assessment Method Results

Fatemi-Socie Model

Figure 4-23 shows the results of the proposed assessment method for Fatemi-Socie model using all the considered alloys. For Albinmousa et al. [3,72] AZ31B alloy, as shown in Figure 4-23a, the Fatemi-Socie model did really well in estimating very close to the observed fatigue lives at a certain plane for all the three phase angles (0° , 45° and 90°). For Zhang et al. [73] AZ61A alloy, as shown in Figure 4-23b, the Fatemi-Socie model did really well in estimating very close to the observed lives for in-phase data but failed to do so for 90° out-of-phase data. For Xiong et al. [2] AZ31B alloy, as shown in Figure 4-23c, the Fatemi-Socie model did really well in estimating very close to the observed lives for both in-phase as well as for 90° out-of-phase data, except for some of the 90° out-of-phase data. For Hoffmeyer [74] S460N alloy, as shown in Figure 4-23d, the Fatemi-Socie model did really well in estimating very close to the observed lives for all the proportional and most of the nonproportional data.

Smith-Watson-Topper Model

Figure 4-24 shows the results of the proposed assessment method for Smith-Watson-Topper model using all the considered alloys. For Albinmousa et al. [3,72] AZ31B alloy, as shown in Figure 4-24a, the Smith-Watson-Topper model did well in estimating close to the observed fatigue lives at a certain plane for most of in-phase and 45° out-of-phase data but did not do well for some of the 90° out-of-phase data. For Zhang et al. [73] AZ61A

alloy, as shown in Figure 4-24b, the Smith-Watson-Topper model also did really well in estimating close to the observed lives for in-phase data and failed to do so for 90° out-of-phase data. For Xiong et al. [2] AZ31B alloy, as shown in Figure 4-24c, the Smith-Watson-Topper model also did really well in estimating close to the observed lives for in-phase data but failed to do so for 90° out-of-phase data. For Hoffmeyer [74] S460N alloy, as shown in Figure 4-24d, the Smith-Watson-Topper model failed in estimating close to the observed lives for all the proportional and nonproportional data.

Jahed-Varvani Model

Figure 4-25 shows the results of the proposed assessment method for Jahed-Varvani model using all the considered alloys. For Albinmoussa et al. [3,72] AZ31B alloy, as shown in Figure 4-25a, the Jahed-Varvani model did well in estimating close to the observed fatigue lives at a certain plane for some of 45° and most of 90° out-of-phase data but did not do well for most of the in-phase data. For Zhang et al. [73] AZ61A alloy, as shown in Figure 4-25b, the Jahed-Varvani model did not do well in estimating life close to the observed lives for both in-phase and 90° out-of-phase data. For Xiong et al. [2] AZ31B alloy, as shown in Figure 4-25c, the Jahed-Varvani model did well in estimating close to the observed lives for half of the in-phase data and 90° out-of-phase data. However, it estimated the 90° out-of-phase data well than Smith-Watson-Topper Model.

From all the above comparison, it can be seen that the Fatemi-Socie model did really well in estimating lives close to the observed fatigue lives at a certain plane for AZ31B,

AZ61A and S460N alloys. Thus, the results of the proposed assessment method suggest that the Fatemi-Socie model, with further studies and improvements, has a more successful chance to successfully close the ± 2 factor gap for smooth specimens and ± 3 factor gap for notched components, respectively. As it is the best fatigue damage model for smooth specimens, it can be modified to take into account the geometric corrections needed to adjust the notch effects, and thus has a more successful chance to successfully close the ± 3 factor gap for notched components.

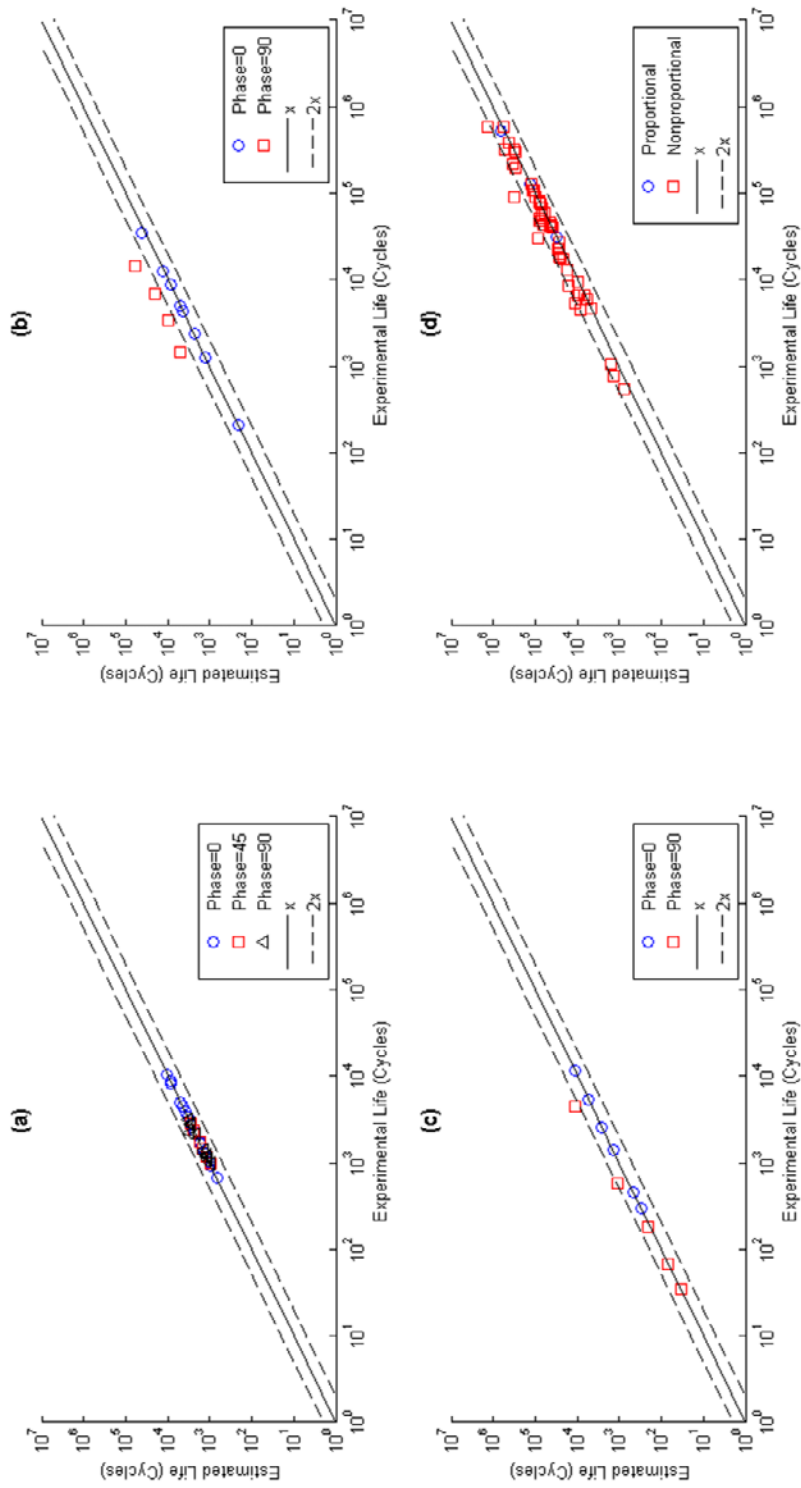


Figure 4-23: Results from the proposed assessment method for Fatemi-Socie model; using (a) Albinmousa et al. [3,72] AZ31B Mg alloy data, (b) Zhang et al. [73] AZ61A Mg alloy data, (c) Xiong et al. [2] AZ31B Mg alloy data, and (d) Hoffmeyer [74] S460N structural steel alloy data.

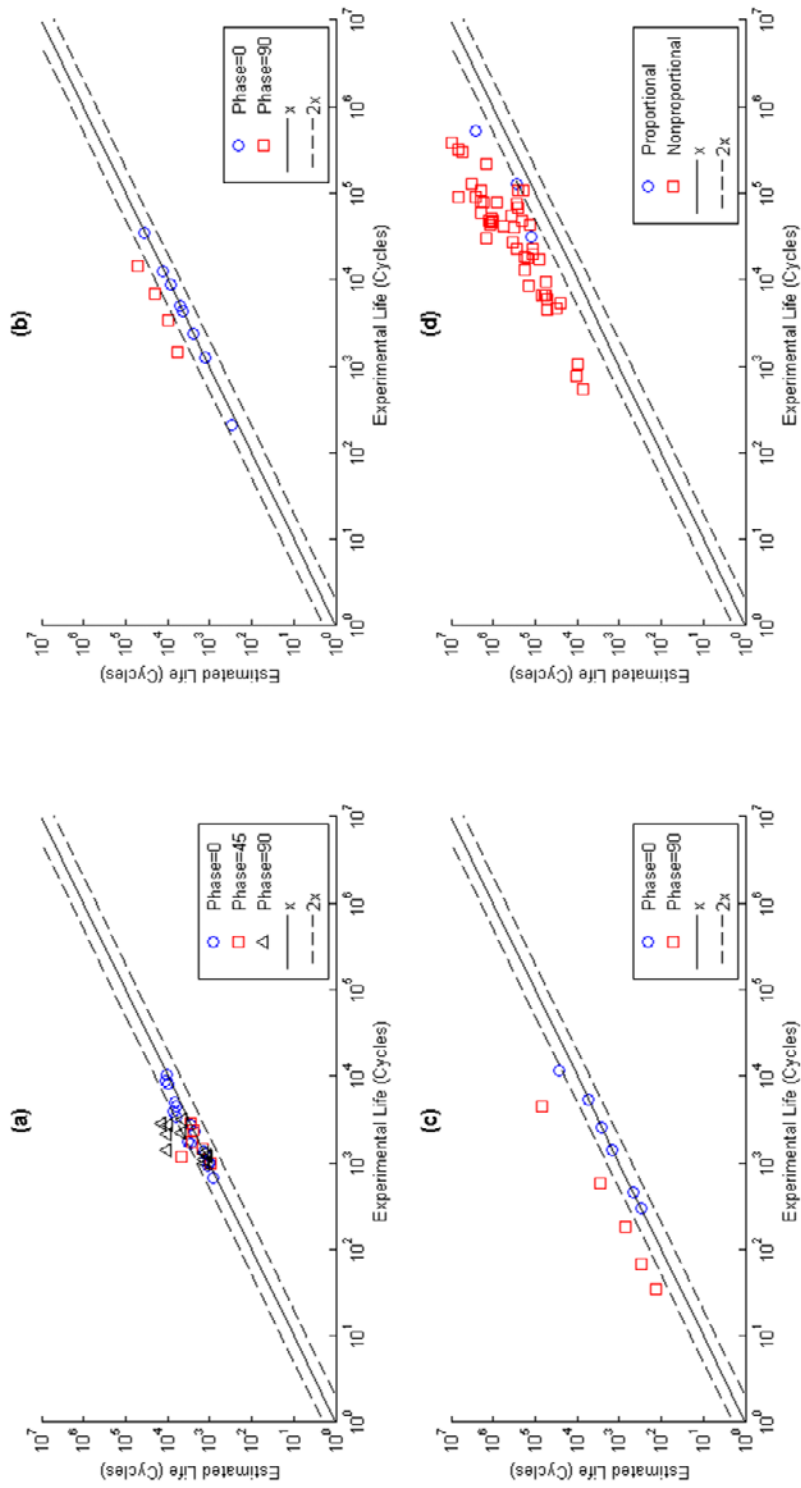


Figure 4-24: Results from the proposed assessment method for Smith-Watson-Topper model; using (a) Albinmousa et al. [3,72] AZ31B Mg alloy data, (b) Zhang et al. [73] AZ61A Mg alloy data, (c) Xiong et al. [2] AZ31B Mg alloy data, and (d) Hoffmeyer [74] S460N structural steel alloy data.

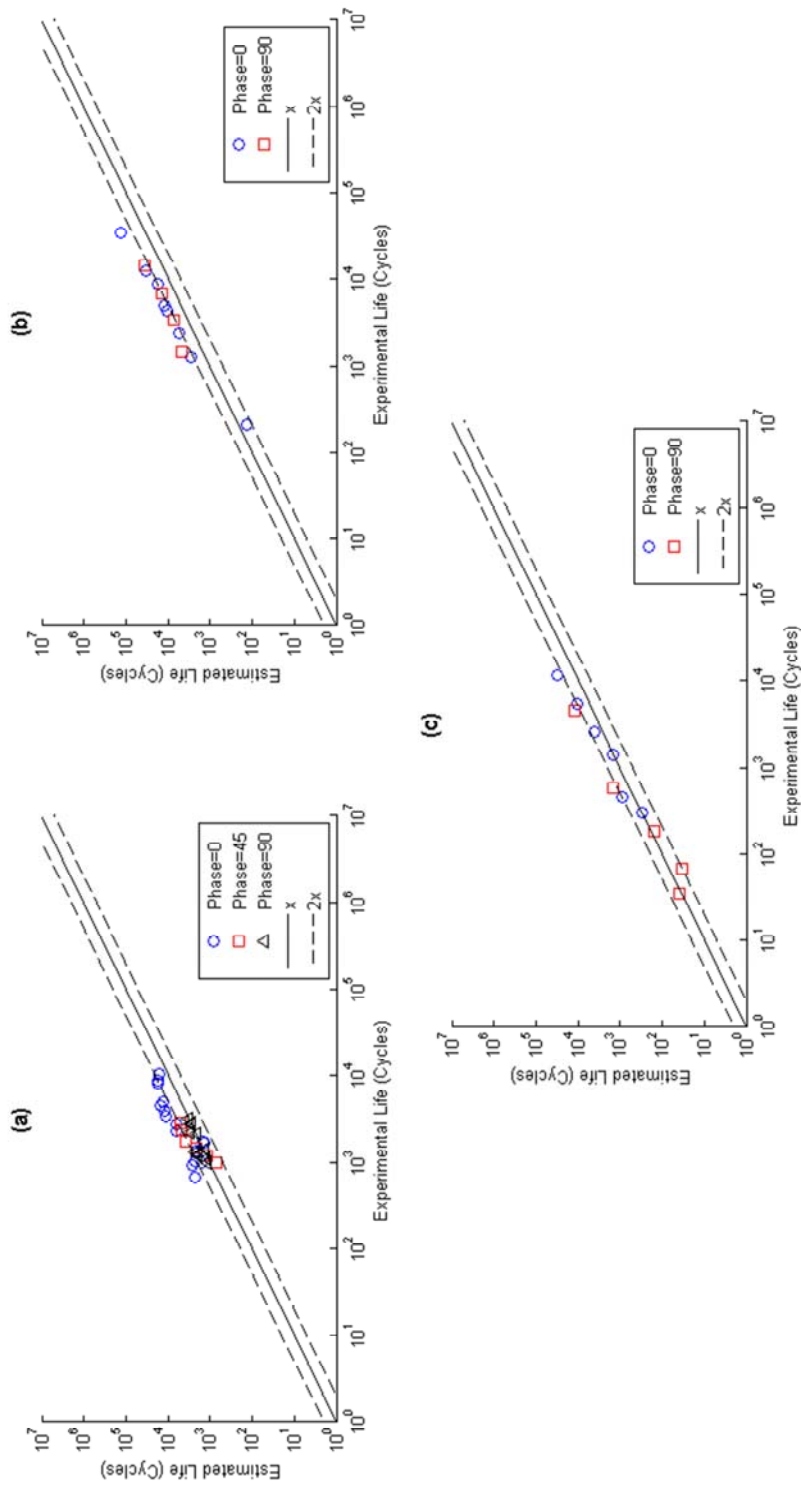


Figure 4-25: Results from the proposed assessment method for Jahed-Varvani model; using (a) Albinmousa et al. [3,72] AZ31B Mg alloy data, (b) Zhang et al.

[73] AZ61A Mg alloy data, and (c) Xiong et al. [2] AZ31B Mg alloy data.

4.4 Proposed Damage Model Results

4.4.1 Notch Root

Figure 4-26 shows the Fatemi-Socie fatigue damage values versus experimental lives for the SAE 1045 notched shaft data. The error bars show the scatter in the observed life data for some of the repeated loading points. The marker shows the mean whereas the bars show the minimum and maximum values of observed lives recorded for the same loading. Mean experimental life for specimens with same loading are used in all the calculations to lower the error in the life data. It can be seen from Figure 4-26 that the damage values of the notched shaft are under-estimated at lower lives while they are over-estimated at higher lives in comparison to the perfect estimation line. Figure 4-26 suggests that the damage scatter needs to be translated and rotated to get close to the perfect estimation line for accurate fatigue life estimations. This observation supports the idea that there should be two notch geometric correction factors, one which translates and the other which rotates the damage scatter. The notch geometric correction factors g_1 and g_2 can be thought of as rotation and translation, respectively, of the damage scatter band.

Table 4-3 shows that the critical plane for all the pure bending loadings occur at the same angle. The θ and \emptyset values show the crack normal direction whereas the ‘xy’ and ‘xz’ shows the type and direction of crack. As discussed in Section 3.4.4, the critical plane analysis is done by considering the damage parameters FP_1 and FP_2 in Eqs. (3-11) and (3-12). If the maximum value of FP_1 (from all the plane angles) is greater than that of FP_2 ,

then it is ‘xy’ crack case. However, if the maximum value of FP_1 (from all the plane angles) is lesser than that of FP_2 , then it is ‘xz’ crack case. Like pure bending loadings, the critical plane for all the pure torsion loadings also occur at the same angle. Figure 4-27a and Figure 4-27b show the fitting of the bending and torsion data, respectively, with the perfect estimation line. The perfect estimation line is plotted based on the approach explained in Section 2.1.2. This approach is used to examine the capability of the proposed and Fatemi-Socie models in correlating the multiaxial fatigue damage with fatigue life. In Figure 4-27a, the last point is not used in fitting because it is the only point in the high cycle region. In Figure 4-27b, IL-TR1-1 data point is not used in fitting because it is away from the trend (also evident from two other repeated tests which have half the life). The fitting results for both the pure bending and pure torsion loadings are shown in Table 4-4. As it can be observed that the value of g_2 is in the order of the shear strain.

Figure 4-28a shows the damage scatter for all the four loading types using the Fatemi-Socie model. As discussed above, the damage values are under-estimated in the low cycle region whereas they are over-estimated than the perfect estimation line in the high cycle region. Figure 4-28b shows the damage scatter for all the four loading types using the proposed model which take into account the geometric effects introduced by the notch in the geometry. As can be seen that the damage scatter is now closer and evenly spread around the perfect estimation line. To assess the capability of the proposed damage model, the damage scatter of the proposed damage model is compared to that of the Fatemi-Socie model. Two measures, the Mean Absolute Percentage Error (MAPE) and Mean Percentage

Error (MPE), are used to compare the Fatemi-Socie model and proposed damage model. The MAPE shows the model's tendency to estimate accurate results while MPE shows the model's tendency to over-estimate or under-estimate the results. The MAPE and MPE were determined using the following formulae:

$$MAPE = \frac{\sum_{i=1}^n \left| \frac{a_i - f_i}{a_i} \right|}{n} \times 100\% \quad (4-1)$$

$$MPE = \frac{\sum_{i=1}^n \left(\frac{a_i - f_i}{a_i} \right)}{n} \times 100\% \quad (4-2)$$

Using Fatemi-Socie model, the damage scatter has MAPE of 18.42% and MPE of -5.54%. Using proposed damage model, the damage scatter has MAPE of 14.00% and MPE of 0.35%. The proposed damage model has reduced the MAPE by 24.00%, which means that the proposed model has better accuracy than the Fatemi-Socie model. Thus, the proposed model can estimate the fatigue lives with better accuracy. In addition, the Fatemi-Socie model has a tendency to over-estimate the damage as shown by the negative MPE. However, the MPE of the proposed damage model is 0.35% which shows that it does not greatly over-estimate or under-estimate the damage.

The fatigue lives are estimated from the proposed model damage values using the nonlinear equation Eq. (3-21). The fatigue life estimation capability of both the Fatemi-Socie model and the proposed damage model are compared with each other on the basis of

factor bands of ± 3 , ± 2.5 and ± 2 as shown in Figure 4-29 to Figure 4-31. The Fatemi-Socie model over-estimates life in the low cycle region while it under-estimates life in the high cycle region, thus it correlates life within factors of ± 3 . However, the proposed model does not greatly under-estimate or over-estimate and is able to estimate life within factors of ± 2 . It can be seen from Figure 4-29a to Figure 4-31a that the Fatemi-Socie model mostly estimate fatigue lives within factors of ± 3 . Also, it can be seen from Figure 4-29b to Figure 4-31b that the proposed damage model successfully estimate fatigue lives within factors of ± 2.5 . However, there are some points just outside the factor of ± 2 bands, thus, the proposed damage model can generally be considered to be able to estimate fatigue lives within factors of ± 2 .

Figure 4-32 shows the cumulative probability distribution of fatigue life estimation for all the loading paths using both the Fatemi-Socie model and the proposed damage model. It can be observed that 83.0% of fatigue life data of all the loading paths lie within factors of ± 3 for the Fatemi-Socie model. Whereas for the proposed damage model, 83.0% of fatigue life data of all the loading paths lie within factors of ± 2.5 . This shows significant improvement of the proposed damage model over the Fatemi-Socie model, and shows its potential for more accurate fatigue life estimations.

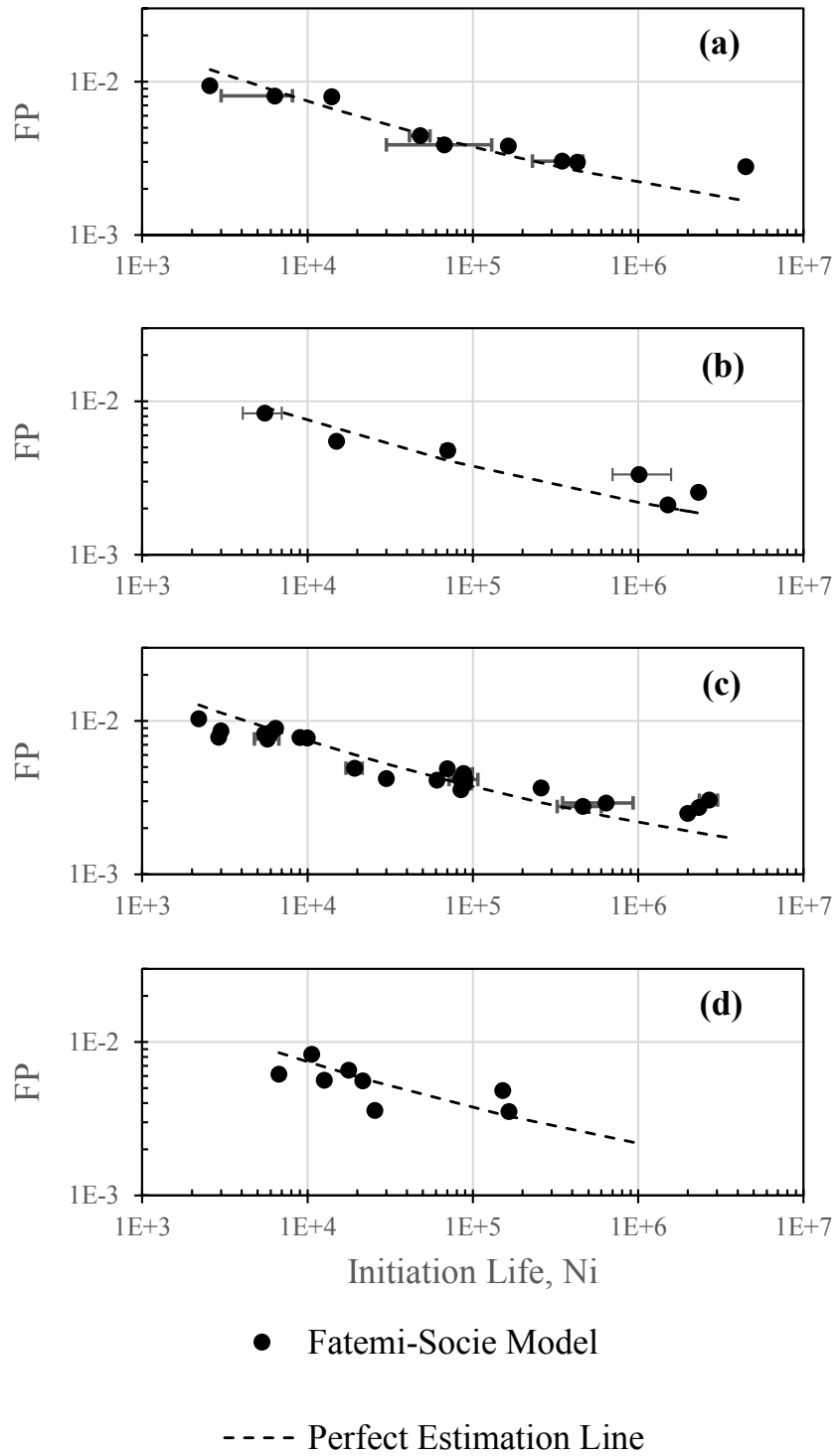


Figure 4-26: Damage-observed life scatter of the Fatemi-Socie model at notch root for SAE shaft.

Table 4-3: Critical plane data at notch root of SAE 1045 notched shaft for all the loading types.

Specimen	Loading	θ	ϕ	Crack	Specimen	Loading	θ	ϕ	Crack
JD-BR3-1	Bending	36	0	xy	IL-XR3-1	In-phase	178	67	xz
IL-BR3-2		36	0	xy	RN-XR3-1		133	34	xy
AOS-BR3-1		36	0	xy	IL-XR3-2		133	34	xy
JD-BR3-2		36	0	xy	IL-XRN-1		178	70	xz
AOS-BR3-2		36	0	xy	JD-XR3-1		134	32	xy
JD-BR2-1		37	0	xy	RN-XR2-1		178	68	xz
BC-BR2-1		37	0	xy	IL-XR2-1		178	68	xz
RN-BR2-1		37	0	xy	JD-XR2-1		178	68	xz
IL-BR2-2		37	0	xy	RN-XR1-1		178	68	xz
IL-BR2-1		37	0	xy	IL-XR1-1		178	68	xz
AOS-BR2-1		37	0	xy	IL-XRN-1		178	72	xz
AOS-BR2-2		37	0	xy	IL-XR2-2		135	23	xy
AOS-BR1-1		38	0	xy	IL-YR2-2		135	23	xy
AOS-BR1-2		38	0	xy	IL-YR3-1		137	19	xy
JD-BR1-1		38	0	xy	IL-YR3-2		137	19	xy
IL-BR1-1		38	0	xy	IL-YR3-1		135	25	xy
JD-TR3-1		Torsion	178	82	xz		IL-YR3-2	In-phase	135
IL-TR3-1	178		82	xz	BC-YR2-1	136	19		xy
BC-TR3-1	178		82	xz	JD-YR1-1	136	18		xy
BC-TR2-1	178		83	xz	JD-YR1-1	133	32		xy
IL-TR2-1	178		83	xz	RN-YR1-1	135	23		xy
GKN-TR1-1	178		84	xz	IL-YR1-1	135	23		xy
RN-TR1-1	178		84	xz	IL-YRN-1	133	29		xy
IL-TR1-1	178		84	xz	IL-YRN-2	133	29		xy
JD-TR0-1	178		84	xz	IL-ZR3-1	178	73		xz
JD-TR0-2	178		85	xz	JD-ZR3-1	178	72		xz
JD-ZR03-1	90° out-of-phase	178	177	xz	IL-ZR3-1	In-phase	178	75	xz
JD-XR03-1		178	174	xz	IL-ZR3-2		178	75	xz
JD-XR03-2		178	175	xz	IL-ZR2-1		178	75	xz
BC-XR03-1		178	175	xz	IL-ZR2-2		178	75	xz
JD-YR03-1		37	178	xy	IL-ZR2-3		178	77	xz
JD-ZR03-2		178	178	xz	IL-ZR2-4		178	77	xz
BC-XR03-1		178	177	xz	JD-ZR2-1		178	72	xz
JD-XR02-1		178	177	xz	IL-ZRN-2		178	77	xz
JD-XR02-2		178	177	xz	IL-ZRN-1		178	77	xz

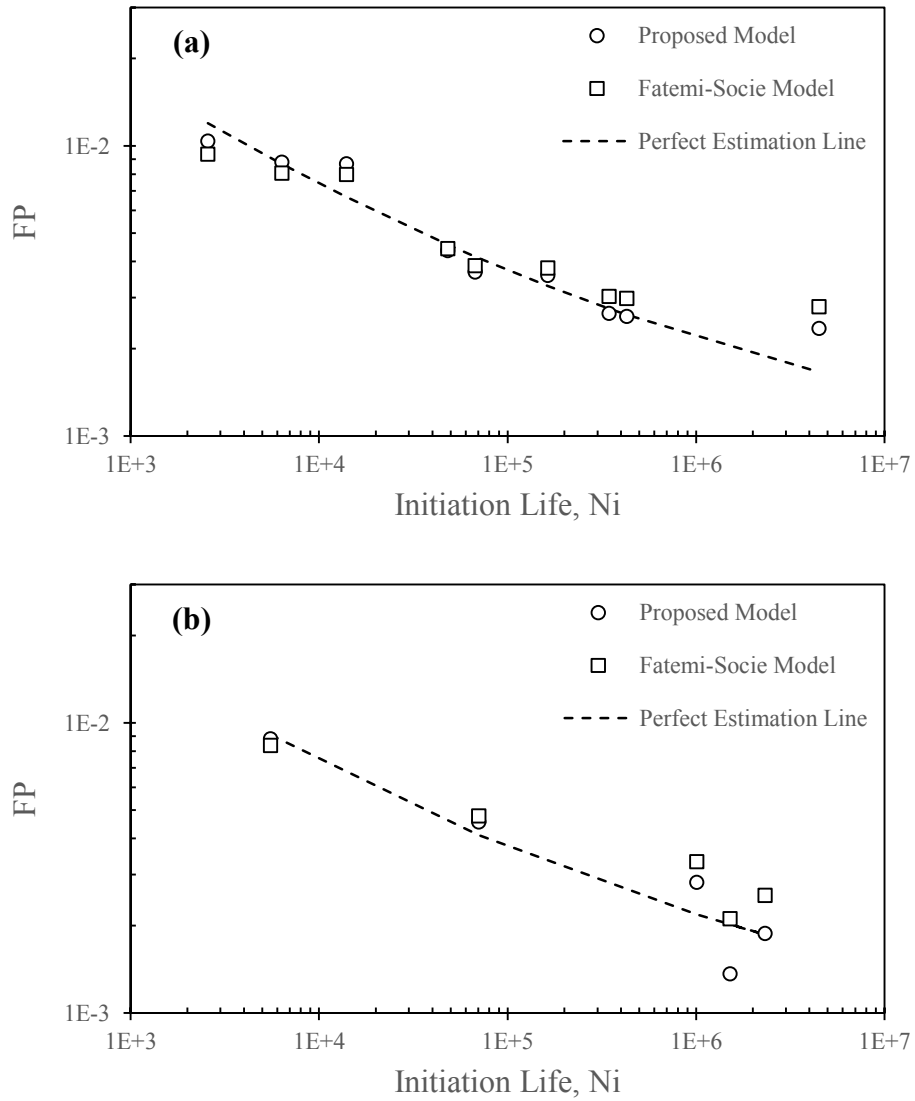


Figure 4-27: Fitting of notch damage scatter with the perfect estimation line for SAE 1045 notched shaft, using; (a) For pure bending loading, (b) For pure torsion loading.

Table 4-4: Fitting results for the proposed model at the notch root for SAE 1045 notched shaft.

Loading	g_1	g_2
Pure Bending	0.3249	-0.001169
Pure Torsion	0.2164	-0.001189

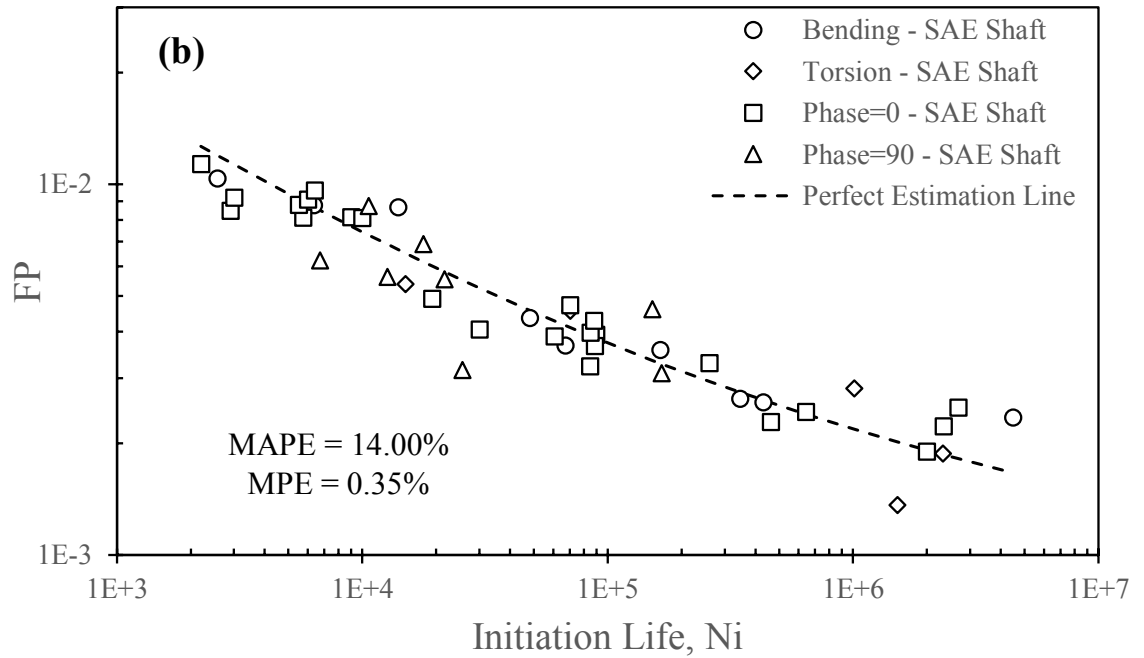
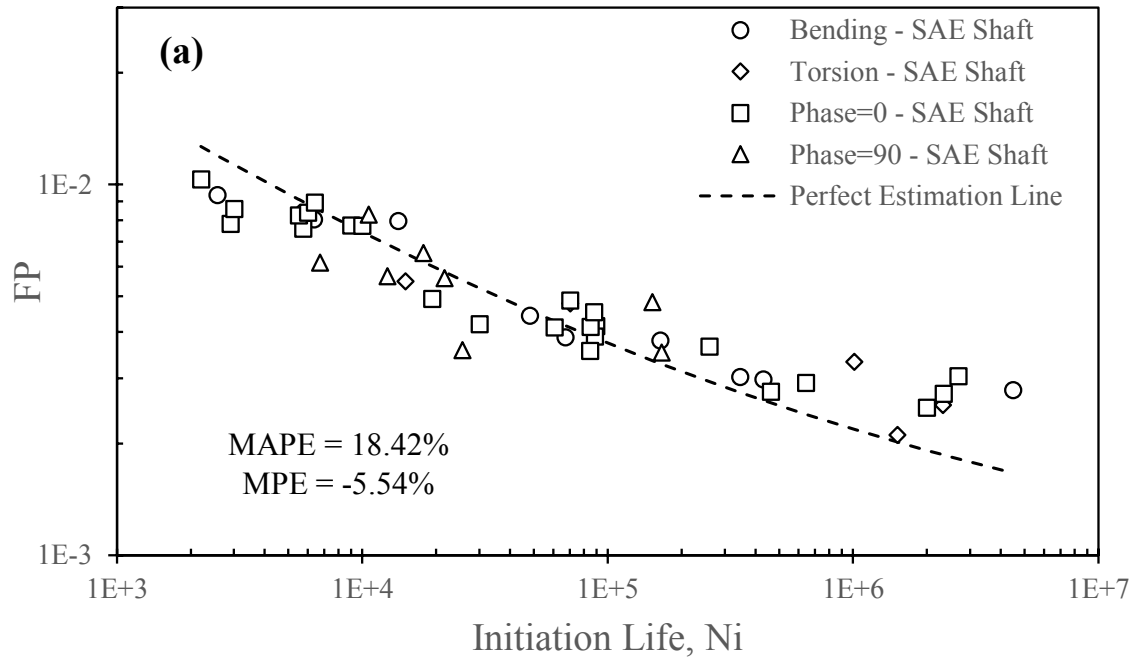


Figure 4-28: Damage-observed life scatter at notch root of SAE 1045 notched shaft for all loading types; (a) Fatemi-Socie model, (b) Proposed damage model.

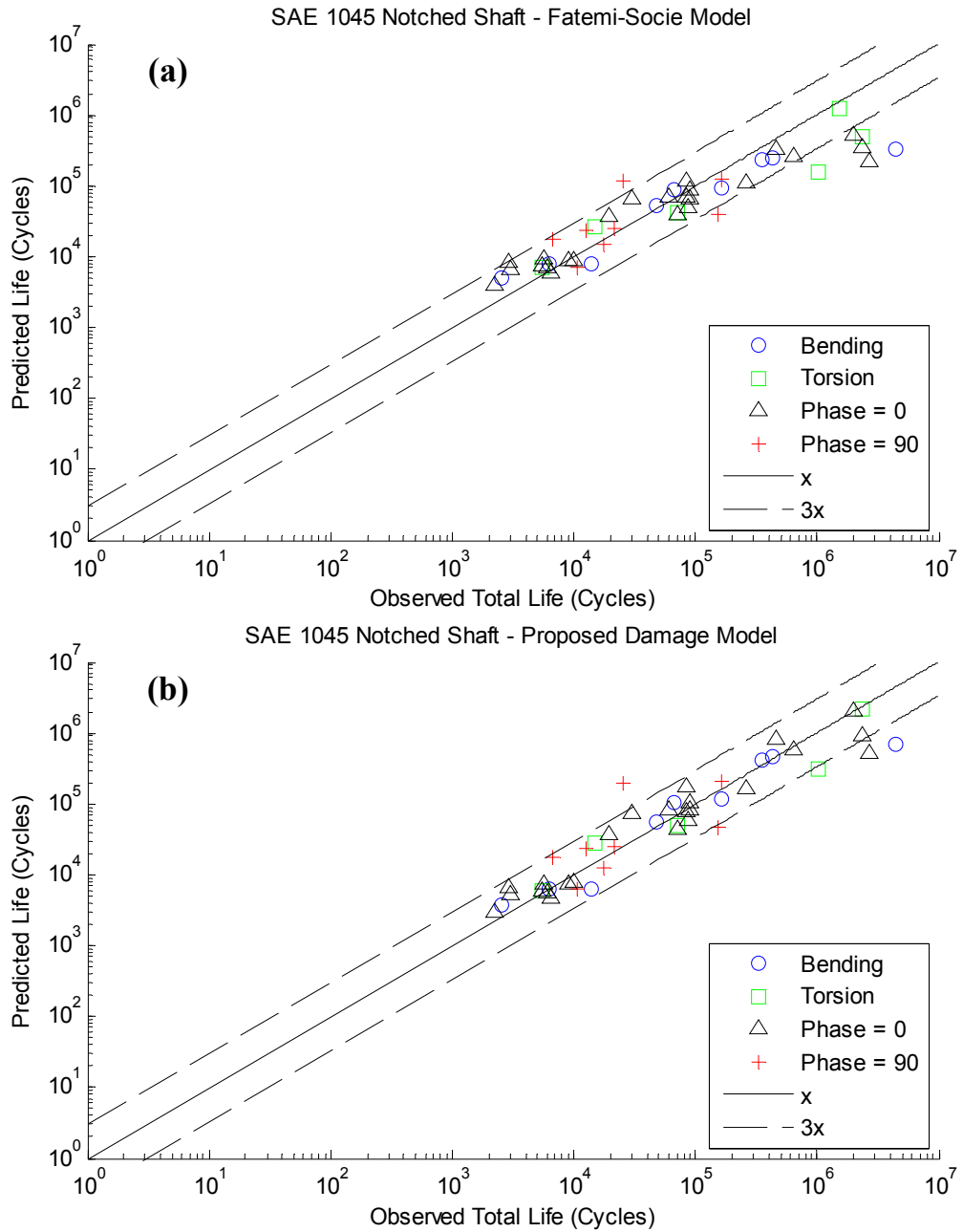


Figure 4-29: Fatigue life estimation capability of the model within a factor of 3; (a) Fatemi-Socie model, (b) Proposed damage model.

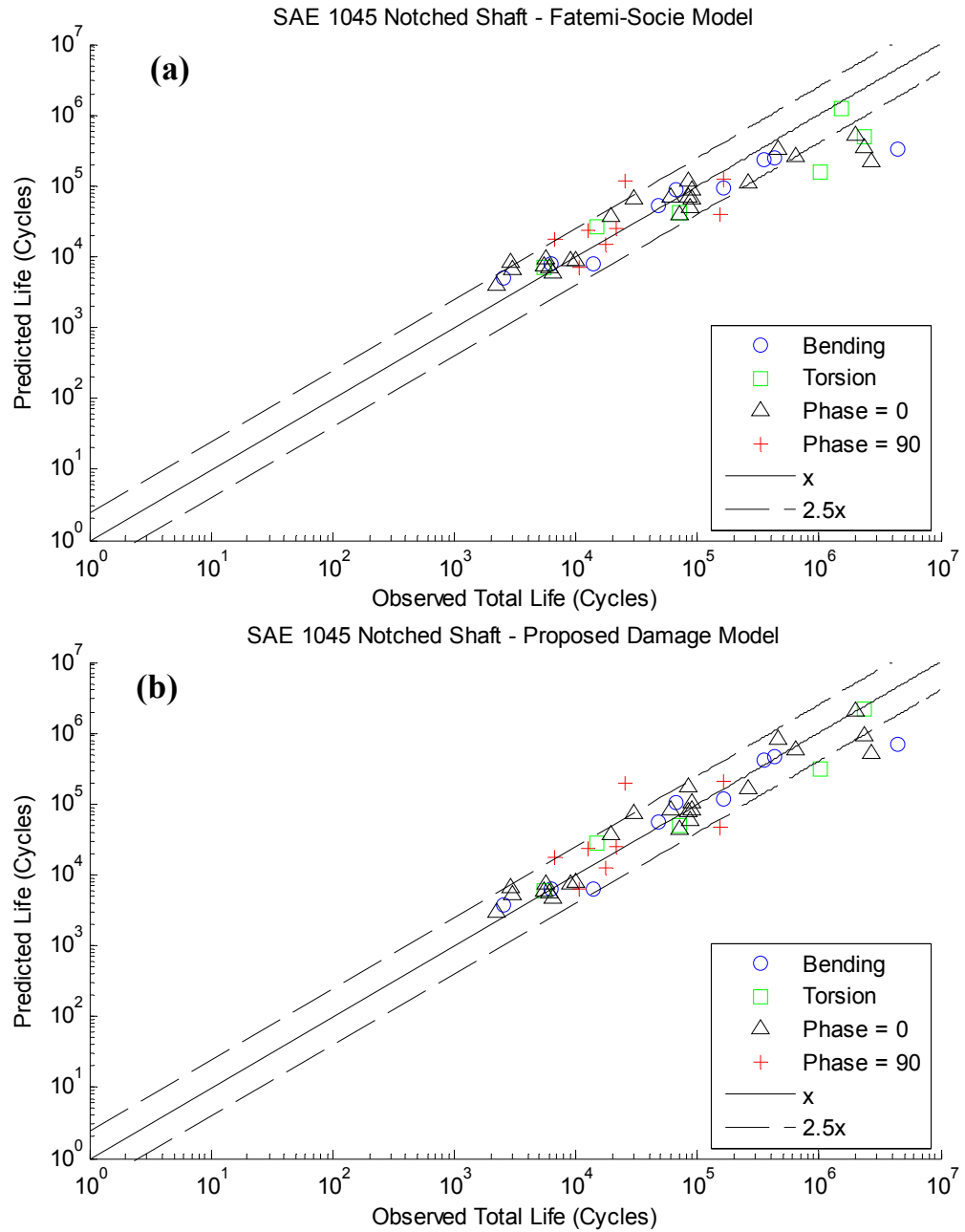


Figure 4-30: Fatigue life estimation capability of the model within a factor of 2.5; (a) Fatemi-Socie model, (b) Proposed damage model.

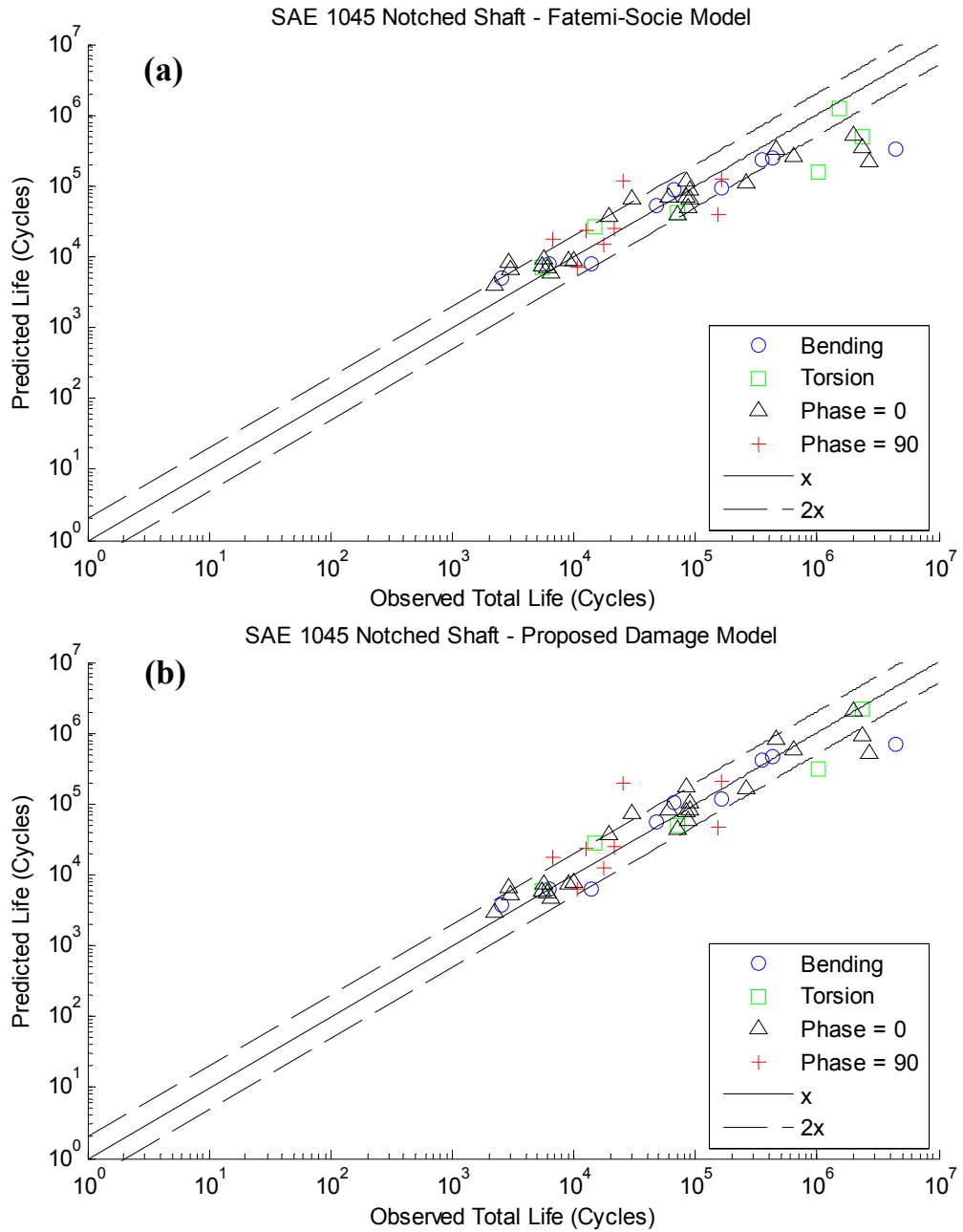


Figure 4-31: Fatigue life estimation capability of the model within a factor of 2; (a) Fatemi-Socie model, (b) Proposed damage model.

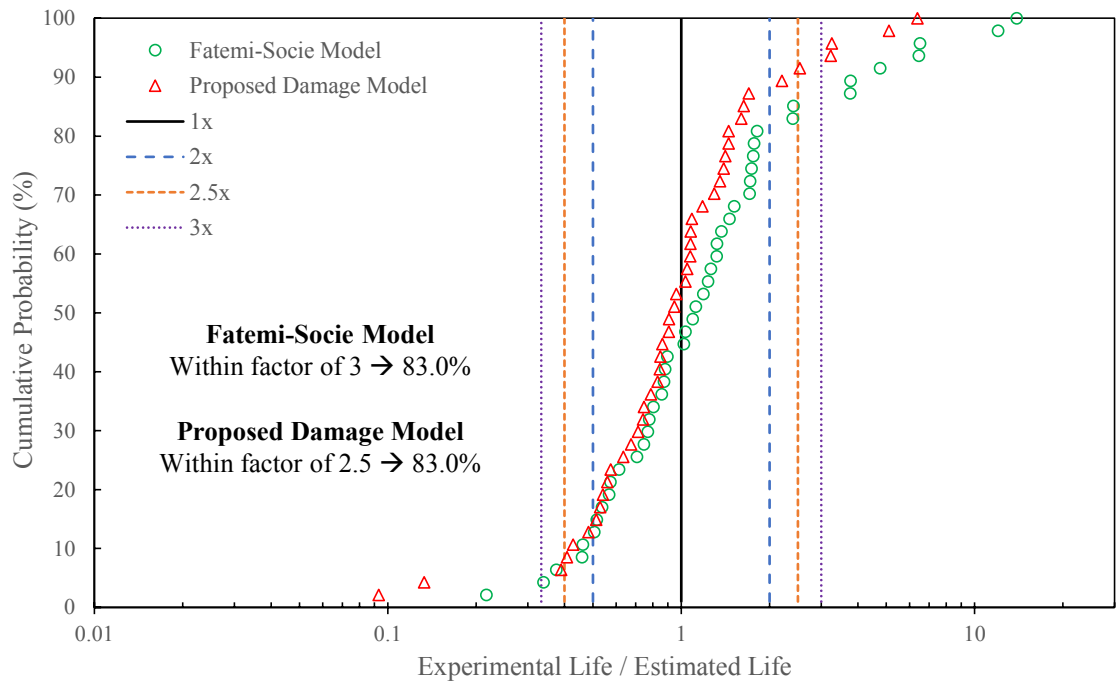


Figure 4-32: Cumulative probability distribution of SAE shaft at notch root for all loading paths.

4.4.2 Max von-Mises Location

Figure 4-33 shows the Fatemi-Socie fatigue damage values versus experimental lives for the SAE 1045 notched shaft at the maximum von-Mises location. The mean experimental life for specimens with same loading are used in all the calculations to lower the error in the life data. It can be seen that damage values of the notched shaft are mostly under-estimated at lower lives while they are over-estimated at higher lives in comparison to the perfect estimation line. Like notch root results, a similar observation can be made here that the damage scatter needs to be translated and rotated to get close to the perfect estimation line for accurate fatigue life estimations. Again, this observation supports the idea that there should be two notch geometric correction factors, one which translates and

the other which rotates the damage scatter. The notch geometric correction factors g_1 and g_2 can be thought of as rotation and translation, respectively, of the damage scatter band.

Figure 4-34a and Figure 4-34b show the fitting of the bending and torsion data, respectively, with the perfect estimation line. In Figure 4-34a, the last point is not used in fitting because it is the only point in the high cycle region. In Figure 4-34b, IL-TR1-1 data point is not used in fitting because it is away from the trend (also evident from two other repeated tests which have half the life). The fitting results for both the pure bending and pure torsion loadings are shown in Table 4-5. As it can be observed that the value of g_2 is in the order of the shear strain.

Figure 4-35a shows the damage scatter for all the four loading types using the Fatemi-Socie model. As discussed above, the damage values are under-estimated in the low cycle region whereas they are over-estimated than the perfect estimation line in the high cycle region. The damage scatter has MAPE of 25.48% and MPE of -20.31%. Figure 4-35b shows the damage scatter for all the four loading types using the proposed damage model which take into account the geometric effects introduced by the notch in the geometry. As can be seen that the damage scatter is now closer and evenly spread around the perfect estimation line. The damage scatter has MAPE of 14.56% and MPE of 2.43%. The proposed damage model has reduced the MAPE by 42.86%, which means that the proposed model has better accuracy than the Fatemi-Socie model. Thus, the proposed model can estimate the fatigue lives with better accuracy. In addition, the Fatemi-Socie model has a

tendency to over-estimate the damage as shown by the negative MPE. However, the MPE of the proposed model is 2.43% which shows that it slightly under-estimate the damage.

The fatigue lives are estimated from the proposed model damage values using the nonlinear equation Eq. (3-21). The fatigue life estimation capability of both the Fatemi-Socie model and proposed damage model are compared with each other on the basis of factor bands of ± 3 , ± 2.5 and ± 2 as shown in Figure 4-36 to Figure 4-38. The Fatemi-Socie model under-estimates life in the high cycle region, thus it correlates life within factors of ± 3 . However, the proposed damage model does not greatly under-estimate or over-estimate and is able to estimate life within factors of ± 2 . It can be seen from Figure 4-36a to Figure 4-38a that the Fatemi-Socie model mostly estimate fatigue lives within factors of ± 3 . Also, it can be seen from Figure 4-36b to Figure 4-38b that the proposed damage model successfully estimate fatigue lives within factors of ± 2.5 . However, there are some points just outside the factor of ± 2 bands, thus, the proposed damage model can generally be considered to be able to estimate fatigue lives within factors of ± 2 .

Figure 4-39 shows the cumulative probability distribution of fatigue life estimation for all the loading paths using both the Fatemi-Socie model and the proposed damage model. It can be observed that 70.2% of fatigue life data of all the loading paths falls within factors of ± 3 for the Fatemi-Socie model. Whereas for the proposed damage model, 68.1% and 83.0% of fatigue life data of all the loading paths falls within factors of ± 2 and ± 2.5 ,

respectively. This shows significant improvement of the proposed damage model over the Fatemi-Socie model, and shows its potential for more accurate fatigue life estimations.

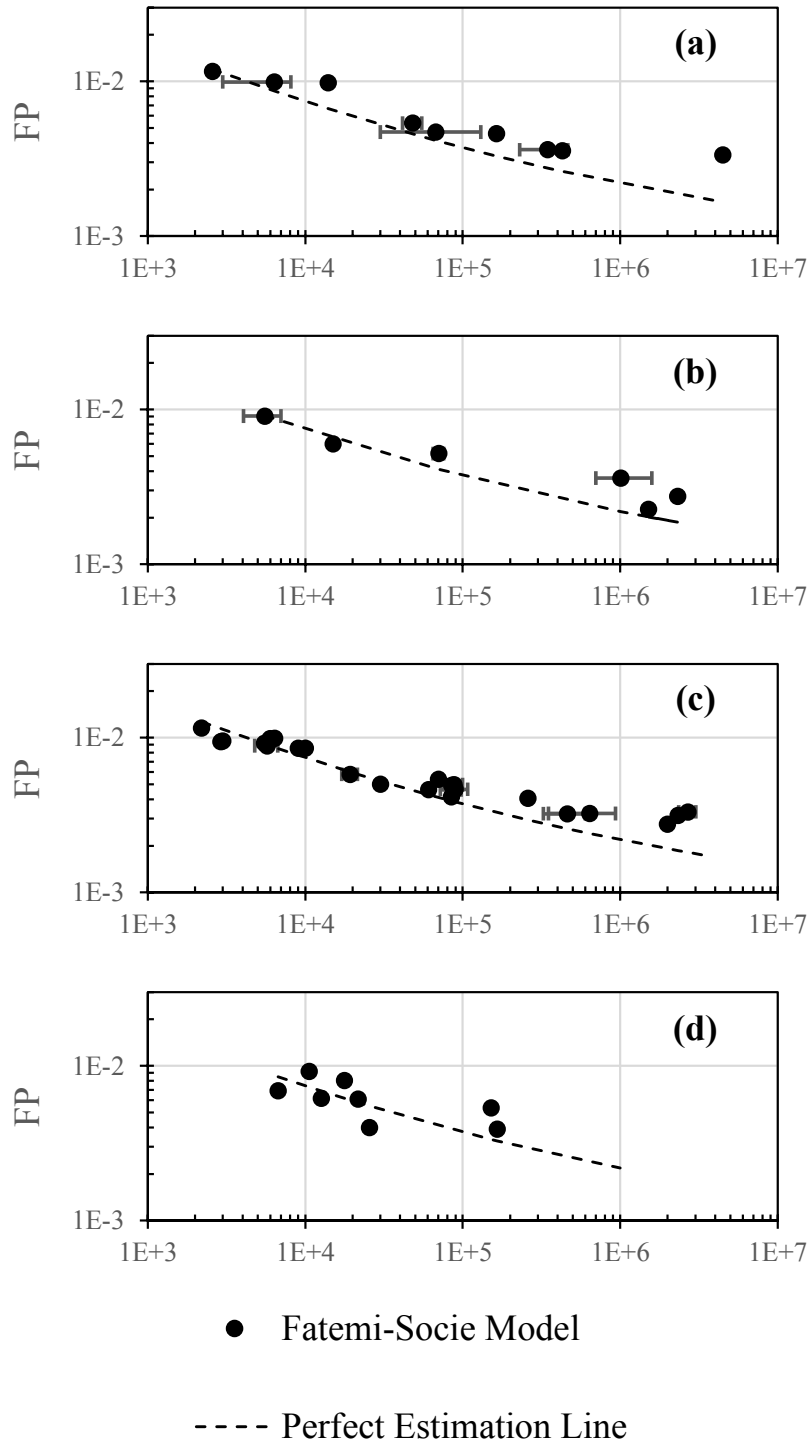


Figure 4-33: Damage-observed life scatter of the Fatemi-Socie model for SAE 1045 notched shaft.

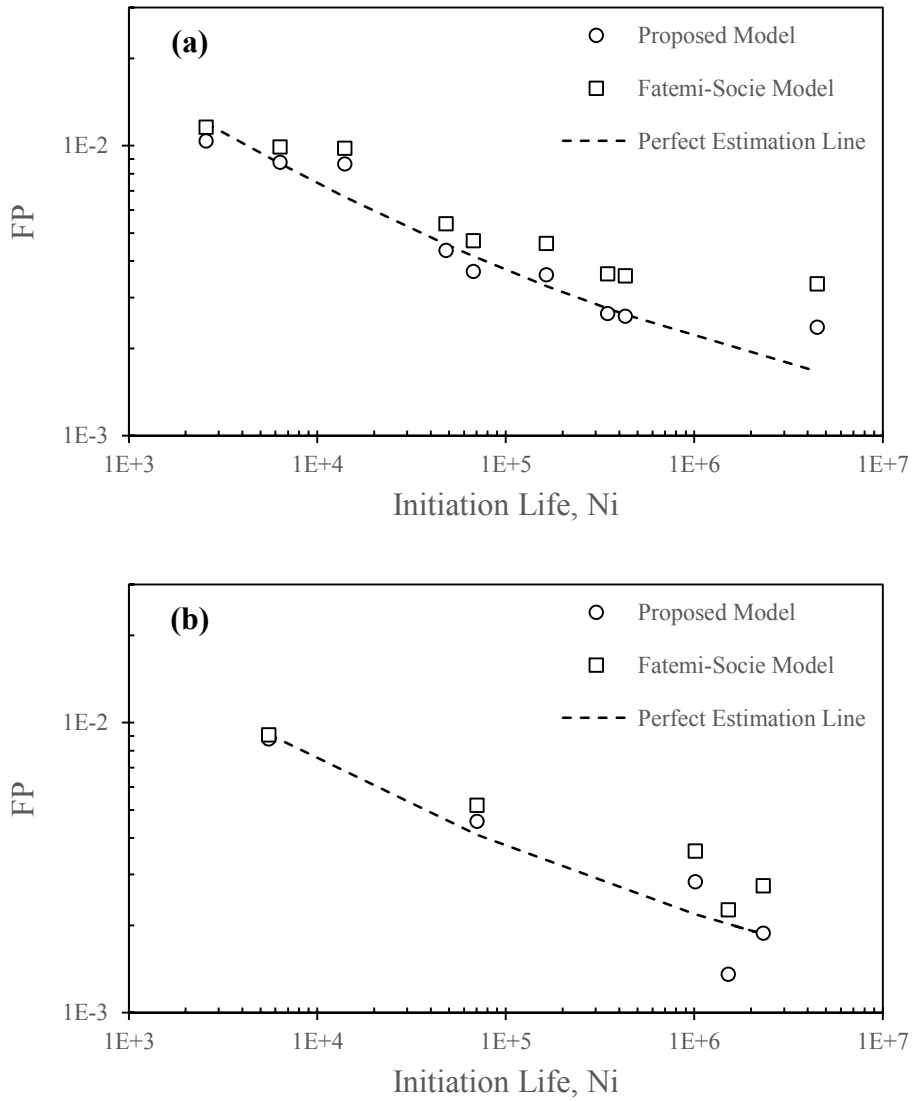


Figure 4-34: Fitting of notch damage scatter with the perfect estimation line; (a) For pure bending loading, (b) For pure torsion loading.

Table 4-5: Fitting results for the proposed model at maximum von-Mises node.

Loading	g_1	g_2
Pure Bending	-0.03857	-0.0008723
Pure Torsion	0.1048	-0.001136

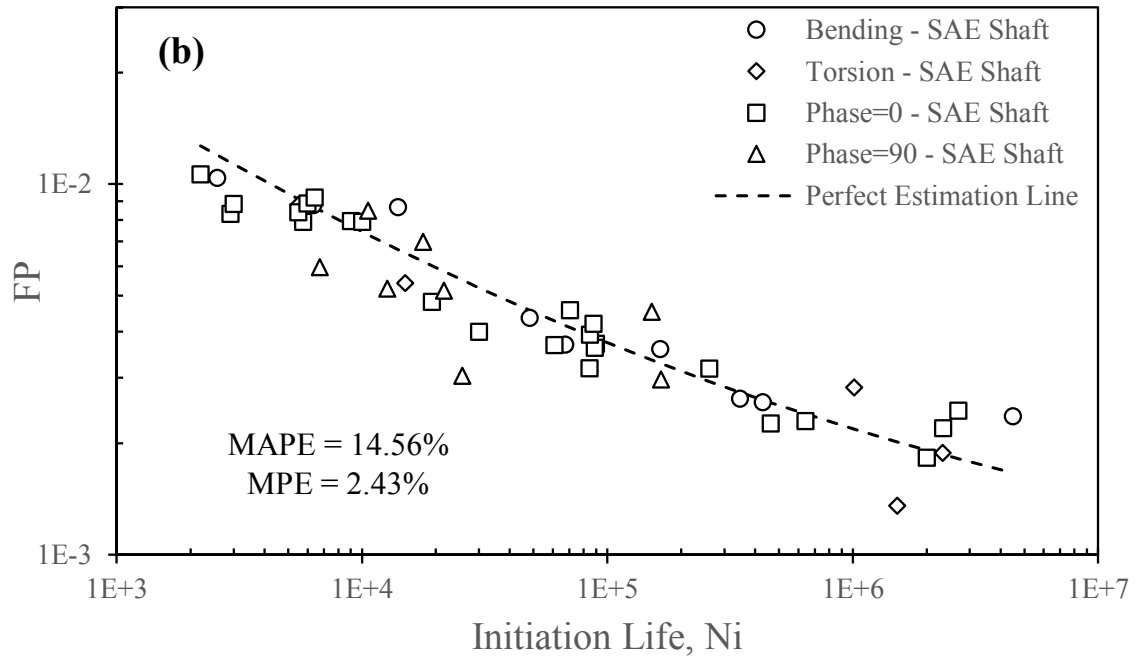
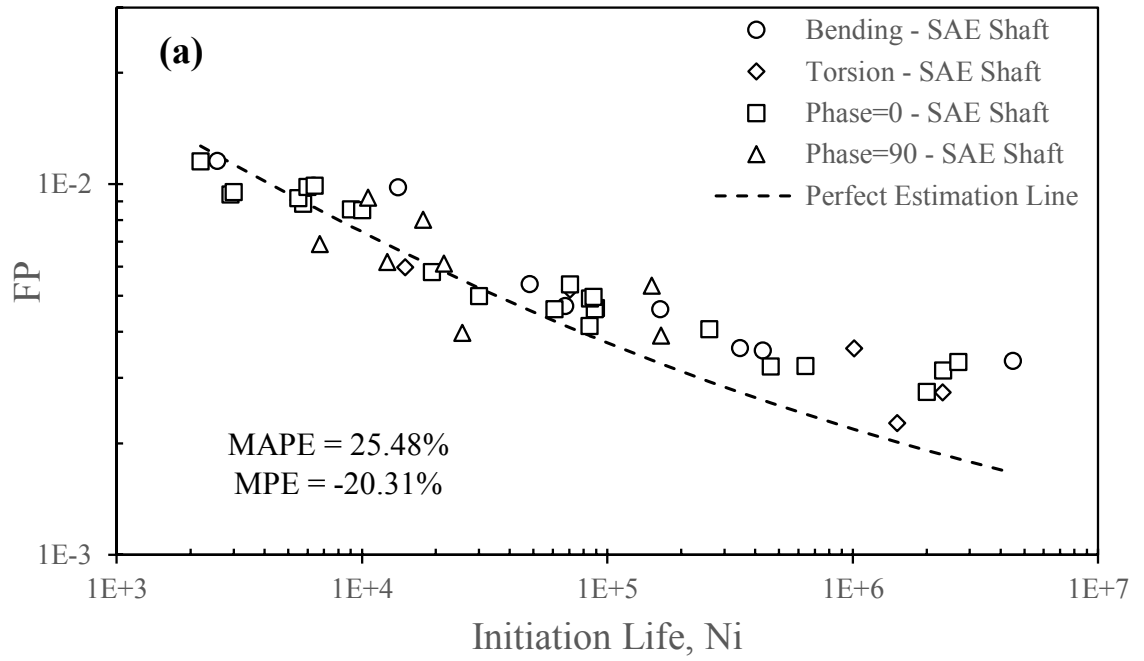


Figure 4-35: Damage-observed life scatter for all loading types; (a) Fatemi-Soce model, (b) Proposed damage model.

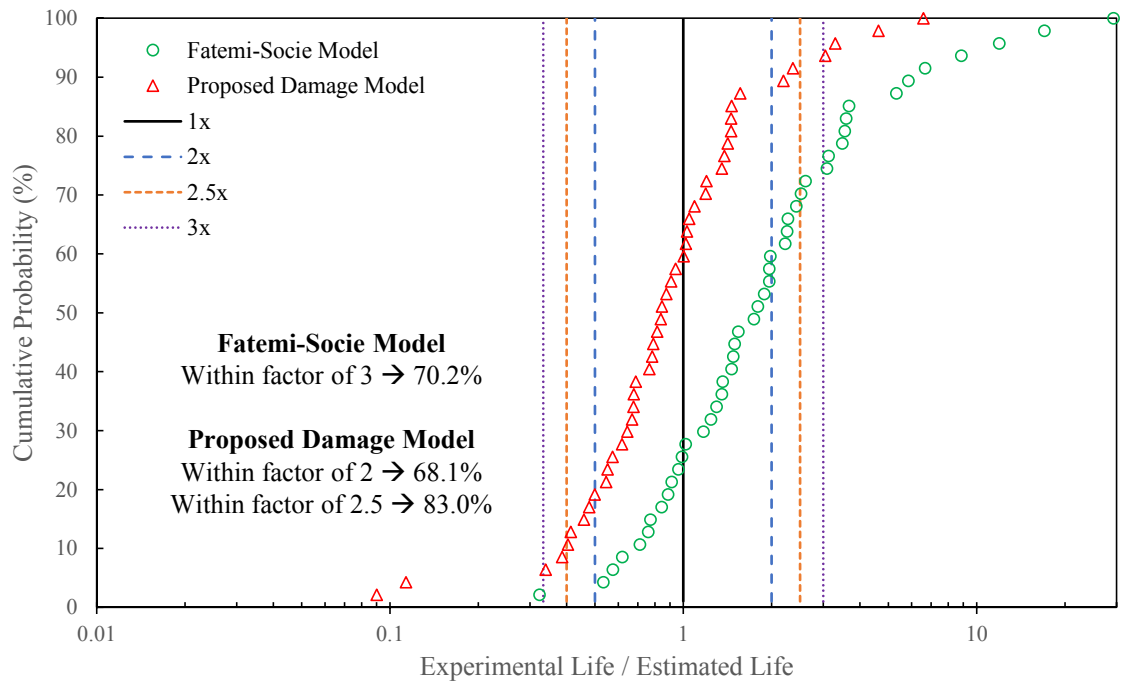


Figure 4-39: Cumulative probability distribution of SAE shaft at maximum von-Mises location for all loading paths.

CHAPTER 5

CONCLUSIONS AND RECOMMENDATIONS

5.1 Conclusions

A computational fatigue design tool is developed using ANSYS Parametric Design Language (APDL) and MATLAB, for the multiaxial fatigue analysis of the notched components. The developed tool can analyze components with complex geometries made from different materials under a variety of loading conditions. The FE analysis is used to determine the elastic-plastic stress-strain histories at the critical locations in the notched component. The multiaxial fatigue analysis utilizes these stress-strain histories to determine the fatigue damage that is used for fatigue life estimation. The following conclusions are drawn from this research:

1. The FE model used for estimation of notch stress-strain histories is validated using the measured strains using strain-rosette mounted on the SAE 1045 notched shaft.
2. A screening method is proposed to compare different critical plane based fatigue damage models to select the best model that can estimate fatigue lives most accurately for smooth specimens. The proposed assessment method results suggest

that the Fatemi-Socie model provide better fatigue life estimations for smooth specimens than the Smith-Watson-Topper and Jahed-Varvani models.

3. The selected model, Fatemi-Socie model, is modified to take into account the notch geometrical effects to improve its fatigue life estimation for notched components. Taking the notch root as the critical location, the Fatemi-Socie model damage scatter has MAPE of 18.42% and MPE of -5.54%, whereas the proposed model damage scatter has MAPE of 14.00% and MPE of 0.35%. Thus, the proposed model improves the fatigue life estimation and removes the large over-estimation tendency of the Fatemi-Socie model.
4. Similarly, for maximum von-Mises location in the vicinity of notch region as the critical location, the Fatemi-Socie model damage scatter has MAPE of 25.48% and MPE of -20.31%, whereas the proposed model damage scatter has MAPE of 14.56% and MPE of 2.43%. Thus, the proposed model improves the fatigue life estimation and removes the large over-estimation tendency of the Fatemi-Socie model.
5. The proposed damage model significantly improves fatigue life estimation over that of the Fatemi-Socie model. For notch root as critical location, the Fatemi-Socie model estimated 83.0% of fatigue life data of all the loading paths within factor of ± 3 , whereas the proposed damage model estimated 83.0% of it within factor of ± 2.5 . For maximum von-Mises location in the vicinity of notch root as the critical location, the Fatemi-Socie model estimated 70.2% of fatigue life data of all the loading paths falls within factor of ± 3 , whereas the proposed damage model

estimated 68.1% and 83.0% of it within factor of ± 2 and ± 2.5 , respectively. This shows the potential of the proposed damage model for more accurate fatigue life estimations.

6. The proposed damage model is developed to serve industry, as it is a simple model capable of estimating the fatigue lives of industrial notched components with nearly the same accuracy as that of the laboratory smooth specimens. It just demands a few extra tests of the notched components under pure bending and pure torsional loadings. The automobile industries uses fatigue as design tool for load-bearing structural components. As the proposed damage model improved the fatigue life estimation accuracy, so the design of structural components can be carried out using lower safety factors for cost savings. The automobile companies like Ford, General Motors, Chrysler, Toyota, Honda, Volkswagen; produce thousands of vehicles every year. Therefore, an improvement in fatigue estimation by the proposed model will enable them to design their automobiles with lower safety factors, which implies less material usage and less weight of vehicles. The less weight of vehicle further improves fuel efficiency of the vehicle and reduces the carbon tax.

5.2 Recommendations

The developed fatigue damage model estimates fatigue lives of the notched shafts with nearly the same accuracy level as that of the smooth specimens. Thus, the notch geometric correction factors has a great potential for use in different industries such as automobiles

for the fatigue life estimation of notched components, especially the notched shafts. In the future, this methodology should be extended in the following ways:

1. A suitable geometric equation should be developed, which can be used instead of the weight function, to calculate the notch geometric correction factors for multiaxial loadings. This equation will take into account both the bending and torsion geometric correction factors as well as the bending and torsion loading amplitudes to calculate the notch geometric correction factors to be used in the damage parameter.
2. This methodology should be extended to variety of notch geometries. Additional fatigue tests (pure bending, pure torsion and multiaxial) should be conducted on components of different notch geometries. The fatigue data from these tests should be used to generalize the geometric correction factors in the proposed damage model for variety of notch geometries.

NOMENCLATURE

A	instantaneous cross-sectional area
A_o	original cross-sectional area
b	axial fatigue strength exponent
b_s	torsional fatigue strength exponent
B	axial energy-based fatigue strength exponent
B_s	torsional energy-based fatigue strength exponent
c	axial fatigue ductility exponent
c_s	torsional fatigue ductility exponent
C	axial energy-based fatigue toughness exponent
C_s	torsional energy-based fatigue toughness exponent
D	diameter
ΔE	total strain energy density
ΔE_A	axial strain energy density
ΔE_T	torsional strain energy density
$\Delta \varepsilon_1$	principal normal strain range
$\Delta \gamma_{max}$	maximum shear strain range
e	engineering strain
E	tensile modulus of elasticity
E_T	tangent modulus
E'_e	axial energy-based fatigue strength coefficient

E'_f	axial energy-based fatigue toughness coefficient
ε	true strain
ε_e	elastic strain
ε_{ij}	strain tensor
ε_p	plastic strain
ε_t	total strain
ε'_f	axial fatigue ductility coefficient
f	yield function
g_1, g_2	geometric correction factors
G	shear modulus
γ	shear strain
γ_e	elastic shear strain
γ_p	plastic shear strain
γ'_f	torsional fatigue ductility coefficient
J	polar moment of inertia
k	Fatemi-Socie constant
K	monotonic tensile strength coefficient
K_ε	strain concentration factor
K_f	notch fatigue factor
K_σ	stress concentration factor
K_t	elastic stress concentration factor
K'	cyclic axial strength coefficient

K'_S	cyclic torsional strength coefficient
l	extended length
l_o	original length
M	transformation or rotation matrix
M_b	bending moment
M_t	torsional moment
M^T	transpose of transformation matrix
n	monotonic tensile strain hardening exponent
n'	cyclic axial strain hardening exponent
n'_s	cyclic torsional strain hardening exponent
N_A	fatigue life under purely axial loading
N_f	number of cycles to failure
N_t	transition life
N_{sv}	number of sublayers
N_T	fatigue life under purely torsion loading
P	applied load
ν	Poisson's ratio
r	radius
S	engineering stress
S_y	tensile yield strength
σ	true stress
σ_e	equivalent von-Mises stress

σ_{ij}	stress tensor
σ_m	mean stresses
σ_{nom}	nominal axial stress
$\sigma_{n,max}$	maximum normal stress at critical plane
$\sigma_1, \sigma_2, \sigma_3$	principal stresses
σ'_f	axial fatigue strength coefficient
τ	shear stress
τ_{nom}	nominal shear stress
τ'_f	torsional fatigue strength coefficient
W'_e	torsional energy-based fatigue strength coefficient
W'_f	torsional energy-based fatigue toughness coefficient

REFERENCES

- [1] A. Fatemi, R.I. Stephens, Cyclic Deformation of 1045 Steel Under In-Phase and 90 deg Out-of-Phase Axial--Torsional Loading Conditions, Soc. Automot. Eng. Inc., Multiaxial Fatigue Anal. Exp. (1989) 139–147.
- [2] Y. Xiong, Q. Yu, Y. Jiang, Multiaxial fatigue of extruded AZ31B magnesium alloy, Mater. Sci. Eng. A. 546 (2012) 119–128. doi:10.1016/j.msea.2012.03.039.
- [3] J. Albinmoussa, H. Jahed, Multiaxial effects on LCF behaviour and fatigue failure of AZ31B magnesium extrusion, Int. J. Fatigue. 67 (2014) 103–116. doi:10.1016/j.ijfatigue.2014.01.025.
- [4] S.B. Behravesh, H. Jahed, S.B. Lambert, M. Chengji, Constitutive Modeling for Cyclic Behavior of AZ31B Magnesium Alloy and its Application, Adv. Mater. Res. 891 (2014) 809–814.
- [5] Q. Yu, J. Zhang, Y. Jiang, Q. Li, Multiaxial fatigue of extruded AZ61A magnesium alloy, Int. J. Fatigue. 33 (2011) 437–447. doi:10.1016/j.ijfatigue.2010.09.020.
- [6] Q. Yu, J. Zhang, Y. Jiang, Q. Li, An experimental study on cyclic deformation and fatigue of extruded ZK60 magnesium alloy, Int. J. Fatigue. 36 (2012) 47–58. doi:10.1016/j.ijfatigue.2011.08.016.
- [7] SAE Notched Shaft Test Program, (n.d.). <https://www.efatigue.com/>.
- [8] H. Neuber, Theory of Stress Concentration for Shear-Strained Prismatical Bodies With Arbitrary Nonlinear Stress-Strain Law, J. Appl. Mech. 28 (1961) 544. doi:10.1115/1.3641780.
- [9] K. Molski, G. Glinka, A method of elastic-plastic stress and strain calculation at a notch root, Mater. Sci. Eng. 50 (1981) 93–100. doi:10.1016/0025-5416(81)90089-6.
- [10] P. Kurath, S.D. Downing, D.R. Galliard, Summary of non-hardened notched shaft round robin program, Multiaxial Fatigue Anal. Exp. SAE AE-14 (1989) 13–31.
- [11] D.F. Socie, S.D. Downing, S. Utagawa, Benchmark Problems in Multiaxial Fatigue, 10th Int. Conf. Multiaxial Fatigue Fract. (2013).
- [12] J.W. Fash, D.F. Socie, D.L. McDowell, Fatigue life estimates for a simple notched component under biaxial loading, Multiaxial Fatigue, ASTM STP 853. (1985) 497–513.
- [13] N.E. Dowling, Mechanical Behavior of Materials, 2013.
- [14] W.D. Callister, D.G. Rethwisch, Materials Science and Engineering: An Introduction, Wiley, 2009. doi:10.1016/0025-5416(87)90343-0.
- [15] R.I. Stephens, A. Fatemi, R.R. Stephens, H.O. Fuchs, Metal fatigue in engineering,

John Wiley and Sons, Inc, New Your, 2000.

- [16] D. Roylance, STRESS-STRAIN CURVES, (2001).
- [17] G.E. Dieter, D. Bacon, Mechanical Metallurgy, SI Metric , 1988.
- [18] K.N. Smith, P. Watson, T.H. Topper, Stress-Strain Function for Fatigue of Metals, *J. Mater.* 5 (1970) 767–&. <Go to ISI>://WOS:A1970H915700003.
- [19] ASTM, Standard Practice for Strain-Controlled Axial-Torsional Fatigue Testing with Thin-, *Astm.* 08 (2014) 2–9. doi:10.1520/E2207-08R13.2.
- [20] D.F. Socie, G.B. Marquis, Multiaxial Fatigue, Society of Automotive Engineers, Inc., Warrendale, Pa. , 2001. https://www.efatigue.com/training/multiaxial_fatigue.pdf.
- [21] A. Fatemi, N. Shamsaei, Multiaxial fatigue: An overview and some approximation models for life estimation, *Int. J. Fatigue.* 33 (2011) 948–958. doi:10.1016/j.ijfatigue.2011.01.003.
- [22] D. Socie, Critical plane approaches for multiaxial fatigue damage assessment, *ASTM Spec. Tech. Publ.* 1191 (1993) 7–36. doi:10.1520/STP24793S.
- [23] A. Fatemi , D.F. Socie~, a Critical Plane Approach To Multiaxial Fatigue Damage Including Out-of-Phase Loading, *Fatigue Fract. Engng Mater. Struct.* 1 (1988) 149–165. doi:10.1111/j.1460-2695.1988.tb01169.x.
- [24] H. Jahed, A. Varvani-Farahani, Upper and lower fatigue life limits model using energy-based fatigue properties, *Int. J. Fatigue.* 28 (2006) 467–473. doi:10.1016/j.ijfatigue.2005.07.039.
- [25] H. Jahed, A. Varvani-Farahani, M. Noban, I. Khalaji, An energy-based fatigue life assessment model for various metallic materials under proportional and non-proportional loading conditions, *Int. J. Fatigue.* 29 (2007) 647–655. doi:10.1016/j.ijfatigue.2006.07.017.
- [26] D. Socie, Multiaxial Fatigue Damage Models, *J. Eng. Mater. Technol.* 109 (1987) 293–298. doi:10.1115/1.3225980.
- [27] J.A. Bin Mousa, Multiaxial Fatigue Characterization and Modeling of AZ31B Magnesium Extrusion, University of Waterloo, 2011.
- [28] W.F. Hosford, *Fundamentals of Engineering Plasticity*, 2013. doi:10.1016/0020-7403(63)90046-8.
- [29] D.W.A. Rees, *Basic Engineering Plasticity : An Introduction with Enginnering and Manufacturing Applications*, First, 2006.
- [30] W. Prager, A New Method of Analyzing Stress and Strains in Work-Hardening Plastic Solids, *J. Appl. Mech.* 23 (1956) 493–496.
- [31] Z. Mróz, On the description of anisotropic workhardening, *J. Mech. Phys. Solids.* 15 (1967) 163–175. doi:10.1016/0022-5096(67)90030-0.

- [32] Y.S. Garud, A New Approach to the Evaluation of Fatigue Under Multiaxial Loadings, *J. Eng. Mater. Technol.* 103 (1981) 118. doi:10.1115/1.3224982.
- [33] Y.F. Dafalias, E.P. Popov, Plastic Internal Variables Formalism of Cyclic Plasticity, *J Appl Mech.* 43 (1977) 645–651.
- [34] F.P. Beer, E.R. Johnston, J.T. DeWolf, D.F. Mazurek, *Mechanics of Materials* (Sixth Edition), (2012) 838.
- [35] A. Ince, G. Glinka, Innovative computational modeling of multiaxial fatigue analysis for notched components, *Int. J. Fatigue.* 82 (2016) 134–145. doi:10.1016/j.ijfatigue.2015.03.019.
- [36] C.-C. Chu, F. Conle, J. Bonnen, Multiaxial Stress-Strain Modeling and Fatigue Life Prediction of SAE Axle Shafts, in: *Adv. Multiaxial Fatigue*, ASTM International, 100 Barr Harbor Drive, PO Box C700, West Conshohocken, PA 19428-2959, 1993: pp. 37–37–18. doi:10.1520/STP24794S.
- [37] W.J. Harvey, Biaxial fatigue of the SAE unnotched shaft test specimen., (1989) 107–119.
- [38] R. Branco, J.D. Costa, F.V. Antunes, Fatigue behaviour and life prediction of lateral notched round bars under bending–torsion loading, *Eng. Fract. Mech.* 119 (2014) 66–84. doi:10.1016/j.engfracmech.2014.02.009.
- [39] N. Gates, A. Fatemi, Notched fatigue behavior and stress analysis under multiaxial states of stress, *Int. J. Fatigue.* 67 (2014) 2–14. doi:10.1016/j.ijfatigue.2014.01.014.
- [40] R.E. Peterson, *Stress Concentration Factors*, John Wiley & Sons, 1977.
- [41] G. Glinka, Energy density approach to calculation of inelastic strain-stress near notches and cracks, *Eng. Fract. Mech.* 22 (1985) 485–508. doi:10.1016/0013-7944(85)90148-1.
- [42] M. Hoffmann, T. Seeger, A Generalized Method for Estimating Multiaxial Elastic-Plastic Notch Stresses and Strains, Part 1: Theory, *J. Eng. Mater. Technol.* 107 (1985) 250. doi:10.1115/1.3225814.
- [43] H. Hoffmann, T. Seeger, Stress-Strain Analysis and Life Predictions of a Notched Shaft under Multiaxial Loading, *Multiaxial Fatigue Anal. Exp. {AE}-14.* (1989) 81–99.
- [44] A.A. Moftakhar, *Calculation of Time-Independent and Time-Dependent Strains and Stresses in Notches*, University of Waterloo, 1994.
- [45] M. Hoffmann, H. Amstutz, T. Seeger, Local strain approach in nonproportional loading, *Third Int. Conf. Biaxial/Multiaxial Fatigue.* (1989) 55.1–55.20.
- [46] M.N.K. Singh, *Notch Tip Stress Strain Analysis in Bodies Subjected to Non-Proportional Cyclic Loads*, (1998).
- [47] S.M. Tipton, D.V. Nelson, *Methods for estimating cyclic notch strains in the SAE*

- specimen, (1989) 101–106.
- [48] Y.L. Lee, Y.J. Chiang, H.H. Wong, A constitutive model for estimating multiaxial notch strain, *J. Eng. Mater. Technol.* 117 (1995) 33–40.
- [49] A. Ince, G. Glinka, A. Buczynski, Computational modeling of multiaxial elasto-plastic stress–strain response for notched components under non-proportional loading, *Int. J. Fatigue.* 62 (2014) 42–52. doi:10.1016/j.ijfatigue.2013.10.008.
- [50] J. Das, S. Sivakumar, An evaluation of multiaxial fatigue life assessment methods for engineering components, *Int. J. Press. Vessel. Pip.* 76 (1999) 741–746. doi:10.1016/S0308-0161(99)00053-8.
- [51] W. Fash, “An Evaluation of Damage Development During Multiaxial Fatigue of Smooth and Notched Specimens,” James Walter Fash, August 1985 (UILU-ENG 85-3607). | Fracture Control Program - Illinois, 1985.
- [52] F. Shen, G.Z. Voyiadjis, W. Hu, Q. Meng, Analysis on the fatigue damage evolution of notched specimens with consideration of cyclic plasticity, *Fatigue Fract. Eng. Mater. Struct.* 38 (2015) 1194–1208. doi:10.1111/ffe.12299.
- [53] Tipton, Fash, Multiaxial Fatigue Life Predictions of the {SAE} Specimen Using Strain Based Approaches, *Multiaxial Fatigue Anal. Exp. {AE}-14.* (1989) 67–80.
- [54] J. Li, Q. Sun, Z.-P. Zhang, C.-W. Li, D.-W. Zhang, A New Multiaxial Fatigue Life Prediction Model Under Proportional and Nonproportional Loading, *J. Eng. Mater. Technol.* 132 (2010) 021016. doi:10.1115/1.4000823.
- [55] M. Firat, A numerical analysis of combined bending–torsion fatigue of SAE notched shaft, *Finite Elem. Anal. Des.* 54 (2012) 16–27. doi:10.1016/j.finel.2012.01.005.
- [56] A. Ince, G. Glinka, A generalized fatigue damage parameter for multiaxial fatigue life prediction under proportional and non-proportional loadings, *Int. J. Fatigue.* 62 (2014) 34–41. doi:10.1016/j.ijfatigue.2013.10.007.
- [57] N. Gates, A. Fatemi, Notch deformation and stress gradient effects in multiaxial fatigue, *Theor. Appl. Fract. Mech.* (2016). doi:10.1016/j.tafmec.2016.02.005.
- [58] S.M. Tipton, D. V Nelson, Advances In Multiaxial Fatigue Life Predictions For Components With Stress Concentrations, *Int. J. Fatigue.* 19 (1997) 503–515. doi:10.1016/S0142-1123(96)00070-9.
- [59] Y. Weixing, Stress field intensity approach for predicting fatigue life, *Int. J. Fatigue.* 15 (1993) 243–246. doi:10.1016/0142-1123(93)90182-P.
- [60] Y. Weixing, X. Kaiquan, G. Yi, On the fatigue notch factor , *Kf*, (1995).
- [61] D.G. Shang, D.K. Wang, M. Li, W.X. Yao, Local stress-strain field intensity approach to fatigue life prediction under random cyclic loading, *Int. J. Fatigue.* 23 (2001) 903–910. doi:10.1016/S0142-1123(01)00051-2.
- [62] H. Adib, G. Pluvinage, Theoretical and numerical aspects of the volumetric

- approach for fatigue life prediction in notched components, *Int. J. Fatigue*. 25 (2002) 67–76. doi:10.1016/S0142-1123(02)00040-3.
- [63] ANSYS Inc., ANSYS Mechanical APDL Structural Analysis Guide, 2013. [http://148.204.81.206/Ansys/150/ANSYS Mechanical APDL Structural Analysis Guide.pdf](http://148.204.81.206/Ansys/150/ANSYS%20Mechanical%20APDL%20Structural%20Analysis%20Guide.pdf).
- [64] ANSYS Inc., ANSYS Mechanical APDL Element Reference, 2013. doi:www.ansys.com.
- [65] J.R. Besseling, A theory of elastic, plastic and creep deformations of an initially isotropic material showing anisotropic strain-hardening, creep recovery, and secondary creep, 1959.
- [66] D.R.J. Owen, A. Prakash, O.C. Zienkiewicz, Finite element analysis of non-linear composite materials by use of overlay systems, *Comput. Struct.* 4 (1974) 1251–1267.
- [67] ASTM E8/E8M: 2009, Standard Test Methods for Tension Testing of Metallic Materials 1, i (2010) 1–27. doi:10.1520/E0008.
- [68] A. Standard, E9 (2009) Standard test methods of compression testing of metallic materials at room temperature, ASTM Int. West Conshohocken, PA. (2003).
- [69] J. Albinmoussa, On the application of polar representation for investigating high and low cycle fatigue of metals, *Int. J. Fatigue*. (2016). doi:10.1016/j.ijfatigue.2016.12.014.
- [70] A. Ince, Development of Computational Multiaxial Fatigue Modelling For Notched Components, University of Waterloo, 2012.
- [71] A. Fatemi, P. Kurath, Multiaxial fatigue life predictions under the influence of mean-stresses, *J. Eng. Mater. Technol.* 110 (1988) 380–388.
- [72] J. Albinmoussa, H. Jahed, S. Lambert, Cyclic behaviour of wrought magnesium alloy under multiaxial load, *Int. J. Fatigue*. 33 (2011) 1127–1139. doi:10.1016/j.ijfatigue.2011.01.009.
- [73] J. Zhang, Q. Yu, Y. Jiang, Q. Li, An experimental study of cyclic deformation of extruded AZ61A magnesium alloy, *Int. J. Plast.* 27 (2011) 768–787. doi:10.1016/j.ijplas.2010.09.004.
- [74] J. Hoffmeyer, Anrisslebensdauervorhersage bei mehrachsiger Beanspruchung auf Basis des Kurzrissskonzepts, *Inst. für Stahlbau und Werkstoffmechanik*, 2005.
- [75] F. Castro, Y. Jiang, Fatigue life and early cracking predictions of extruded AZ31B magnesium alloy using critical plane approaches, *Int. J. Fatigue*. 88 (2016) 236–246.
- [76] Y. Jiang, O. Hertel, M. Vormwald, An experimental evaluation of three critical plane multiaxial fatigue criteria, *Int. J. Fatigue*. 29 (2007) 1490–1502. doi:10.1016/j.ijfatigue.2006.10.028.

VITAE

Name: Syed Haris Iftikhar

Nationality: Pakistan

Present Address: KFUPM P. O. Box 8366, King Fahd University of Petroleum and Mineral, Dhahran-31261, Saudi Arabia.

Permanent Address: H. No. 43, Street 5, Sector J4, Phase 2, Hayatabad, Peshawar, Pakistan.

Email Address: g201406060@kfupm.edu.sa
syedharis_iftikhar@yahoo.com

Educational Qualification:

M.S (Mechanical Engineering)
January, 2017
King Fahd University of Petroleum & Minerals,
Dhahran, Saudi Arabia.

B.Sc (Mechanical Engineering)
June, 2012
GIK Institute,
Topi, Pakistan.